การศึกษาระบบตรวจวัตถุระเบิดและสารเสพติดที่ใช้นิวตรอนโดยการจำลอง
แบบมอนติคาร์โลและการทดลอง

นายสมหมาย ช่างเขียน

STUDY OF THE NEUTRON-BASED EXPLOSIVE

AND DRUG DETECTION SYSTEM USING

MONTE CARLO SIMULATION

AND EXPERIMENT

Sommai Changkian

A Thesis Submitted in Partial Fulfillment of the Requirements

for the Degree of Doctor of Philosophy in Physics

Suranaree University of Technology

Academic Year 2006

STUDY OF THE NEUTRON-BASED EXPLOSIVE AND DRUG DETECTION SYSTEM USING MONTE CARLO SIMULATION AND EXPERIMENT

Suranaree University of Technology has approved this thesis submitted in partial fulfillment of the requirements for the Degree of Doctor of Philosophy.

Thesis Examining Committee

_____

(Assoc. Prof. Dr. Prapan Manyum)

Chairperson

_____

(Asst. Prof. Dr. Worasit Uchai)

Member (Thesis Advisor)

_____

(Prof. Hancheng Sun)

Member

_____

(Assoc. Prof. Dr. Samnao Phatisena)

Member

_____

(Assoc. Prof. Dr. Yupeng Yan)

Member

_____ _____

(Assoc. Prof. Dr. Saowanee Rattanaphani) (Assoc. Prof. Dr. Sompong Thammathaworn)

Vice Rector for Academic Affairs   Dean of Institute of Science

สมหมาย ช่างเขียน : การศึกษาระบบตรวจวัตถุระเบิดและสารเสพติดที่ใช้นิวตรอนโดยการ
จำลองแบบมอนติคาร์โลและการทดลอง (STUDY OF THE NEUTRON-BASED
EXPLOSIVE AND DRUG DETECTION SYSTEM USING MONTE CARLO
SIMULATION AND EXPERIMENT) อาจารย์ที่ปรึกษา : ผู้ช่วยศาสตราจารย์ พันเอก ดร.
วรศิษย์ อุชัย, 161 หน้า.

ในวิทยานิพนธ์นี้ได้ทำการศึกษาถึงระบบตรวจวัตถุระเบิดและสารเสพติดที่ใช้นิวตรอน
โดยการจำลองด้วยโปรแกรมคอมพิวเตอร์แบบมอนติคาร์โลและการทำการทดลอง แหล่งกำเนิด
นิวตรอนที่ใช้เพื่อการก่อกัมมันต์ในวัตถุระเบิดชนิด ทีเอ็นที (TNT) อาร์ดีเอ็กซ์ (RDX) และวัตถุ
ทั่วไปอื่นๆ คือแคลิฟอร์เนียมและอะเมอริเซียมเบอริเลียม โปรแกรมคอมพิวเตอร์ที่ใช้เพื่อการ
จำลองคือโปรแกรม MCNP5 ในการจำลองการเกิดสเปกตรัมของรังสีแกมมาที่เกิดจากการกัมมันต์
ในไฮโดรเจน คาร์บอน ไนโตรเจน ออกซิเจน ทีเอ็นที อาร์ดีเอ็กซ์และวัตถุทั่วไปอื่นๆ นั้นอาศัยการ
แสดงผลชนิดเอฟ4 และเอฟ8 โดยในชนิดเอฟ4 จะเกิดเส้นสเปกตรัมรังสีแกมมาที่สำคัญต่างๆทั้ง
จากนิวตรอนอุณหภาพและนิวตรอนพลังงานสูง โดยมีเส้นสเปกตรัมที่สำคัญคือ 2.2 ล้าน
อิเล็กตรอนโวลต์จากไฮโดรเจน 4.4 ล้านอิเล็กตรอนโวลต์จากคาร์บอน 6.1 ล้านอิเล็กตรอนโวลต์
จากออกซิเจน และ 10.8 ล้านอิเล็กตรอนโวลต์ จากไนโตรเจน ส่วนการแสดงผลแบบเอฟ8 มีเพียง
รังสีแกมมาพลังงาน 10.8 ล้านอิเล็กตรอนโวลต์จากไนโตรเจนเกิดขึ้นในสเปกตรัมของ ทีเอ็นที อาร์
ดีเอ็กซ์และเมลามีน ได้มีการออกแบบระบบตรวจวัตถุระเบิดที่มีอุโมงค์เป็นรูปสี่เหลี่ยมขนาดกว้าง
30 เซนติเมตร ยาว 40 เซนติเมตร สูง 15 เซนติเมตรขึ้นมาและใช้เป็นแบบจำลองสำหรับการจำลอง
และการทดลอง ได้ทำการจำลองและวัดฟลักซ์ของนิวตรอนอุณหภาพที่กึ่งกลางอุโมงค์ของระบบ
ตรวจวัตถุระเบิดดังกล่าว นอกจากนี้ยังได้ทำการจำลองและวัดปริมาณรังสี ณ จุดที่ห่างจากผิวนอก
ของระบบตรวจวัตถุระเบิด 1 เมตร   ได้ทำการวัดพื้นที่ใต้กราฟของสเปกตรัมที่เกิดจากทีเอ็นที
น้ำหนัก 1000 กรัม 520 กรัม และ 200 กรัม ตามลำดับ เมื่อนำผลการวัดที่ได้มาหาความไวในการ
ตรวจของระบบตรวจวัตถุระเบิดโดยอาศัยเส้นรังสีแกมมาพลังงาน 10.8 ล้านอิเล็กตรอนโวลต์
พบว่ามีค่าเฉลี่ยเป็น 0.53 เคาน์/วินาที-กิโลกรัม แต่ค่าดังกล่าวที่ได้จากการจำลองมีค่าเป็น 6.64
เคาน์/วินาที-กิโลกรัมซึ่งสูงกว่าค่าจากการทดลอง 12.5 เท่า นอกจากนี้ได้ทำการออกแบบระบบ
ตรวจวัตถุระเบิดที่ใช้แคลิฟอร์เนียมโดยมีอุโมงค์ตรวจขนาดใหญ่คือ กว้าง 40 เซนติเมตร ยาว 80
เซนติเมตร และสูง 60 เซนติเมตรใช้พอลิเอทธิลีนเป็นตัวลดทอนพลังงานนิวตรอน ใช้ลิเธียม
คาร์บอเนตเป็นตัวกำบังนิวตรอนและใช้ตะกั่วเป็นตัวกำบังรังสีแกมมา ได้ทำการประมาณค่าความ
แรงของแหล่งกำเนิดนิวตรอนที่จำเป็นสำหรับการตรวจทีเอ็นทีและอาร์ดีเอ็กซ์ด้วยความไวต่างๆ

สำหรับการตรวจทีเอ็นทีที่ 300 กรัม และอาร์ดีเอ็กซ์ที่ 150 กรัมนั้น พบว่าความแรงของแหล่งกำเนิด
ที่เหมาะสมคือ 5.8×10^8 นิวตรอนต่อวินาที ได้ทำการประมาณค่าปริมาณรังสีที่ผิวนอกของระบบ
ตรวจวัตถุระเบิดเช่นกันเมื่อใช้พอลีเอ็ทธิลีน ลิเธียมคาร์บอเนตและตะกั่วหนา 45 5 และ 0.5
เซนติเมตร ตามลำดับ โดยแหล่งกำเนิดมีความแรง 5.8×10^8 นิวตรอนต่อวินาที พบว่าปริมาณรังสี
สูงสุดที่ผิวคือ 7.0×10^{-6} พิโคซีเวิร์ต ซึ่งเป็นค่าที่ต่ำกว่าเกณฑ์ปริมาณรังสีสูงสุดที่ยอมรับได้ เมื่อใช้
ค่ารังสีสูงสุดนี้ประมาณค่าปริมาณรังสีที่ผู้ปฏิบัติงานกับระบบตรวจวัตถุระเบิดได้รับในเวลา 1 ปี
(ทำงานแปดชั่วโมงต่อวัน ในเวลา 365 วัน) พบว่าปริมาณรังสีที่ได้รับคือ 0.03 ซีเวิร์ต

สาขาวิชาฟิสิกส์   ลายมือชื่อนักศึกษา_____
ปีการศึกษา 2549   ลายมือชื่ออาจารย์ที่ปรึกษา_____
                                                              ลายมือชื่ออาจารย์ที่ปรึกษาร่วม_____

SOMMAI CHANGKIAN : STUDY OF THE NEUTRON-BASED EXPLOSIVE AND DRUG DETECTION SYSTEM USING MONTE CARLO SIMULATION AND EXPERIMENT. THESIS ADVISOR : ASST. PROF. WORASIT UCHAI, Ph.D. 161 PP.

NEUTRON-BASED TECHNIQUE / EXPLOSIVE DETECTION / MONTE CARLO SIMULATION / THERMAL NEUTRON ACTIVATION / FAST NEUTRON ACTIVATION / GAMMA RAY ATTENUATION

The neutron-based explosive and drug detection system is studied by using Monte Carlo simulation and experiment. Cf and Am/Be are used as neutron sources for activations of TNT, RDX and other common materials. MCNP5 is used as the Monte Carlo computer code for simulations. The F4 and F8 tallies of gamma ray spectra resulted from activations of H, C, N, O, TNT, RDX and other common materials are used in the simulations. For F4 tallies, all of the important gamma ray lines results from the thermal and fast nuclear reactions (2.2, 4.4, 6.1 and 10.8 MeV from H, C, O and N, respectively) present in their respective spectra. For F8 tallies, only the 10.8 MeV from N presents in the pulse height spectra of TNT, RDX and Melamine.

The geometry of the small explosive detection system (EDS) with the inspection cavity of 30 cm × 40 cm × 15 cm is designed and used as a model for MCNP simulations and experimental set up. The thermal neutron fluxes created at the center of the EDS are simulated and experimentally measured. Dose at points of 1 m away from the EDS's surfaces are also simulated and measured. The pulse height spectra resulting from inspections of 1000, 520 and 200 g of TNT are measured experimentally. The average detection sensitivity for inspections of

the 10.8 MeV gamma ray lines is 0.53 counts/s-kg. However, the corresponding MCNP simulation detection sensitivity value is 0.60 counts/s-kg. It is about 13% different from the experimental value.

A large EDS suitable for the inspection of briefcase or small parcel by using Cf-source is also designed. It has a dimensions of 40 cm $\times$ 60 cm $\times$ 80 cm with polyethylene, lithium carbonate and lead as the moderator, neutron shielding and gamma ray shielding materials, respectively. The source strength required for inspections of TNT and RDX with a certain detection sensitivity is estimated. For inspections of TNT and RDX with sensitivity of 300 and 150 g, respectively, the source strength required is 5.9×10^8 n/s. Doses at various surfaces of the EDS are also estimated. With polyethylene, lithium carbonate and lead of 45, 5 and 0.5 cm thick and source strength of 5.9×10^8 n/s, the highest surface dose is 7.0×10^{-6} pSv. This value is used to estimate the maximum total dose received by an operator working with the EDS for one year (8 hours per day for 365 days). The results is 0.03 Sv which is well under the whole body maximum permissible dose of 0.05 Sv.

School of Physics   Student's Signature _____

Academic Year 2006   Advisor's Signature _____

                                             Co-advisor's Signature _____

ACKNOWLEDGEMENTS

patience during my Ph.D. study.

Special thanks to my parents, my sister and my brother for their understanding, support and encouragement during my Ph.D. study.

Finally, I myself standstill survive with my inspired song "You Can Get It If You Really Want" from Jimmy Cliff.

Sommai Changkian

CONTENTS

CONTENTS (Continued)

CONTENTS (Continued)

CONTENTS (Continued)

CONTENTS (Continued)

CONTENTS (Continued)

LIST OF TABLES

LIST OF FIGURES

LIST OF FIGURES (Continued)

LIST OF FIGURES (Continued)

LIST OF FIGURES (Continued)

LIST OF FIGURES (Continued)

LIST OF FIGURES (Continued)

LIST OF FIGURES (Continued)

CHAPTER I

INTRODUCTION

1.1 Effect of explosions

It is well recognized that the explosion has devastating effects on humanity, causing losses of human life and properties. There were many incidents involving explosions in different places and occasions which either killed innocent peoples or destroyed people's properties or both; an explosion occurred on an airplane in midair (Pan Am flight 103, in Lockerbie, Scotland in 1988) causing a crash of the airplane and killed 270 passengers (วรศิษย์ อุชัย, 2002); an explosion occurred in the state's government building in 1995 which killed 686 lives and destroyed the hold building worth of 142 million U.S. dollars; an explosion occurred in Bhali, an important tourist attraction of Indonesia, in 2002 which killed 202 innocent tourists. Many other explosions occurred almost daily at other places around the world, such as the explosions in many countries in the Middle East and Southeast Asia, including three southernmost provinces of Thailand. Most of these explosions are the results of conflicts between nations, religious and ethics. Though it is very difficult to prevent such explosions, it can be better controlled if the effective explosive detection systems are available. The following sections describe the available explosive detection methods.

1.2 Explosive detection methods

There are many methods used in the explosive detection systems at present. The following sections describe the principle, technical descriptions and applications of these methods

1.2.1 Metal detection

The metal detection method uses the electromagnetic signal, arising from inspection of the object, as the signature for the existence of explosive. The eddy current created in the metal detector is used to trigger its' alarm (He et al., 2002). It is sensitive to small ferrous particle and can be developed for pass-through or hand-held detector. Plastic explosives, however, escape detection by this method.

1.2.2 Vapour detection

The success of dogs in being able to locate explosive has inspired a number of studies involving "electronic nose" that mimic, in a limited manner, olfaction in vertebrates. One needs to have sensing elements that have responses to very low concentrations of explosives. Molecular recognition phenomena have been extensively studied for various applications (Yang et al., 2001). These detectors measure traces of characteristic volatile compounds that evaporate from the explosive or are present as particles on the explosive's container surface. Particle samples are collected by wiping a surface with a paper filter trap or with hand-held vacuum, followed by desorption into an analyzer/detector (Yinon, 2002). Pinnaduwage et al. (2004) developed a micro-electromechanical system (MEMS) explosive sensor, advantage in compactness and possible low cost. Chemosensors, such as light-emitting polymer thin films also have been demonstrated as highly

sensitive chemosensor for 2,4,6-trinitrotoluene (TNT) (Lin et al., 2004).

1.2.3   Radio frequency

The system that uses this principle is called Nuclear Quadrupole Resonance (NQR). It is tuned to respond to the interaction of radio-frequency (RF) energy with nitrogen in the crystalline structure of explosives. The advantage of ^{14}N-NQR spectroscopy when used for the detection of explosives results from the high chemical and crystallographic specificity of NQR spectra which depend very strongly on a small changes in electronic charge distribution over the whole molecule. Due to this specificity one can identify chemical compounds unambiguously by measuring the frequencies of NQR spectra e.g. in nitrogen containing explosive substances. On the other hand NQR detection of explosives suffers from relatively low sensitivity caused by low resonance frequencies (0.5–6 MHz) inherent in NQR spectroscopy of ^{14}N nuclei (Ostafin et al., 2006).

1.2.4   X-ray-based method

The standard x-ray scanner has a fan-shaped or scanning x-ray beam that is transmitted through the object to be inspected. The absorption of x-rays is usually measured by an array of detectors and a high-resolution image, derived from the degree of absorption of the beam, is produced. The image depends primarily on the density of objects located in the inspected object along the beam of the x-ray. These devices cannot distinguish between a thin sheet of a strong absorber, such as a metal, and a thick slab of a weak absorber. Simple x-ray systems rely on humans or operators to serve as pattern recognition devices. Dual-energy systems are really two x-ray systems, whose beams are generated by sources that peak at different energies, producing two independent images. The higher energy view

suffers less absorption. While areas of heavy elements are dark in both views, areas of light elements are darker in the lower energy view. By comparing both images, light elements such as carbon, nitrogen, and oxygen may be emphasized. In this way, it is possible to determine whether a given object is made of a light or a heavy element. Multi-energy systems are essentially the same except that they have a single x-ray tube that transmits a broad spectrum of energies. Detectors are used to select specific energy regions. Both systems produce effectively the same result. This technique cannot distinguish among the light elements, such as nitrogen, oxygen and carbon. However, it can overcome the countermeasure of hiding explosives behind an object made of a heavy element, such as steel of 8 to 10 mm thick. These devices are technically identical to simple x-ray scanners, except for the dual energy and image feature. The backscatter system scans a pencil beam of x-rays across the object and makes two images: the normal transmission image, created by a single detector on the opposite side, and a backscatter image, created by a large area detector on the side of the entering beam. A single energy x-ray beam is utilized. A two-sided version of this system with two identical x-ray beam systems makes backscatter measurements from opposite sides of the object to enhance the backscatter penetration capability of the system. The transmitted beam provides a typical x-ray image showing primarily the absorption by heavy elements. The backscatter signal intensity depends on how much of the transmitted beam has been absorbed, how much is backscattered, and how many of the backscattered x-rays reach the backscatter detectors. The backscatter signal depends on the competition between photoelectric absorption and Compton scattering. The photoelectric cross section increases with the atomic number of the object, while the Compton cross section is relatively independent of atomic number. Therefore, the resulting backscatter signal favors the low Z elements, with

particular emphasis on low Z elements of high density, such as plastic explosives. Backscatter imaging provides a direct measure of the density of elements with low atomic number. The system produces two independent x-ray images: an x-ray transmission image emphasizing the high Z elements, and an x-ray backscatter image emphasizing the low Z elements. The system utilizes a proprietary Flying Spot technique, which sweeps a small pencil beam of x rays across the object to generate each line of image data. A single large solid-state. transmission detector measures the x-ray absorption by integrating the detected x-ray flux over time. The Flying Spot scanning beam technology is required for efficient scatter imaging. Because only one small area is illuminated by the pencil beam at any instant of time, all detectable backscatter must come from that pixel. A large solid-state detector measures the backscattered x-ray signal, again with time integration of the detected backscattered flux. By comparing the two images, the operator can make judgments about the composition of regions of high density, which may help detect and identify threatening contents of a bag (OTA report, 1991).

1.2.5   Gamma ray-based method

Science Applications International Corporation (SAIC) developed the Vehicle and Cargo Inspection System (VACIS) for inspection of tanker truck passing through the U.S. Custom check points along the border between U.S.A. and Mexico. VACIS is a gamma- ray based method utilizing gamma rays from a shuttered radioactive source (Cs-137 or Co-60) as a mean to produce a fan-shaped beam of radiation for line scanning of the inspected object. A tower of NaI detectors is used to collect gamma ray transmitted signals for construction of a two dimensional image in the same way as the x-ray based method. The image created is based on the absorption characteristics of the inspected object (Victor et al., 2005). The

test results show that VACIS can detect a toxic explosive fluid hidden behind the 3/4 to 3/2 inches thick steel wall of the truck.

1.2.6   Neutron-based method

Neutrons are electrically neutral particles and can therefore interact only with nucleus. Because of the short range action of nuclear forces, even low energy neutrons can therefore still penetrate thick substances, which is needed for the application of explosive inspection (1–2 cm of steel and 20–30 cm of earth should be feasible, although with increasing attenuation for increasing thickness). The behavior of neutrons in matter depends strongly on their kinetic energy. Fast neutrons interact preferentially via scattering and nuclear reactions. The probability of reaction (cross section) for slow neutron (E < 0.5 eV) changes heavily from one element to the other. Thermal neutrons are a special type of slow neutrons, whose kinetic energy distribution is in equilibrium with their surrounding (with a typical energy of 0.025 eV at room temperature). They move on irregular paths like a gas through matter, neither accelerating nor slowing down, scattering quite a number of times until they are absorbed (captured in the nucleus). In neutron activation analysis, the elemental composition of the sample is determined from the intensity of prompt gamma rays produced through neutron inelastic scattering $(n,n'\gamma)$ or thermal neutron capture (n,γ)(Al-Jarallah et al., 2003). The following sections describe various explosive detection methods available based on neutrons.

Thermal Neutron Analysis (TNA)

TNA uses fast neutrons from either radioactive source or neutron generator as medias to detect nitrogen (N), an important elemental composition of all explosives. These neutrons will slow down when passing through the interrogated object and become thermal neutron before being captured by ^{14}N. The nuclei of

^{14}N will become the excited-compound nuclei of ^{15}N* and release the 10.8 MeV characteristic gamma rays while returning to the ground state of ^{15}N. The detection of many such gamma rays will signify that the inspected object may contain explosives. Thermal neutron activation (TNA) is based on the well-known ^{14}N(n, γ)^{15} N reactions which has a cross-section of 0.011 barns for producing the 10.8 MeV gamma rays (Gozani, 2003).

Fast Neutron Analysis (FNA)

FNA is a neutron -based technique which utilizes interactions between fast neutrons and the elemental compositions of the inspected object. The nuclear inelastic scattering (n,ńγ) reaction is the basis of the method. The neutron energy has therefore to be above a given threshold for each of the elements involved, about 5 MeV for carbon (producing 4.43 MeV characteristic gamma rays) and 7 MeV for oxygen (producing 6.13, 3.84 MeV characteristic gamma rays). Nitrogen can also produce intense high-energy gamma rays as a result of inelastic scattering with fast neutrons (producing 1.63, 2.3 and 5.1 MeV characteristic gamma rays). The energies of the gamma rays emitted indicate the elements present in the object. The intensity of the gamma rays indicates the relative amount of elements present. It is therefore in principle possible to calculate the elemental ratios for determination of substance under analysis. In the case of explosives, the ratios between carbon, nitrogen, and oxygen ratios can be obtained. FNA has therefore the potential of delivering better results than TNA, because it is sensitive to nearly all elements in explosives and opens the possibility of identifying the substance under analysis, but is usually far more complex and expensive. A fast neutron analysis technique for determining the elemental composition and density of explosive material by using the 14 MeV D-T neutron source was proposed (Hussein and Lord, 1990).

Pulsed Fast Neutron Analysis (PFNA)

The Pulsed Fast Neutron Analysis Cargo Inspection System was introduced by Rynes et al. (1999) to inspect large objects for contraband. This system uses a nanosecond pulsed beam of fast neutrons to inspect the contents of small volume elements of a cargo container or truck. A color display shows the three-dimensional location of suspected contraband, such as drugs or explosives. The neutrons interact with the elemental contents of each voxel, and gamma rays characteristic of the elements are collected by an array of detectors (Rynes et al., 1999; Sawa, 1993). The PFNA concept is similar to the FNA system, except that a pulsed beam of neutrons is utilized. A focused and collimated beam is passed through the object, resulting in the emission of gamma rays of specific energies, characteristic of elemental compositions of the object. This method uses penetrating neutrons at lower energies than those in FNA. At these energies, the probability for gamma ray production by nuclear reactions with oxygen, carbon, chlorine and nitrogen is about the same as for 14 MeV neutrons. However, the gamma ray spectrum is cleaner and shows a much better signal-to noise ratio. The gamma rays are detected, as before, by scintillators that provide gamma ray energy information by which the element can be identified. The neutron beam profile provides the two-dimensional position information required to determine the spatial distribution. The third dimension, derived by timing and image reconstruction, constitutes a significant improvement over the basic FNA technique (OTA report, 1991).

Pulsed Fast-Thermal Neutron Analysis (PFTNA)

PFTNA usually involves two types of neutron-induced reactions, namely, the fast neutron reactions during the emission of the neutron pulse (inelastic scattering reactions $(n,\acute{n}\gamma)$ and neutron capture reactions (n,γ) during two consecutive pulses (Womble et al., 1995; Vourvopoulos, 1993). When the 14 MeV neutrons

intereact with the explosive elemental compositions the (n,ńγ) reaction takes place over a very short time (10^{-8}–10^{-7} s) with the emission of characteristic gamma rays. After a certain number of collisions neutrons lose their energy to become thermal neutrons over 10^{-6}–10^{-5} s. Some thermal neutrons diffuse in the materials by (n,γ) reactions. It is not easy to detect the pure inelastic spectra according to the reaction time and the actual condition of pulsed neutron generator. A gate circuit is employed in the experiment to separate spectrum I (the overall spectrum of inelastic, capture and activation) and spectrum II (the sum spectrum of capture and activation). The two spectra are used to identify C, O and H in explosive.

1.3 The methods used in this thesis

Each of the above method has its own drawbacks. Metal detection is difficult to detect plastic explosive as it involves only detecting ferrous particle. X-rays suffer from the main disadvantage of having low interaction probability with the low-electron density elements from which the explosive materials are composed. However, these low-mass-number elements exhibit much higher interaction probabilities when exposed to neutrons. The pulsed neutron methods are based on using neutron generator which requires the thick shielding materials. There fore, they tends to be heavier and more expensive. We therefore investigate in this thesis a method that utilizes the neutron radioactive source which requires the thin shielding materials. This method will be easy to operate and cost effective. The TNA and FNA methods are the basis for our explosive inspection system. Since neutron radioactive sources also produce gamma rays, the Gamma ray Attenuation Analysis (GAA) is also used in our explosive inspection system. Monte Carlo simulations of the principles of these analyses are performed to investigate whether they can indicate the existence of explosive in the inspected object or

not. An experiment to confirm some of the simulation results were done at China Institute of Atomic Energy (CIAE), Beijing, China.

This thesis is organized as follows: Chapter I: Introduction; Chapter II: Monte Carlo Simulation and Radiation interaction; Chapter III: MCNP Simulation and experimental set up; Chapter IV: Simulation and experimental results; Chapter V: Conclusions.

CHAPTER II

THEORY

Since the main part of this thesis involves simulations of the principle of the nuclear-based EDS by using MCNP computer code, the description of Monte Carlo methods and its relevant theories on radiation interaction with matters will be described in the following sections.

2.1 Introduction to MCNP

MCNP, which stands for Monte Carlo N Particles, is a general-purpose N particles Monte Carlo transport code, where N represents either neutron, photon, electron or combination of them. It can be used with neutron energy from 10^{-11} MeV to 20 MeV, and photon and electron energy from 1 keV to 1000 MeV. In using MCNP for simulation, the user must create an input file that is subsequently read by MCNP. This file contains information about the problem in areas such as the geometry specification, the description of materials, the selection of cross-section evaluations, the source definition, the type of answers or tallies desired, and any variance reduction techniques. In solving a problem, Monte Carlo uses the statistical method which is different from deterministic method. The following sections compare the Monte Carlo and the deterministic methods and provide the simple description of Monte Carlo methods.

2.1.1 Monte Carlo method versus Deterministic method

Monte Carlo methods are very different from deterministic transport methods. Deterministic methods solve the transport equation for the average particle behavior. In contrast, Monte Carlo methods do not solve any explicit equation but rather obtain answers by simulating individual particles and recording some aspects of their average behavior. The average behavior of particles in the physical system is then inferred from the average behavior of the simulated particles. Moreover, what constitutes their solutions is also different. Typically, deterministic methods give fairy complete information, such as flux throughout the phase space of the problem. Mote Carlo gives information only about specific tallies requested by user. Another different aspect between Monte Carlo and deterministic methods is the type of equation which they solve. Monte Carlo solves the integral transport equation, whereas discrete method solves the integro-differential transport equation. Two aspects are misleading about this statement. First, the integral and integro-differential transport equation are two different forms of the same equation. If one is solved, the other is solved. Second, Monte Carlo solves a transport problem by simulating particle histories rather than by solving an equation. Nonetheless, one can derive an equation that describes the probability density of particles in phase space. This turns out to be the same as the integral transport equation.

2.1.2 The Monte Carlo Method

Monte Carlo can be used to duplicate theoretically a statistical process, such as interaction of nuclear particles with matters. It is particularly useful for

complex problem that can not be modeled by computer codes that use deterministic methods.The individual probabilistic events that comprise a process are simulated sequentially. The probability distribution governing these events are statistically sampled to describe the total phenomenon. In general, the simulation is performed on a digital computer because the number of trials necessary to adequately describe the phenomenon is very large. The statistical sampling process is based on the selection of random numbers. This process is analogous to throwing dice in a gambling casino- hence the name "Monte Carlo". In particle transport, the Monte Carlo technique is very realistic. It follows each particles from its birth (releasing from source) throughout its life when it is absorbed in or escaped from the system. Probability distributions of its transport are randomly sampled until the outcome at each step of its life has been scored. Figure 2.1 represents the random history of a neutron incident on a bulk of concrete. Numbers between 0 and 1 are selected randomly to determine what, if any, and where interaction takes place, based on the physical rules and probabilities governing the processes and materials involved. In this particular example, a neutron collision occurs at event 1. The neutron is scattered in the direction shown, which is selected randomly from the physical scattering distribution. A photon is also produced and is temporarily stored in a certain memory location for later analysis. At event 2, a slowing down neutrons has been completely captured and produced one photon which leaks out at event 3. The remaining photon generated at event 1 is now followed with a capture at event 4. Note that MCNP retrieves stored particles such that the last particle stored in the memory is the first particle taken out. This neutron history is now complete. As more and more such histories are followed, the neutron and photon distributions become better known. The quantities of interest (whatever the user requests) are tallied, along with estimates of the statistical precision or
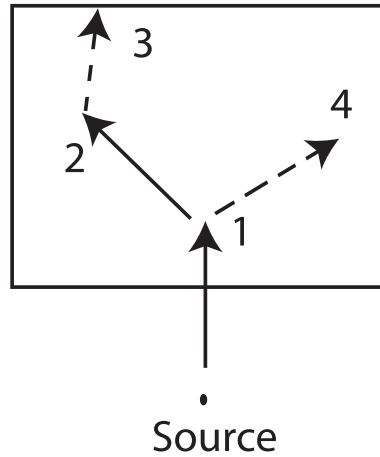
Figure 2.1 the random history of a neutron incident on a bulk of concrete.

uncertainty of the results. From this concept we can see that the accuracy of an estimate quantity tends to improve as one averages over larger and larger samples of the quantity. Suppose that the Monte Carlo simulation yields successive independent scores, x_1, x_2, x_3....x_N of the random variable x. If the sample mean

$$\bar{x} = \frac{1}{N} \sum_{i=1}^{N} x_i \tag{2.1}$$

is formed, the law of large numbers states that the sample mean, with a probability that approaches 1 as $N \to \infty$, approaches the population mean, or true mean. (x might be any quantity such as; energy deposition in a detector, flux through a specified region etc.)

The above Monte Carlo result can be written as

$$\bar{x} \pm S_x \tag{2.2}$$

where S_x represents the standard deviation of the mean of our N independent observations (particle tracks, for instance). We will see later that the results can be represented as follows:

$$\bar{x} \pm \sqrt{\frac{\overline{x^2} - (\bar{x})^2}{\sqrt{N}}} \tag{2.3}$$

equation (2.3) shows that S_x is proportional to $1/\sqrt{N}$. To reduce S_x, the number of histories must be increased which will take up more computer time.

This mean that the Monte Carlo technique is based upon a minimum amount of data and a maximum amount of floating-point operation. Deterministic calculations are often maximum data and minimal floating-point operation procedures. Since impediments to data processing are often caused by communication bottlenecks, either from the CPU to cache memory, cache memory to main memory or main memory to large storage devices (typically disk), modern computer architecture favors the Monte Carlo model which emphasizes iteration and minimizes data storage.

2.1.3 MCNP Features

In MCNP, there are many features that the user should know. These features include nuclear data and reactions, source specification, tally and output, estimation of error, and variance reduction technique. The details of these features are described in the following sections.

1) Nuclear Data and Reactions

MCNP uses continuous-energy nuclear and atomic data libraries. The primary sources of nuclear data are evaluations from the Evaluated Nuclear Data File (ENDF) 1 system, the Evaluated Nuclear Data Library (ENDL) 2 and the Activation Library (ACTL) 3 compilations from Livermore, and evaluations from the Applied Nuclear Science (T2) Group 4, 5, 6 at Los Alamos. Evaluated data are processed into a format appropriate for MCNP by codes such as NJOY.7 The processed nuclear data libraries retain as much detail from the original evaluations as is feasible to faithfully reproduce the evaluators intent. Nuclear

data tables exist for neutron interactions, neutron-induced photons, photon interactions, neutron dosimetry or activation, and thermal particle scattering $S(\alpha,\beta)$. Photon and electron data are atomic rather than nuclear in nature. Each data table available to MCNP is listed on a directory file, XSDIR. Users may select specific data tables through unique identifiers for each table, called ZAIDs. These identifiers generally contain the atomic number Z, mass number A, and library specifier ID (X-5 Monte Carlo Team, 2003).

2) Source Specification

MCNP generalized user-input source capability allows the user to specify a wide variety of source conditions without having to make a code modification. Independent probability distributions may be specified for the source variables of energy, time, position, and direction, and for other parameters such as starting cell(s) or surface(s). Information about the geometrical extent of the source can also be given. In addition, source variables may depend on other source variables (for example, energy as a function of angle) thus extending the built-in source capabilities of the code. The user can bias all input distributions. In addition to input probability distributions for source variables, certain built-in functions are available. These include various analytic functions for fission and fusion energy spectra such as Watt, Maxwellian, and Gaussian spectra; Gaussian for time; and isotropic, cosine, and monodirectional for direction. Biasing may also be accomplished by special built-in functions. A surface source allows particles crossing a surface in one problem to be used as the source for a subsequent problem. The decoupling of a calculation into several parts allows detailed design or analysis of certain geometrical regions without having to rerun the entire problem from the beginning each time. The surface source has a fission volume

source option that starts particles from fission sites where they were written in a previous run. The source definition will describe clearly in MCNP geometry.

3) Tallies and Output

In MCNP the user can identify the output results based on his simulation problem. This make various output independent on how specific results he prefer. These output results call "tallies" are related to particle current, particle flux, and energy deposition. In default MCNP tally is defined per starting particle. Currents can be tallied as a function of direction across any set of surfaces, surface segments, or sum of surfaces in the problem. Charge can be tallied for electrons and positrons. Fluxes across any set of surfaces, surface segments, sum of surfaces, and in cells, cell segments, or sum of cells are also available. Similarly, the fluxes at designated detectors (points or rings) are standard tallies. Heating and fission tallies give the energy deposition in specified cells. A pulse height tally provides the energy distribution of pulses created in a detector by radiation and a detector response function(gaussian distribution) must be adjust for a reasonable real detector. In fact, any quantity of the form

$$C = \int \phi(E)f(E)dE \tag{2.4}$$

can be tallied, where $\phi(E)$ is the energy-dependent fluence, and $f(E)$ is any product or summation of the quantities in the cross-section libraries or a response function provided by the user. The tallies may also be reduced by line-of-sight attenuation. Tallies may be made for segments of cells and surfaces without having to build the desired segments into the actual problem geometry. All tallies are functions of time and energy as specified by the user and are normalized to be per starting particle. In addition to the tally information, the output file contains tables of standard summary information to give the user a better idea

of how the problem ran. This information can give insight into the physics of the problem and the adequacy of the Monte Carlo simulation. If errors occur during the running of a problem, detailed diagnostic prints for debugging are given. Printed with each tally is also its statistical relative error corresponding to one standard deviation. Following the tally is a detailed analysis to aid in determining confidence in the results. Ten pass/no pass checks are made for the user-selectable tally fluctuation chart (TFC) bin of each tally. The quality of the confidence interval still cannot be guaranteed because portions of the problem phase space possibly still have not been sampled. Tally fluctuation charts are also automatically printed to show how a tally mean, error, variance of the variance, and slope of the largest history scores fluctuate as a function of the number of histories run. Tally results can be displayed graphically, either while the code is running or in a separate postprocessing mode.

4) Estimation of Monte Carlo Errors

MCNP tallies are normalized to be per starting particle and are printed in the output accompanied by the estimated relative error, R. This error is defined to be one estimated standard deviation of the mean S_x divided by the estimated mean $\bar{x}$. In MCNP, the quantities required for this error estimate, namely, the tally and its second moment are computed after each Monte Carlo history, which accounts for the fact that the various contributions to a tally from the same history are correlated. Tally may be good or poor. For a well-behaved tally, R will be proportional to $1/\sqrt{N}$ where N is the number of histories. Thus, to reduce R by half, we must increase the total number of histories fourfold. The poor behaved tally, R may increase with the number of histories. The estimated relative error can be used to form confidence intervals about the estimated mean, allowing the

user to learn about what the true result is. This idea involves the different between precision and accuracy of a Monte Carlo calculation. There is an extremely important difference between precision and accuracy of Monte Carlo calculation. Precision is the uncertainty in $\bar{x}$ caused by statistical fluctuations of $x_i{}'$s sampled during the Monte Carlo process. Accuracy is a measure of how close the expected value of $\bar{x}$, E_x, to the true physical quantity being estimated. The difference between this true value and the expected value of $\bar{x}$ is called the systematic error, which is seldom known. The following table shows guidelines for interpreting the relative error. More detail can be obtained from MCNP user manual (X-5 Monte Carlo Team, 2003).

Table 2.1 Guidelines for the interpretation of relative error.

Range of R	Quality of tally
0.5 to 1	Not meaningful
0.2 to 0.5	Factor of a few
0.1 to 0.2	Questionable
less than 0.1	Generally reliable
less than 0.05	Generally reliable for point detector

5) Variance reduction

As noted in the previous section, R (the estimated relative error) is proportional to $1/\sqrt{N}$, where N is the number of histories. For a given MCNP run, the computer time T consumed is proportional to N. Thus $R=C/\sqrt{T}$, where C is a positive constant. There are two ways to reduce R: (1) increase T and/or (2) decrease C. Computer budgets often limit the utility of the first approach.

For example, if it has taken 2 hours to obtain R=0.10, then 200 hours will be required to obtain R=0.01. For this reason MCNP has special variance reduction techniques for decreasing C. (Variance is the square of the standard deviation.) The constant C depends on the tally choice and/ or the sampling choices

For many problems, variance reduction is not just a way to speed up the problem but is absolutely necessary to get any answer at all. Deep penetration problems and pipe detector problems, for example, will run too slowly by factors of trillions without adequate variance reduction. Consequently, users have to become skilled in using the variance reduction techniques in MCNP. Most of the following techniques cannot be used with the pulse height tally. The following summarizes briefly the main variance reduction techniques available in MCNP. More details can be obtained from MCNP user manual (X-5 Monte Carlo Team, 2003).

1. **Energy cutoff:** Particles whose energy is out of the range of interest are terminated so that computation time is not spent following them.

2. **Time cutoff:** Like the energy cutoff but based on time.

3. **Geometry splitting with Russian roulette:** Particles transported from a region of higher importance to a region of lower importance undergo Russian roulette. Most particles are killed and some particle survive with increase rate.

4. **Energy splitting/Russian roulette:** Particles can be split or rouletted upon entering various user-supplied energy ranges. Thus important energy ranges can be sampled more frequently by splitting the weight among several particles and less important energy ranges can be sampled less frequently by rouletting particles.

5. **Time splitting/Russian roulette:** Like energy splitting/roulette, but based on time.

6. **Weight cutoff/Russian roulette:** If a particle weight becomes so low that the particle becomes insignificant, it undergoes Russian roulette. Most particles are killed, and some particles survive with increased weight.

7. **Weight window:** As a function of energy, geometrical location, or both, low-weighted particles are eliminated by Russian roulette and high-weighted particles are split.

8. **Exponential transformation:** To transport particles long distances, the distance between collisions in a preferred direction is artificially increased and the weight is correspondingly artificially decreased.

9. **Implicit absorption:** When a particle collides, there is a probability that it is absorbed by the nucleus. In analog absorption, the particle is killed with that probability. In implicit absorption, also known as implicit capture or survival biasing, the particle is never killed by absorption; instead, its weight is reduced by the absorption probability at each collision.

10. **Forced collisions:** A particle can be forced to undergo a collision each time it enters a designated cell that is almost transparent to it.

11. **Point and ring detectors:** When the user wishes to tally a flux-related quantity at a point in space, the probability of transporting a particle precisely to that point is vanishingly small. Therefore, pseudoparticles are directed to the point instead. Every time a particle history is born in the source or undergoes a collision, the user may require that a pseudoparticle be tallied at a specified point in space. In this way, many pseudoparticles of

low weight reach the detector, which is the point of interest, even though no particle histories could ever reach the detector. For problems with rotational symmetry, the point may be represented by a ring to enhance the efficiency of the calculation.

12. **DXTRAN:** DXTRAN, which stands for deterministic transport, improves sampling in the vicinity of detectors or other tallies. It involves deterministically transporting particles on collision to some arbitrary, user-defined sphere in the neighborhood of a tally and then calculating contributions to the tally from these particles.

13. **Correlated sampling:** The sequence of random numbers in the Monte Carlo process is chosen so that statistical fluctuations in the problem solution will not mask small variations in that solution resulting from slight changes in the problem specification. The ith history will always start at the same point in the random number sequence no matter what the previous i-1 particles did in their random walks.

2.1.4 MCNP Geometry

The geometry of MCNP treats an arbitrary 3-dimensional configuration of user-defined materials in geometric cells bounded by first- and second-degree surfaces and fourth-degree elliptical tori. The cells are defined by the intersections, unions, and complements of the regions bounded by the surfaces. Surfaces are defined by supplying coefficients to the analytic surface equations or, for certain types of surfaces, known points on the surfaces. MCNP also provides a macro-body capability, where basic shapes such as spheres, boxes, cylinders, etc., may be combined using boolean operators. MCNP has a more general geometry than is

available in most combinatorial geometry codes. In addition to the capability of combining several predefined geometrical bodies, as in a combinatorial geometry scheme, MCNP gives the user the added flexibility of defining geometrical regions from all the first and second degree surfaces of analytical geometry and elliptical tori and then of combining them with boolean operators. The following sections describe the definition of cell and surface.

1) Cell

In defining cells, an important concept is that of the sense of all points in a cell with respect to a bounding surface. For example, if the surface defined by x-3 = 0, the points are said to have a negative sense with respect to that surface if it less than 3 and, conversely, a positive sense if it greater than or equal to 3. Cells are defined on cells cards. Each cell is described by a cell number, material number, and material density followed by a list of operators and signed surfaces that bound the cell. If the sense is positive, the sign can be omitted. The material number and material density can be replaced by a single zero to indicate a void cell. The cell number must begin in columns 1-5. The remaining entries follow, separated by blanks. Each surface divides all space into two regions, one with positive sense with respect to the surface and the other with negative sense. The geometry description defines the cell to be the intersection, union, and/or complement of the listed regions. More details can be obtained from MCNP user manual (X-5 Monte Carlo Team, 2003).

2) Surface

The first- and second-degree surfaces plus the fourth-degree elliptical and degenerate tori of analytical geometry are all available in MCNP. The surfaces are designated by mnemonics such as C/Z for a cylinder parallel to the z-axis. A cylinder at an arbitrary orientation is designated by the general quadratic GQ mnemonic.

A paraboloid parallel to a coordinate axis is designated by the special quadratic SQ mnemonic. The 29 mnemonics representing various types of surfaces are listed in Table 3.1 on page 314 of MCNP user manual.

The surface number is the first entry which must begin in columns 1-5 and not exceed 5 digits. The next entry is an alphabetic mnemonic indicating the surface type. Following the surface mnemonic are the numerical coefficients of the equation of the surface in the proper order.

The first way to define a surface is to use one of the surface-type mnemonics from Table 3.1 on MCNP manual page 313 (X-5 Monte Carlo Team, 2003) and to calculate the appropriate coefficients needed to satisfy the surface equation. For example, a sphere of radius 3.62 cm with the center located at the point (4,1,3) is specified by S 4 1 3 3.62

The second way to define a surface is to supply known points on the surface. This method is convenient if you are setting up a geometry from something like a blueprint where you know the coordinates of intersections of surfaces or points on the surfaces. When three or more surfaces intersect at a point, this second method also produces a more nearly perfect point of intersection if the common point is used in the surface specification. It is frequently difficult to get complicated surfaces to meet at one point if the surfaces are specified by the equation coefficients. Failure to achieve such a meeting can result in the unwanted loss of particles.

2.1.5   MCNP Input

The main input file for the user is the INP (the default name) file that contains the input information to describe the problem. We will present here only the subset of cards required to run the simple fixed source demonstration problem. All input cards are discussed in Chapter III and summarized in Table 3.8 starting on page 3148 of the MCNP user manual.

The units used are:

1. lengths in centimeters,

2. energies in MeV,

3. times in shakes (10^{-8} sec),

4. temperatures in MeV (kT),

5. atomic densities in units of atoms/barn-cm,

6. mass densities in g/cm^3,

7. cross sections in barns (10-24 cm^2),

8. heating numbers in MeV/collision, and

9. atomic weight ratio based on a neutron mass of 1.008664967.

In these units, Avogadros number is $0.59703109 \times 10^{-24}$.

An input file has the following form:

```
Message Block (optional)

Blank Line Delimiter (optional)

One Line Problem Title Card

Cell Cards

::

Blank Line Delimiter

::

Surface Cards

::

Blank Line Delimiter

Data Cards

::

Blank Line Terminator (optional)
```

The below sample problem input deck is for the problem of 14-MeV neutrons at a point isotropic source in the center of a small sphere of oxygen that is embedded

in a cube of carbon. A small sphere of iron is also embedded in the carbon. The carbon is a cube 10 cm on each side; the spheres have a 0.5-cm radius and are centered between the front and back faces of the cube. We wish to calculate the total and energy-dependent flux in increments of 1 MeV from 1 to 14 MeV, where bin 1 will be the tally from 0 to 1 MeV. Full input file show as follow;

```
Sample Problem Input Deck
c cell cards for sample problem
1 1 -0.0014 -7
2 2 -7.86 -8
3 3 -1.60 1 -2 -3 4 -5 6 7 8
4 0 -1:2:3:-4:5:-6
c end of cell cards for sample problem
C Beginning of surfaces for cube
1 PZ -5
2 PZ 5
3 PY 5
4 PY -5
5 PX 5
6 PX -5
C End of cube surfaces
7 S 0 -4 -2.5 .5 $ oxygen sphere
8 S 0 4 4.5 $ iron sphere
blank line delimiter
IMP:N 1 1 1 0
SDEF POS=0 -4 -2.5
F2:N 8 $ flux across surface 8
```

```
F4:N 2 $ track length in cell 2

E0 1 12I 14

M1 8016 1 $ oxygen 16

M2 26000 1 $ natural iron

M3 6000 1 $ carbon

NPS 100000

blank line delimiter (optional)
```

2.2 Gamma ray interactions with matter

Since MCNP simulations in this thesis involve using the theory of gamma ray interaction with material as a basis for studying the average behavior of gamma ray propagation in materials, the descriptions of gamma ray interaction with material will be described in the following sections (Lamarsh and Baratta, 2001).

2.2.1 Interaction Process

When the gamma ray interact with the material, three different processes, namely, photoelectric absorption, Compton scattering and pair production are involved. The following sections describe the descriptions of these processes.

1) Photoelectric Absorption

When a gamma ray may interacts with a bound atomic electron in such a way that it loses all of its energy and ceases to exist as a gamma ray (see Figure 2.2), some of the gamma ray energy is used to overcome the electron binding energy, and most of the remainder is transferred to the freed electron as kinetic energy.

A very small amount of recoil energy remains with the atom to conserve momentum. Photoelectric absorption is important for gamma ray detection because
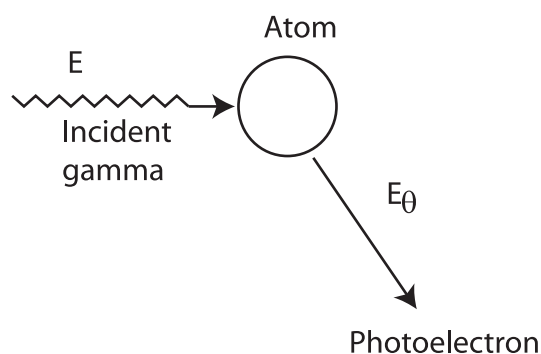
Figure 2.2 A schenratic representation of the photoelectric absorption process.

the gamma ray gives up all its energy, and the resulting pulse falls in the full-energy peak. The probability of photoelectric absorption depends on the gamma ray energy, the electron binding energy, and the atomic number of the atom. The probability is greater then the more tightly bound electron. Therefore, K electrons are most affected (over 80% of the interactions involve K electrons), provided the gamma ray energy exceeds the K-electron binding energy. The probability is given approximately by equation (2.5), which shows that the interaction is more important for heavy atoms like lead and uranium and low-energy gamma rays:

$$\tau \propto Z^4/E^3 \tag{2.5}$$

where τ = photoelectric mass attenuation coefficient.

The proportionality is only approximate because the exponent of Z varies in the range 4.0 to 4.8. As the gamma ray energy decreases, the probability of photoelectric absorption increases rapidly (Figure 2.3). Photoelectric absorption is the predominant interaction for low-energy gamma rays, x-rays, and bremsstrahlung. The energy of the photoelectron E_e, released by the interaction is the difference between the gamma ray energy E_γ and the electron binding energy E_b.

$$E_e = E_\gamma - E_b \tag{2.6}$$
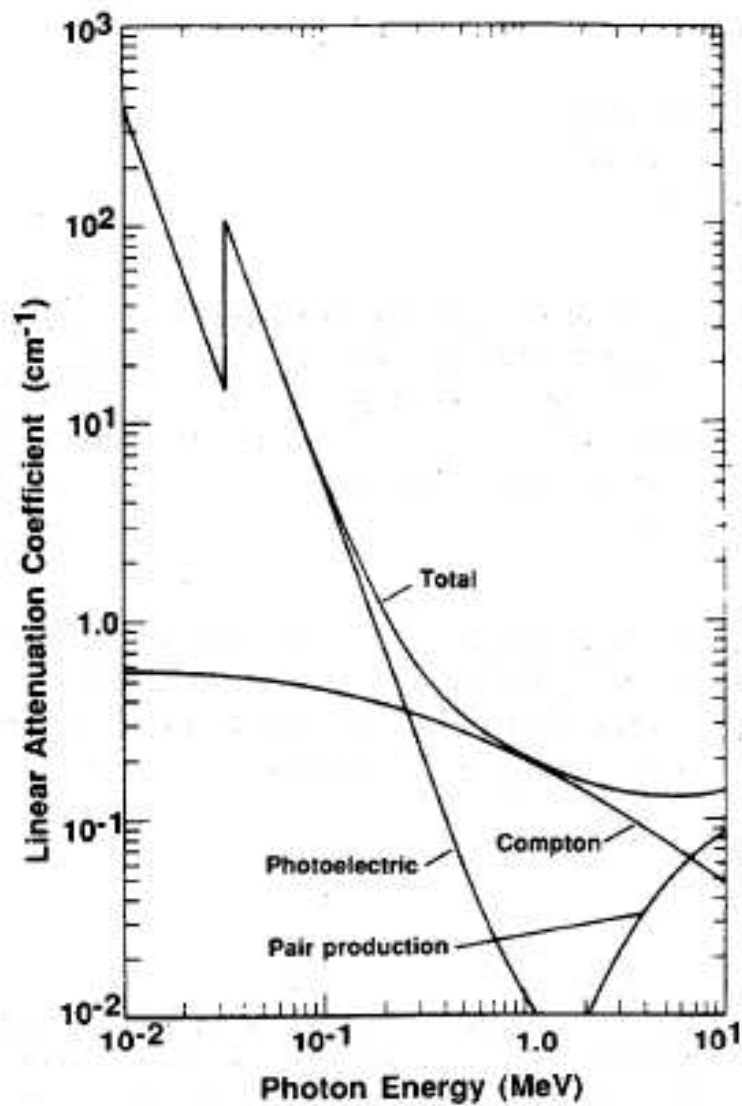
Figure 2.3 Linear attenuation coefficient of NaI showing contributions from photoelectric absorption, Compton scattering, and Pair production (Reilly et al., 1991).

In most detectors, the photoelectron is stopped quickly in the active volume of the detector, which emits a small output pulse whose amplitude is proportional to the energy deposited by the photoelectron. The electron binding energy is not lost but appears as characteristic x-rays emitted in coincidence with the photoelectron. In most cases, these x-rays are absorbed in the detector in coincidence with the photoelectron and the resulting output pulse is proportional to the total energy of the incident gamma ray. For low-energy gamma rays in very small detectors, a sufficient number of K x-rays can escape from the detector to cause escape peaks in the observed spectrum; the peaks appear below the full-energy peak by an amount equal to the energy of the x-ray. Figure 2.4 shows the photoelectric mass attenuation coefficient of lead. The interaction probability increases rapidly as energy decreases, but then becomes much smaller at a gamma ray energy just below the binding energy of the K electron. This discontinuity is called the K edge below this energy the gamma ray does not have sufficient energy to dislodge a K electron. Below the K edge the interaction probability increases again until the energy drops below the binding energies of the L electron. These discontinuities are called the LI, LII and $LIII$ edges
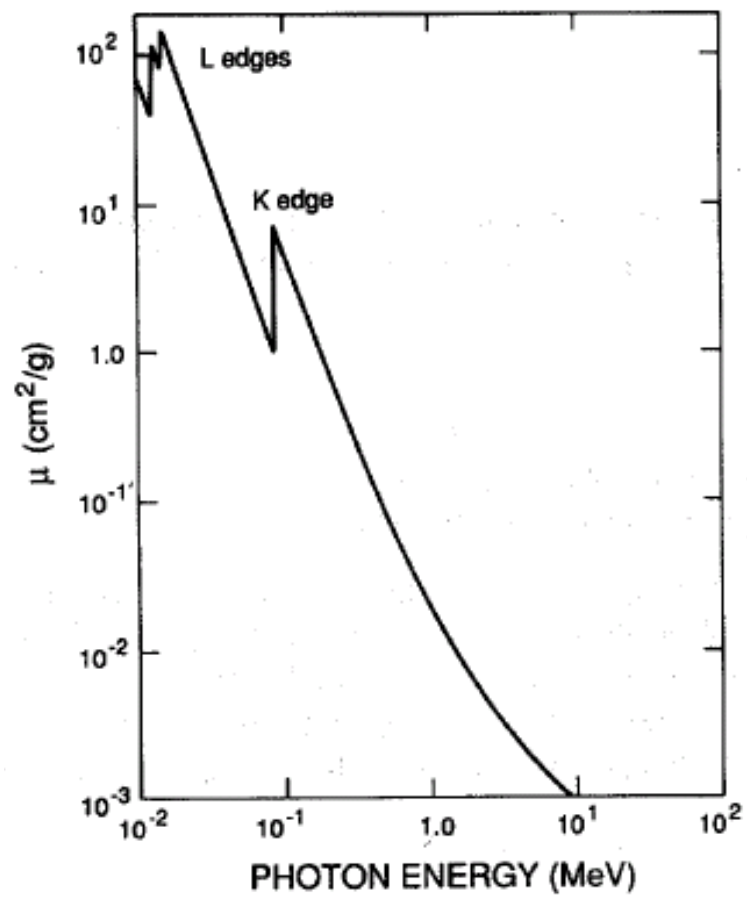
Figure 2.4 Photoelectric mass attenuation coefficient of lead (Reilly et al., 1991).

2) Compton Scattering

Compton scattering is the process whereby a gamma ray interacts with a free or weakly bound electron ($E_\gamma >> E_b$) and transfers part of its energy to the electron (see Figure 2.5). Conservation of energy and momentum allows only a partial energy transfer when the electron is not bound tightly enough for the atom to absorb recoil energy. This interaction involves the outer, least tightly bound electrons in the scattering atom. The electron becomes a free electron with kinetic energy equal to the difference of the energy lost by the gamma ray and the electron binding energy.
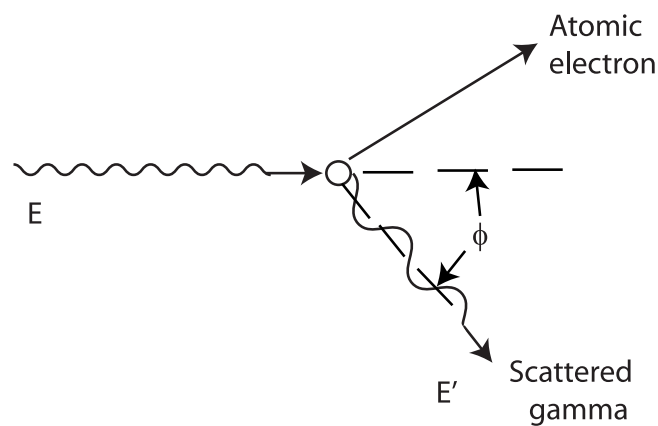
Figure 2.5 A schematic representation of Compton scattering.

Because the electron binding energy is very small compared to the gamma ray energy, the kinetic energy of the electron is very nearly equal to the energy lost by the gamma ray:

$$E_e = E_\gamma - E' \tag{2.7}$$

where $\quad E_e$ = energy of scattered electron

$\qquad E_\gamma$ = energy of incident gamma ray

$\qquad E'$ = energy of scattered gamma ray

Two particles leave the interaction site: the freed electron and the scattered gamma ray. The directions of the electron and the scattered gamma ray depend on the amount of energy transferred to the electron during the interaction. equation (2.8) gives the energy of the scattered gamma ray.

$$E' = m_0 c^2 / (1 - \cos\phi + m_0 c^2 / E) \tag{2.8}$$

This energy is minimum for a head-on collision where the gamma ray is scattered 180° and the electron moves forward in the direction of the incident gamma ray.
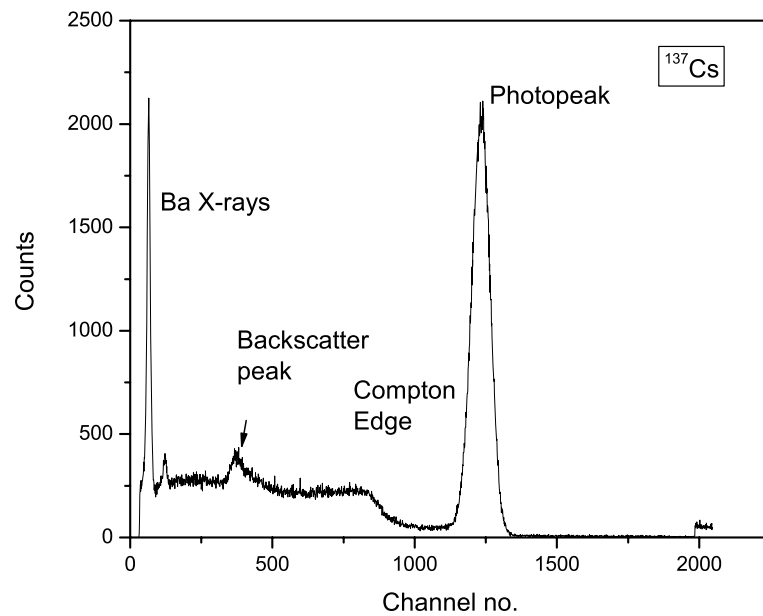
Figure 2.6 High-resolution spectrum of ^{137}Cs showing full-energy photo peak, Compton edge, and backscatter peak from the 662- keV gamma ray. Events below the photopeak are caused by Compton scattering in the detector and surrounding materials.

When a Compton scattering occurs in a detector, the scattered electron is usually stopped in the detection medium and the detector produces an output pulse that is proportional to the energy lost by the incident gamma ray. Figure 2.6 shows the measured gamma ray spectrum from a monoenergetic gamma

ray source (^{137}Cs). The full-energy peak at 662 keV is formed by interactions where the gamma ray loses all of its energy in the detector either by a single photoelectric absorption or by a series of Compton scattering followed by photoelectric absorption. The spectrum of events below the full-energy peak is formed by Compton scattering where the gamma ray loses only part of its energy in the detector. The step near 470 keV corresponds to the maximum energy that can be transferred to an electron by a 662-keV gamma ray in a single Compton scattering. The small peak at 188 keV in Figure 2.6 is called a backscatter peak. The sum of the energy of the backscatter peak and the Compton edge equals the energy of the incident gamma ray.

3) Pair production

A gamma ray with an energy of at least 1.022 MeV can create an electron-positron pair when it is under the influence of the strong electromagnetic field in the vicinity of a nucleus (see Figure 2.7). In this interaction the nucleus receives a very small amount of recoil energy to conserve momentum, but the nucleus is otherwise unchanged and the gamma ray disappears. This interaction has a threshold of 1.022 MeV which is the minimum energy required to create the electron and positron. If the gamma ray energy exceeds 1.022 MeV, the excess energy is shared between the electron and positron as their kinetic energies.
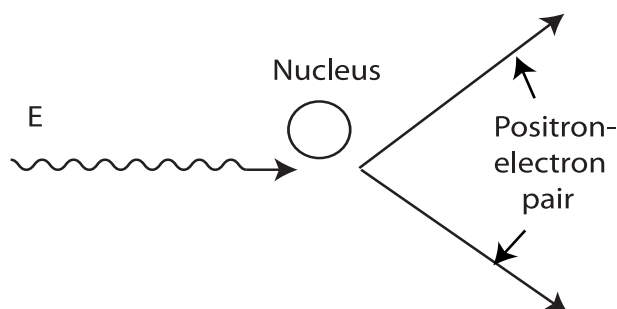
Figure 2.7 A schematic representation of pair production.

The electron and positron from pair production are rapidly slowed down in the absorber. After losing its kinetic energy, the positron combines with an electron in an annihilation process, which releases two gamma rays with energies of 0.511 MeV. These lower energy gamma rays may interact further with the absorbing material or may escape. In a gamma ray detector, this interaction often gives three peaks for a high-energy gamma ray (see Figure 2.8). The kinetic energies of the electron and positron are absorbed in the detector.
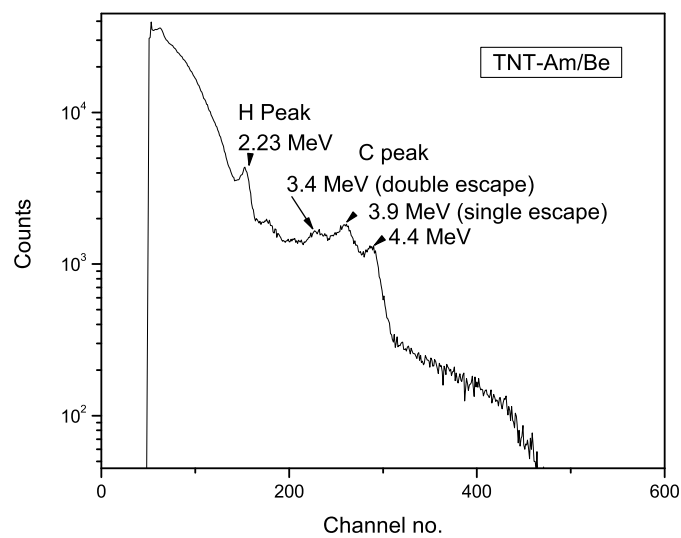
Figure 2.8 gamma ray spectrum of the ^{12}C showing single-escape (SE) and double-escape (DE) peaks (3.4 and 3.9) that arise from pair-production inter-actions of 4.4- MeV gamma rays in a NaI detector.

One or both of the annihilation gamma rays may escape from the detector or they may both be absorbed. If both annihilation gamma rays are absorbed in the detector, the interaction contributes to the full-energy peak in the measured spectrum; if one of the annihilation gamma rays escapes from the detector, the interaction contributes to the single-escape peak located 0.511 MeV below the

full-energy peak; if both gamma rays escape, the interaction contributes to the double-escape peak located 1.022 MeV below the full-energy peak. The relative heights of the three peaks, depend on the energy of the incident gamma ray and the size of the detector.

2.2.2   Gamma Ray Attenuation

1) The Fundamental Law of gamma ray Attenuation

Figure 2.9 illustrates a simple attenuation experiment and attenuation curve. When gamma radiation of intensity I_o is incident on an absorber of thickness L, the emerging intensity (I) transmitted by the absorber is given by the exponential expression
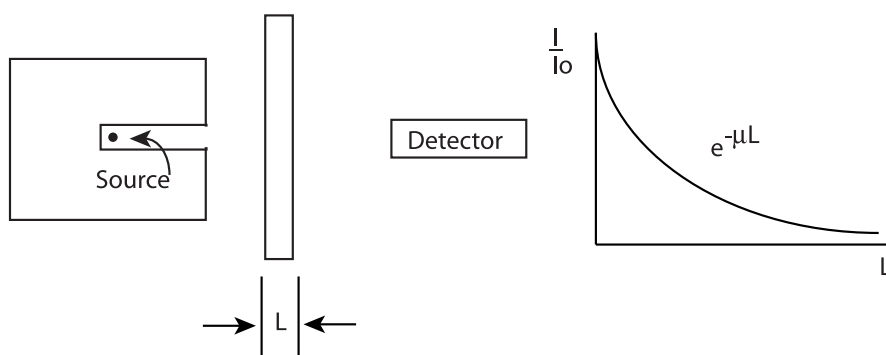
Figure 2.9 Attenuation experimental setup and attenuation curve.

$$I = I_o e^{-\mu_l L} \tag{2.9}$$

where μ_l is the linear attenuation coefficient (expressed in cm^{-1}). Figure 2.10 illustrates exponential attenuation in lead for three different gamma ray energies and shows that the transmission increases with increasing gamma ray energy and decreases with increasing absorber thickness. Measurements with

different sources and absorbers show that the linear attenuation coefficient μ_l depends on the gamma ray energy and the atomic number (Z) and density (ρ) of the absorber. For example, lead has a high density and atomic number and transmits a much lower fraction of incident gamma radiation than does a similar thickness of aluminum or steel. Figure 2.3 shows the linear attenuation of solid sodium iodide, a common material used in gamma ray detectors.
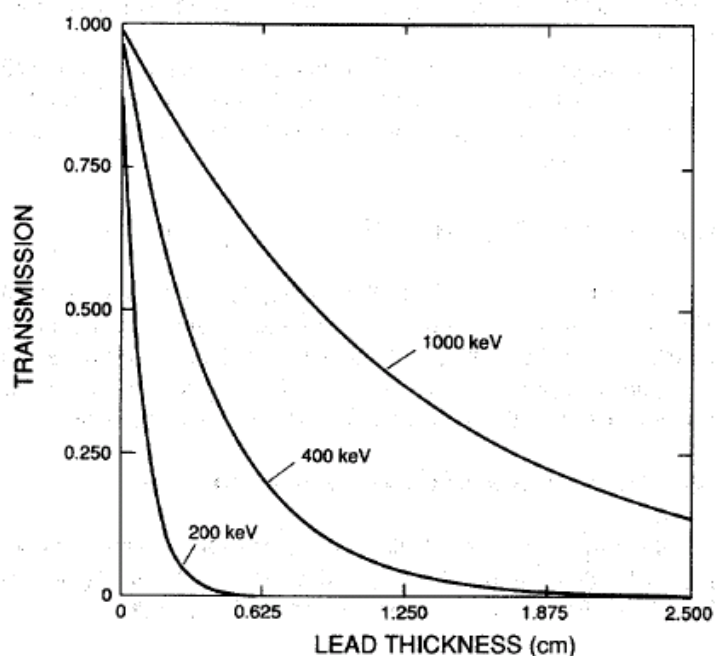
Figure 2.10 Transmission of gamma rays through lead absorbers (Reilly et al., 1991).

2) Mass Attenuation Coefficient

The linear attenuation coefficient is the simplest absorption coefficient to measure experimentally, but it is not usually tabulated because of its dependence on the density of the absorbing material. For example, at a given energy, the linear attenuation coefficients of water, ice, and steam are all different, even though the same material is involved.

The ratio of the linear attenuation coefficient to the density (μ_l/ρ) is called the mass attenuation coefficient μ and has the dimensions of area per unit mass (cm^2/g). The units of this coefficient hint that one may think of it as the effective cross-sectional area of electrons per unit mass of absorber. The mass attenuation coefficient can be written in terms of a reaction cross section, $\sigma(\text{cm}^2)$:

$$\mu = \frac{N_0\sigma}{A} \tag{2.10}$$

where N_o is Avogadros number (6.02×10^{23}) and A is the atomic weight of the absorber. The cross section is the probability of a gamma ray interacting with a single atom. Using the mass attenuation coefficient, equation (2.9) can be rewritten as

$$I = I_0 e^{-\mu\rho L} = I_0 e^{-\mu x} \tag{2.11}$$

where $x = \rho L$

Taking the natural logarithmic of equation (2.11), we can prove that

$$\ln\left(\frac{Io}{I}\right) = \rho\mu L \tag{2.12}$$

equation (2.12) implies that for a certain absorber with known thickness and mass attenuation coefficient, the quantity $\ln(I_0/I)$ is proportional to the absorber density.

3) Buildup

The gamma ray attenuation experiment of Figure 2.9, in which the gamma rays are collimated to a narrow beam before striking the absorber, is sometimes characterized as a "narrow beam" or "good geometry" measurement. The essential characteristic is that only gamma rays from the source which escape interaction in the absorber can be counted by the detector. Real measurements are often carried out under different circumstances as Figure 2.11 in which the severe collimation

of the gamma rays is absent.
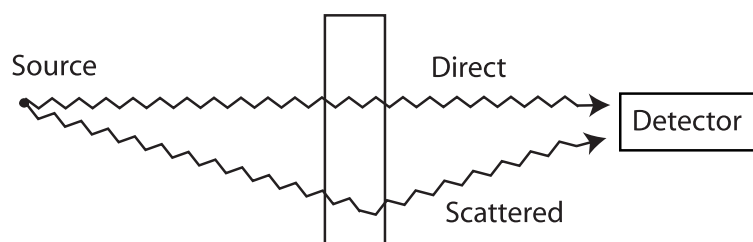
Figure 2.11 A schematic representation of uncollimated gamma ray

Now the detector can respond either to gamma rays directly from the source , to gamma rays that reach the detector after having scattered in the absorber, or to other types of secondary photon radiation. Many types of detectors will be unable to distinguish between these possibilities, so that the measured detector signal will be larger than that recorded under equivalent "good geometry" conditions. The conditions that lead to the simple exponential attenuation of equation (2.9) are therefore violated in this "broad beam" or "bad geometry" measurement because of the additional contribution of the secondary gamma rays. This situation is usually handled by replacing equation (2.9) by the following:

$$\frac{I}{I_o} = B(x, E_\gamma)e^{-\mu x} \tag{2.13}$$

where the factor $B(x, E_\gamma)$ is called the buildup factor. The exponential term is retained to describe the major variation of the gamma ray counting rate with absorber thickness, and the buildup factor is introduced as a simple multiplicative correction. The magnitude of the buildup factor depends on the type of gamma ray detector used, because this will affect the relative weight given to the direct and secondary gamma rays. The buildup also depends on the specific geometry of the experiment.

2.3 Neutron Interaction with Matter

When neutrons interact with materials, the following processes are possible, namely, the elastic neutron scattering, the inelastic neutron scattering, the radiative neutron capture and the fission. The characteristics of these processes will be described in the following sections (Lamarsh and Baratta, 2001; Reilly et al., 1991).

2.3.1 Elastic Neutron Scattering

In elastic neutron scattering both kinetic energy and momentum are conserved. Thus the simple billiard-ball collision model can be used to obtain the direction of motion and the speed of the scattered neutron and recoiling nucleus relative to the direction and speed (or energy) of the incident neutron.

Actually two processes are assumed to produce elastic scattering of neutrons. The first is known as resonance or capture scattering. In this process the neutron is assumed to be absorbed by the target nucleus and re-emitted in (possibly) another direction. The second process is called potential or diffraction scattering. In this process the neutron is assumed not to enter the target nucleus but rather to be elastically scattered by interaction with the potential well created around the nucleus by the short-range nuclear forces. The probability for elastic scatter is the sum of the probabilities for both processes; the cross section for elastic scattering is based on this sum and is often denoted by σ_{es}. In adding these probabilities, we must take account of the spin states of the particles since coherent effects are involved.

The scattering angle-energy relations for elastic interactions are given most simply in the center-of-mass coordinate system in which the total momentum is constant zero, and particle speeds after collision are equal to those before collision.
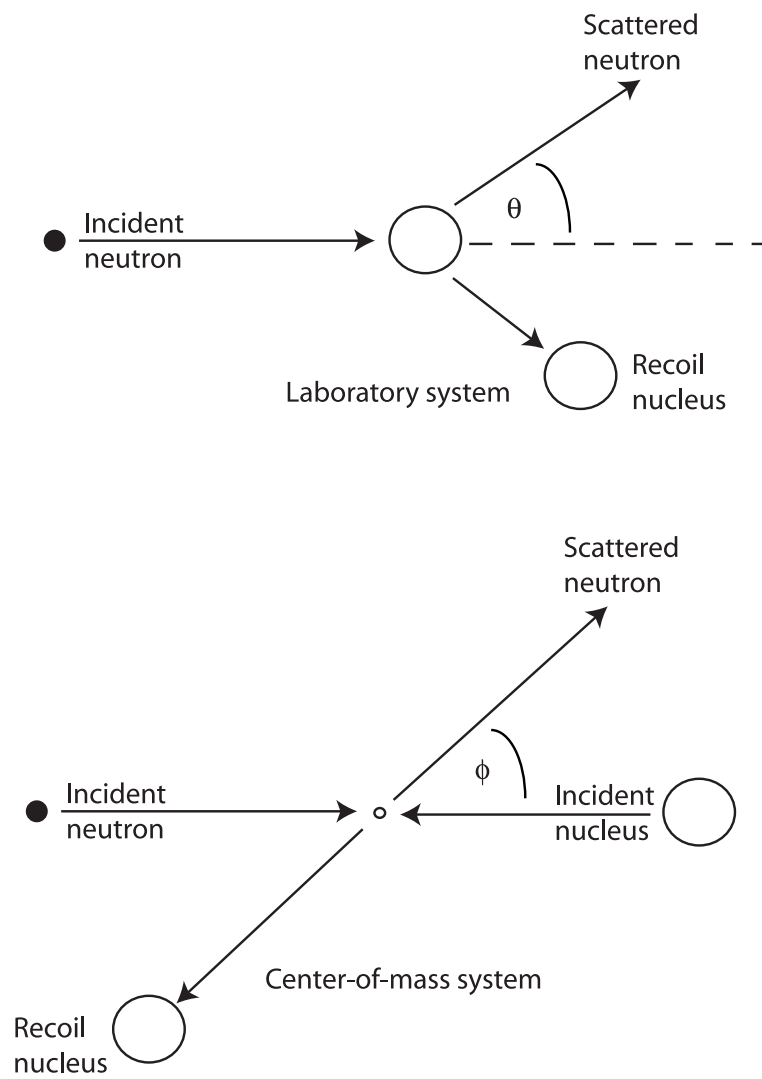
Figure 2.12 A schenratic representation of collision coordinate systems

Figure 2.12 illustrates the collision geometry in both the laboratory and the center-of-mass systems. The energy, E, of the elastically scattered neutron is related to the energy, E_0, of the incident neutron, the atomic mass, A, of the target nucleus, and the scattering angle, ϕ (in the center-of-mass system), by the equation

$$\frac{E}{E_0} = \frac{A^2 + 2A\cos\phi + 1}{(A+1)^2} \qquad (2.14)$$

The scattering angle, θ, in the laboratory system is related to ϕ by the equation

$$\cos\theta = \frac{A\cos\phi + 1}{(A^2 + 2A\cos\phi + 1)^{1/2}} \qquad (2.15)$$

It is seen that for hydrogen scattering ($A=1$) the neutron can lose all its energy in just one collision. Maximum energy loss occurs where $\phi = \pi$, and equation (2.14) becomes

$$\frac{E_{\min}}{E_0} = \left(\frac{A-1}{A+1}\right)^2 \qquad (2.16)$$

For low-energy neutrons elastic scattering is approximately isotropic in the center-of-mass system, and the average scattering angle in the laboratory system is given by

$$\cos\bar{\theta} = \frac{3}{3A} \qquad (2.17)$$

Equation (2.17) illustrates the point that scattering (in the laboratory system) is peaked in the forward direction ($1 > \cos\bar{\theta} > 0$) and that, as A increases, $\bar{\theta}$ approaches $\pi/2$. Thus, for low energies and heavy nuclei, scattering approaches isotropy in the laboratory system as well.

2.3.2 Inelastic Neutron Scattering

In inelastic neutron scattering the inelastic collision differs from an elastic event primarily in that a portion of the incident-neutron energy appears as exci-

tation of the target nucleus. The excited nucleus subsequently decays by photon emission. The inelastically scattered neutron leaves the collision site usually altered in direction and generally with much-reduced energy as well. In fact, inelastic scattering is an important means of reducing fast (E > 1 MeV) neutron energies in reactor shields not only because a large amount of energy can be transferred to the nucleus in one inelastic collision but also because of the increasing importance of inelastic scattering with energy in the 1- to 14-MeV range. For most elements of interest, elastic-scattering cross sections are slowly oscillating, generally decreasing in the fast-energy region. Since inelastic scattering is a threshold reaction, the corresponding cross section usually increases with increasing energy.

Inelastic scattering cannot occur unless the incident neutron has a kinetic energy somewhat greater than the first excited state of the target nucleus. Depending on the nucleus, this threshold varies from 0.1 to 4 or 5 MeV. As the neutron kinetic energy exceeds energy states of the nucleus above the first, these higher states may also become excited, and thus the neutron may excite the nucleus to any level up to the limit of the incident-neutron energy. As the excitation energy is increased, spacing between levels decreases until a continuum is reached. For a given nuclear species and neutron energy, there is a fixed probability for exciting each energy level. For all but the first level, there are alternate routes by which the nucleus may release the excitation energy:

2.3.3   Neutron Radiative Capture

For neutron energies in the lower ranges, radiative capture competes in importance with the elastic-scattering process. In radiative capture the incident neutron is absorbed by the target nucleus; the compound nucleus is almost invariably left in an excited state and decays in a variety of ways, emitting one or more

gamma rays. The total excitation energy is equal to the energy of the incident neutron plus the neutron binding energy.

The binding energy of neutrons varies from 3.2 MeV in hydrogen to 11 MeV in nitrogen, averaging about 7 MeV. Thus energetic gamma rays can be emitted. The probability for the emission of such a photon is highest in light and magic nuclei. If, however, the compound nucleus formed by the absorption has energy levels lower than the combined binding and kinetic energies of the incident neutron, a gamma ray cascade can result. Recent theoretical work in the prediction of the gamma ray spectra from capture reactions is discussed by IAEA report (Choi, 1999). More recent data can be found in the journal of Nuclear Data.

The thermal-neutron cross sections for radiative capture in most elements and isotopes are given in the famous "barn book". Therefore the total energy emitted as gamma rays is almost equal to the neutron binding energy because the energy of the incident neutron is generally quite small by comparison (Schaeffer, 1973).

2.3.4   Fission

Neutrons colliding with certain nuclei may cause the nucleus to split apart to undergo fission. This reaction is the principal source of nuclear energy for practical applications.

Many of these reactions may be viewed as a two-step process involving the a compound nucleus. For example, the scattering reactions, both elastic and inelastic, may be thought of as a process in which the neutron is first absorbed by the target nucleus to form a new nucleus whose atomic number is unchange but whose mass number is increased by 1. Then depending on the specific process, the nucleus decays via neutron emission to produce the original nucleus plus a

neutron. The product nucleus is left in the ground state or an excited state according to the type of scattering reaction involved. This model is particularly useful in understanding the fission process. Each of these interactions is discussed in this chapter. However, to describe quantitatively the various interactions, it is necessary to introduce certain parameters.

2.3.5 Neutron Cross Sections
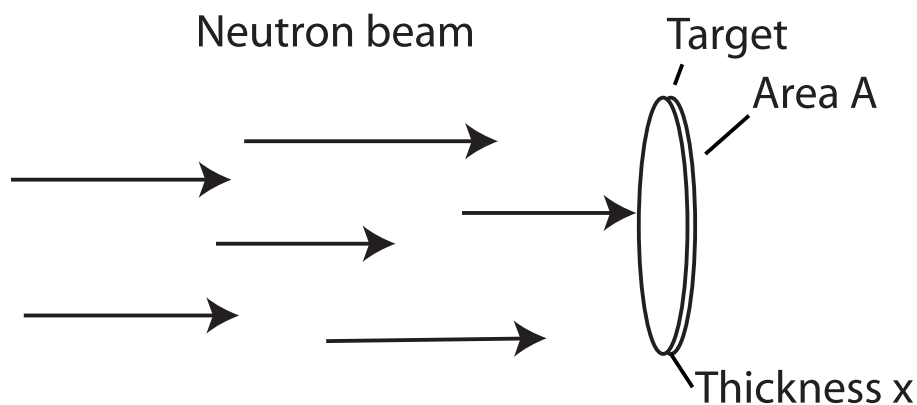
Figure 2.13 Principle of neutron cross section.

When neutrons interact with nuclei, the probabilities of different interaction can be described in terms of cross-sections. These are defined by the experiment as shown in Figure 2.13. Suppose that a beam of monoenergetic neutrons impinges on a thin target of thickness X and area A as shown in Figure 2.13, if there are n neutron per cm^3 in the beam and v is the speed of the neutrons, then the quantity

$$I = nv \tag{2.18}$$

is called the intensity of the beam. Since the neutrons travel the distance v cm in 1 sec, all of the neutrons in the volume vA in front of the target will hit the target in 1 sec. Thus, $nvA = IA$ neutrons strike the entire target per second. Therefore, $IA/A=I$ is equal to the number of neutrons striking the target per cm^2/sec. Since
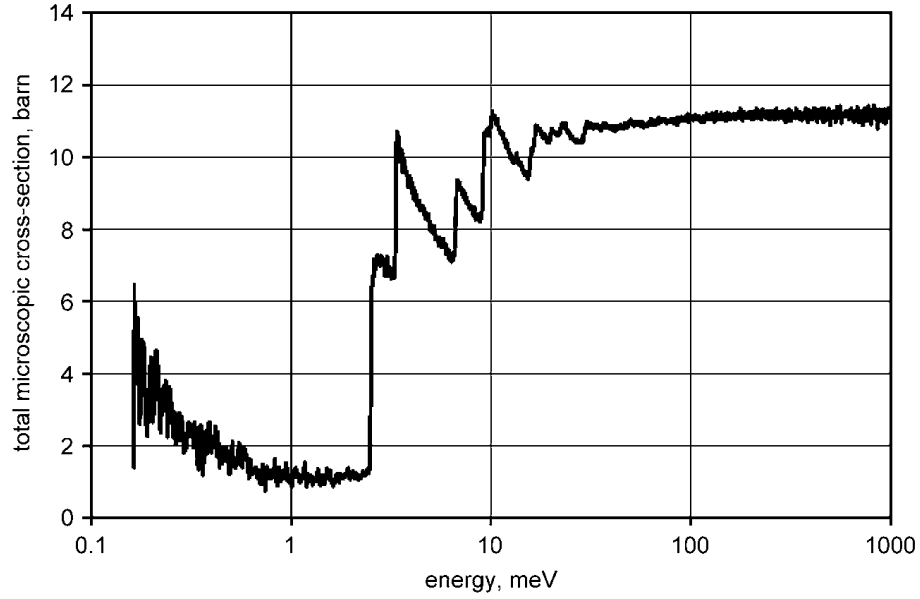
Figure 2.14 Total microscopic cross-section for Pb (Muhrer et al., 2007).

nuclei are small and the target is assumed to be thin, most of the neutrons striking the target pass through the target without interacting with any of the nuclei. The number of neutron collisions are found to be proportional to the beam intensity, to the atom density N of target, and to the area and thickness of the target. These observations can be summarized by the equation below.

$$\text{Number of collisions per second (in entire target)} = \sigma I N A X \qquad (2.19)$$

where σ, the proportionality constant, is called the cross-section. The factor NAX in equation (2.19) is the total number of nuclei in the target. The number of collisions per second with a single nucleus is therefore equal to σI. It follows that σ is equal to the number of collisions per second with one nucleus per unit intensity of the beam. There is another way to view the concept of cross-section. As already noted, IA neutrons strike the target per second. Of these, σI interact with any given nucleus. Therefore, it may be concluded that

$$\frac{\sigma I}{AI} = \frac{\sigma}{A} \qquad (2.20)$$

is equal to the probability that a neutron in the beam will collide with this nucleus. It is clear from equation (2.20) that σ has units of area. In fact, it is not difficult to see that σ is nothing more than the effective cross-sectional area of the nucleus, hence the term cross-section. Neutron cross-sections are expressed in units of barns, where 1 barn, abbreviated b, is equal to 10^{-24} cm^2. One thousandth of a barn is called a millibarn, denoted as mb. Up to this point, it has been assumed that the neutron beam strikes the entire target. However, in many experiments, the beam is actually smaller in diameter than the target.In this case, the prior formulas still hold, but now A refers to the area of the beam instead of the area of the target. The definition of cross-section remains the same, of course.

Each of the processes by which neutrons interact with nuclei is denoted by a characteristic cross-section.Thus, elastic scattering is described by the elastic scattering cross-section, σ_e; inelastic scattering by the inelastic scattering cross-section, σ_i; the (n, γ) reaction (radiative capture) by the capture cross-section, σ_γ; fission by the fission cross-section, σ_f; and so on. The sum of the cross-sections for all possible interactions is known as the total cross-section and is denoted by the symbol σ_t; that is

$$\sigma_t = \sigma_e + \sigma_i + \sigma_\gamma + \sigma_f + ... \tag{2.21}$$

The total cross-section measures the probability that an interaction of any type will occur when neutrons strike a target. The sum of the cross-sections of all absorption reactions is known as the absorption cross-section and is denoted by σ_a. Thus

$$\sigma_a = \sigma_\gamma + \sigma_f + \sigma_p + \sigma_\alpha + ... \tag{2.22}$$

where σ_p and σ_α are the cross-sections for the (n, p) and (n, α) reactions. As indicated in equation (2.22), fission, by convention, is treated as an absorption process. Similarly, the total scattering cross-section is the sum of the elastic and

inelastic scattering cross-section. Thus,

$$\sigma_s = \sigma_e + \sigma_i, \tag{2.23}$$

and

$$\sigma_t = \sigma_s + \sigma_a. \tag{2.24}$$

where σ_t has been introduced because this cross-section measures the probability that a collision of any type may occur. Since AX is the total volume of the target, it follows that the number of collisions per cm^3/sec in the target, which is called the collision density F, is given by

$$F = IN\sigma_t. \tag{2.25}$$

The product of the atom density N and a cross-section, as in equation (2.25), occurs frequently in the equations of nuclear engineering; it is given the special symbol Σ and is called the macroscopic cross-section. In particular, the product $N\sigma_t{=}\Sigma_t$ is called the macroscopic total cross-section, $N\sigma_s{=}\Sigma_s$ is called the macroscopic scattering cross-section, and so on. Since N and σ have units of cm^{-3} and cm^2 respectively, Σ has units of cm^{-1}. In terms of the macroscopic cross-section, the collision in equation (2.25) reduces to

$$F = I\Sigma_t. \tag{2.26}$$

2.3.6   Neutron Sources

We may categorize neutrons into four different groups of energies as the followings (Uckan et al., 2003).

1) Slow or thermal neutrons with energy below 0.5 eV. 2) Intermediate neutron with energies between 0.5 eV to 10 keV. 3) Fast neutron with energies between 10

Table 2.2 Radioisotope neutron sources (Kiefer and Maushart, 1972).

Source	Half-life	Reaction	Neutron yield ($n \times s^{-1} \times g^{-1}$)	Neutron energy(MeV)
^{124}Sb-Be	60.9 d	(γ,n)	2.7×10^9	0.024
^{140}La-Be	40.2 h	(γ,n)	10^7	2.0
^{210}Po-Be	138 d	(α,n)	2.28×10^{10}	4.3
^{241}Am-Be	458 y	(α,n)	1.0×10^7	~ 4
^{226}Ra-Be	1620 y	(α,n)	1.3×10^7	~ 4
^{227}Ac-Be	21.8 y	(α,n)	1.1×10^9	~ 4
^{239}Pu-Be	24400 y	(α,n)	10^9	~ 4
^{228}Th-Be	1.91 y	(α,n)	1.7×10^{10}	~ 4
^{252}Cf	2.65 y	fission	2.34×10^{12}	2.3

keV to 14 MeV. 4) Relativistic neutrons with energy above 14 MeV (Kiefer and Maushart, 1972).

There are two types of sources that produce these neutron: 1) Radioisotope neutron source such as fission source based on Cf-252, (α, n) sources and (γ, n) sources (Vega-Carrillo et al., 2002). 2) Accelerator-based neutron source such as proton and deuterium bombardment source, electron bombardment and photo-nuclear reactions source and spallation sources. Table 2.2 shows characteristics of various neutron source and Table 2.3 show those of Cf-252 neutron source.

2.3.7 Neutron Moderation

There are no sources that directly produce thermal neutrons (Tzika and Stamatelatos, 2004), so the moderation of neutrons are needed to reduce

Table 2.3 Characteristics of ^{252}Cf (Reilly et al., 1991).

Total half-life	2.646 yr
Alpha half-life	2.731 yr
Spontaneous fission half-life	85.5 yr
Neutron yield	2.34×10^{12} n/s-g
gamma ray yield	1.3×10^{13} gamma/s-g
Alpha-particle yield	1.9×10^{13} α/s-g
Average neutron energy	2.14 MeV
Average gamma ray energy	1 MeV
Average alpha-particle energy	6.11 MeV
Neutron activity	4.4×10^{9} n/s-Ci
Neutron dose rate	2300 rem/h-g at 1 m
Gamma dose rate	140 rem/h-g at 1 m
Conversion	558 Ci/g
Decay heat	38.5 W/g
Avg.spontaneous fission neutron multiplicity	3.757
Avg.spontaneous fission gamma multiplicity	8

their energies. The processes of source thermalization is accomplished by the slowing-down or moderation of neutrons emitted from fast-neutron sources. Since in this process, a good number of neutrons are lost, by absorption, divergence and leakage, it is important to choose both a source and a moderating material that provide the highest thermal-neutron flux per unit source. The following sections describe about parameters involving thermalization or slowing down neutrons.

1) Neutron Slowing Down and Thermalization

Fission neutrons are produced at an average energy of 2 MeV and immediately begin to slow down as the result of numerous scattering reactions with a variety of target nuclei. After a number of collisions with nuclei, the speed of a neutron is reduced to such an extent that it has approximately the same average kinetic energy as the atoms (or molecules) of the medium in which the neutron is undergoing elastic scattering. This energy, which is only a small fraction of an electron volt at ordinary temperatures (0.025 eV at 20 C), is frequently referred to as the thermal energy, since it depends upon the temperature. Neutrons whose energies have been reduced to values in this region (< 1 eV) are designated thermal neutrons. The process of reducing the energy of a neutron to the thermal region by elastic scattering is referred to as thermalization, slowing down or moderation. The material used for the purpose of thermalizing neutrons is called a *moderator*. A good moderator reduces the speed of neutrons in a small number of collisions, but does not absorb them to any great extent.

The ideal moderating material (moderator) should have the following nuclear properties.

- large scattering cross section
- small absorption cross section

- large energy loss per collision

A convenient measure of energy loss per collision is the logarithmic energy decrement. The *average logarithmic energy decrement* is the *average decrease per collision* in the logarithm of the neutron energy.

$$\xi = \ln E_i - \ln E_f \tag{2.27}$$

$$\xi = \ln\left(\frac{Ei}{Ef}\right) \tag{2.28}$$

where,

ξ = average logarithmic energy decrement,

E_i = average initial neutron energy,

E_f = average final neutron energy.

The symbol ξ is commonly called the average logarithmic energy decrement because of the fact that a neutron loses, on the average, a fixed fraction of its energy per scattering collision. Since the fraction of energy retained by a neutron in a single elastic collision is a constant for a given material, ξ is also a constant. Because it is a constant for each type of material and does not depend upon the initial neutron energy, ξ is a convenient quantity for assessing the moderating ability of a material. The values for the lighter nuclei are tabulated in a variety of sources. The following commonly used approximation may be used when a tabulated value is not available,

$$\xi = \frac{2}{A + \frac{2}{3}} \tag{2.29}$$

This approximation is relatively accurate for mass numbers (A) greater than 10, but for some low values of A it may be in error by over three percent.

2) Macroscopic Slowing Down Power

Although the logarithmic energy decrement is a convenient measure of the

ability of a material to slow neutrons, it does not measure all necessary properties of a moderator. A better measure of the capabilities of a material is the macroscopic slowing down power. The macroscopic slowing down power (MSDP) is the product of the logarithmic energy decrement and the macroscopic cross section for scattering in the material,

$$MSDP = \xi \, \Sigma_s \tag{2.30}$$

equation (2.30) illustrates how to calculate the macroscopic slowing down power.

3) Moderating Ratio

Macroscopic slowing down power indicates how rapidly a neutron will slow down in the material in question, but it still does not fully explain the effectiveness of the material as a moderator. An element such as boron has a high logarithmic energy decrement and a good slowing down power, but it is a poor moderator because of its high probability of absorbing neutrons. The most complete measure of the effectiveness of a moderator is the moderating ratio. The moderating ratio is the ratio of the macroscopic slowing down power to the macroscopic cross section for absorption. The higher the moderating ratio, the more effectively the material performs as a moderator. equation (2.31) shows how to calculate the moderating ratio of a material,

$$MR = \frac{\xi \Sigma_s}{\Sigma_a} \tag{2.31}$$

Moderating properties of different materials are compared in Table 2.4.

Table 2.4 Neutron moderating materials (Hussein, 2003).

Material	Density	Σ_s	Σ_a	ξ	Slowing-down	Moderating
	(Kg/m^3)	cm^{-1}	cm^{-1}		Power	Ratio
H_2O	1000	1.47	0.022	0.925	1.36	62
D_2O	1100	0.35	36x10^{-6}	0.504	0.18	5000
$Paraffin$	950	1.36	0.020	0.913	1.24	62
$(C_{30}H_{62})$						
$Polyethylene$	960	1.80	0.026	0.912	1.64	63
(C_2H_4)						
$Water$	1100	1.62	0.022	1.46	1.46	63
$Extended$						
$Polyester$						
$Glycerin$	1260	1.96	0.027	0.833	1.73	64
$(C_3H_8O_3)$						
$Graphite$	1600	0.38	3.6x10^{-4}	0.158	0.060	165
$Beryllium$	1850	0.76	0.0011	0.206	0.16	145
BeO	3025	0.76	7.23x10^{-4}	0.173	0.13	181
ZrH_2	5600	1.75	0.030	0.84	1.47	49

2.4   Radiation Shielding

In the EDS, two types of radiations are produced. To reduce these radiations, some kinds of shieldings are needed. The following sections describe about gamma ray and neutron shielding:

1) Gamma Ray Shielding

In the EDS, there are two sources of gamma rays; 1) gamma rays from neutron source, called, "primary gamma" and 2) gamma rays from neutron interactions with materials, called, "secondary gamma". To reduce these radiations, shields and collimators are used. gamma ray shielding materials should be of high density and high atomic number so that they have a high total linear attenuation coefficient and a high photoelectric absorption probability. The most common shielding material is lead because it is readily available. It has a density of 11.35 g/cm^3, an atomic number of 82 and is relatively inexpensive. Lead can be molded into many shapes. However, because of its high ductility it cannot be machined easily or hold a given shape unless supported by a rigid material (Yazdi et al., 2004).

2) Neutron Shielding

To protect personnel from the biological effects of neutrons and to reduce background counts, neutron shielding is often necessary. The selection and arrangement of shielding materials vary with the circumstances. Some general principles can be derived from the neutron interactions with matter.Thermal neutrons with energies of 0.025 eV or less are absorbed with great effectiveness by thin layers of boron or cadmium. Boron is often used in the form of boron carbide (B4C) or boron-loaded solutions. One commonly used material is Boric acid. Cadmium has the disadvantage of emitting high-energy gamma rays after neutron capture, which may necessitate additional gamma ray shielding.

2.5   Radiation Exposure and Dose

When one works in the radiation environment, the following quantities are of interest: absorbed dose, dose-equivalent, exposure and activity. They are defined as follows:

Absorbed dose

Absorbed dose is a physical quantity that represents the energy imparted by the radiation to unit mass of any absorbing material. The old unit of dose is "rad", defined as an energy absorption of 100 ergs per gram of material. The SI unit of dose is "gray" (Gy), where

1 Gy = 1 joule per kilogram, or 1 Gy = 100 rads

Dose equivalent

Dose equivalent may be regarded as an expression of dose in terms of its biological effect. Dose-equivalent takes account of the fact that, for a given absorbed dose such as 1 gray, a radiation of one type may give rise to a greater biological effect than a radiation of another type.

Dose equivalent = dose × quality factor (Q)

where Q depends on the radiation concerned. For most radiation used in medicine Q is 1.0 so that DE is numerically equal to dose. The old unit of DE is "rem", where 1 rad = Q rems. The SI unit of DE is "sievert" (Sv) where 1 Gy = Q sieverts, or 1 Sv = 100 rems.

Exposure

Exposure is a quantity that expresses the ability of radiation to ionize air and thereby create electric charges that can be collected and measured. The unit of exposure is "roentgen" (R), which is the quantity of X- or gamma rays which gives rise to 1 electrostatic unit of charge per cc of air at standard temperature and pressure (0°C and 760 mm Hg). The roentgen is now defined in terms of the

SI unit of charge, the coulomb (C) as follows:

$$1 \text{ R} = 2.58 \times 10^{-4} \text{ C/kg of air, or } 1 \text{ C/kg of air} = 3876 \text{ R}.$$

Activity

Activity is the transformation (disintegration) rate of a radioactive substance. Its unit is "Curie" (Ci) which corresponds to a transformation rate of 3.7×10^{10} disintegration per second. Therefore 1 microcurie (μCi) corresponds to 37,000 dis/sec. The SI unit of activity is "becquerel" (Bq), where 1 Bq = 1 disintegration per second.

CHAPTER III

MONTE CARLO SIMULATION AND EXPERIMENTAL SETUP

3.1   Introduction

The Monte Carlo N-particle (MCNP) computer code was used to simulate various cases regarding principles of the nuclear-based Explosive Detection System (EDS), in this thesis. Four different simulation geometries are used for the simulations. To compare the simulation results with those of experiment, an experiment was performed at China Institute of Atomic Energy (CIAE), Beijing, China. The following sections describe in details about the simulation geometries and cases and the experimental setup.

3.2   Monte Carlo simulation geometry

Four different geometries are used for simulations in this thesis. The following sections describe in details about these geometries.

3.2.1   Spherical geometry

Since the gamma rays emissions resulted from various activation processes is independent of the simulation geometry, the simple spherical geometry was used to simulate the gamma ray emissions. Figure 3.1 shows the spherical geometry which consists of a three- layers sphere. The inner layer of 2.5 cm radius (region

I) is used to hold the inspected material, while the middle layer (region II) of 5 cm is empty (contain air sample). The outer most layer of 1 cm thick is the spherical gamma ray detector. The neutron source that locates at the center of the sphere is a point source.
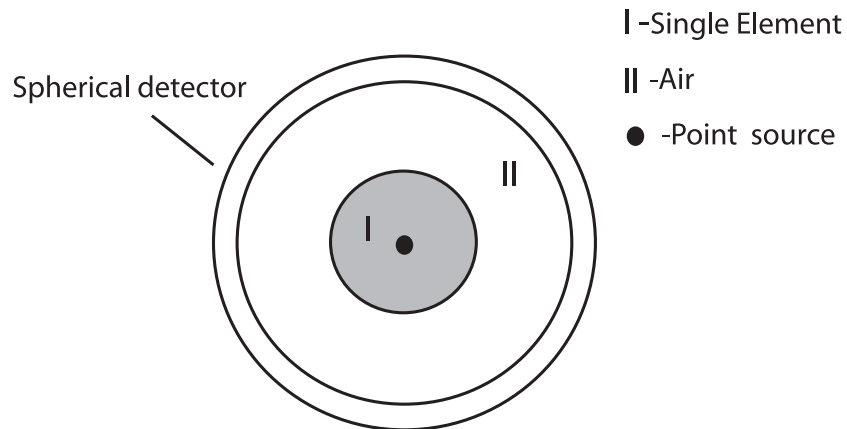
Figure 3.1 Spherical geometry for simulation of gamma ray emission.

3.2.2 Small geometry

The small geometry is used for simulation of the neutron flux distributed in the inspection cavity (Shtejer-Diaz et al., 2003). This simulation will provide the condition for the selection of the appropriate type and dimensions of the moderator. The moderator which produces the optimum thermal neutron flux in the inspection cavity will be selected. Figure 3.2 shows the shape and dimensions of this geometry. It has a rectangular shape consisting of an inspection cavity surrounded by slabs of moderating materials. A neutron source locates at the bottom of the cavity which has the dimensions of 20cm $\times$ 40cm $\times$ 30cm (W $\times$ L $\times$ H).
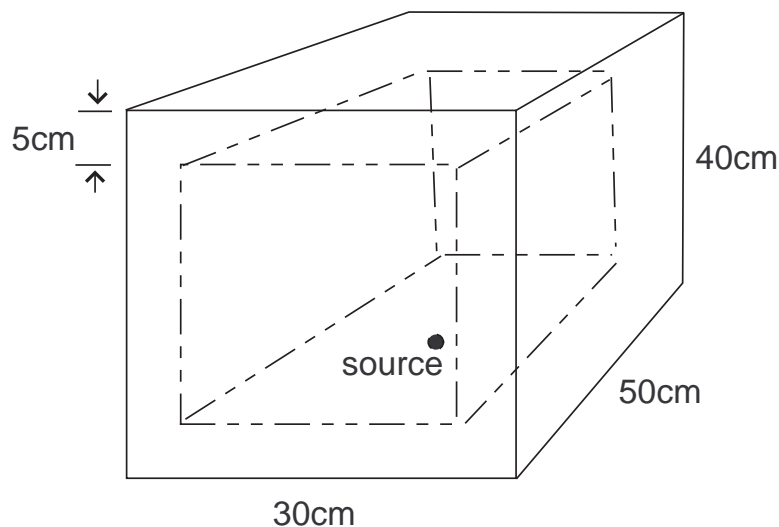
Figure 3.2 Small geometry of thermal neutron flux in the inspection cavity.

3.2.3 Large geometry

The EDS that is appropriate for checking briefcase or small parcel must be large enough to hold those objects. In this thesis, a large geometry is designed and used in the simulations for this application. This geometry is used for simulations of the thermal neutron flux distributed in the inspection cavity, the radiation doses distributed at the outer surfaces of the EDS and the number of the 10.8 MeV gamma rays created in the inspection cavity. The simulation of thermal neutron flux will provide conditions for the selections of the type and dimensions of the moderator including the thicknesses of neutron shielding and gamma ray shielding materials. Figure 3.3 shows the shape and dimensions of the large geometry. It has the shape of a rectangular box with the inspection cavity locates in the middle of the box as shown in Figure 3.3 (a). As shown in Figure 3.3 (b), the box's walls are made up of three layers of different materials with the moderator as the inner-most layer surrounding the inspection cavity. The second and third layers are
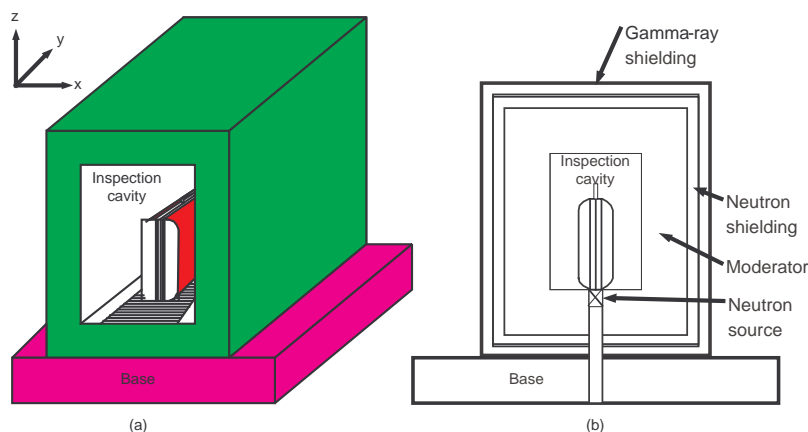
Figure 3.3 Large geometry for simulation of thermal neutron flux and radiation doses.

neutron and gamma- ray shielding materials, respectively. The inspected objects, such as luggage, can enter the inspection cavity on a conveyor belt that moves through the entrance and the exit of the cavity. There are two doors (not shown in Figure 3.3) with the same layers as of the EDS's walls closing the entrance and the exit of the inspection cavity. The entrance and exit doors will be opened and closed automatically when the luggage is outside and inside the inspection cavity, respectively. The dimensions of the inspection cavity in the X, Y and Z directions are 40 cm × 80 cm × 60 cm. The neutron source is at the bottom of the EDS just below the conveyor belt.

3.2.4   Experimental geometry

To compare simulation results with experiment, an experimental geometry is designed and used in this thesis. This geometry with the shape as shown in Figure 3.4 uses a paraffin as the moderating material with optimum thickness of 15 cm. The cavity size is $30 \times 40 \times 15$ cm^3 (W × L × H) and the source holder made from lead and installed at 18 cm under the cavity center.
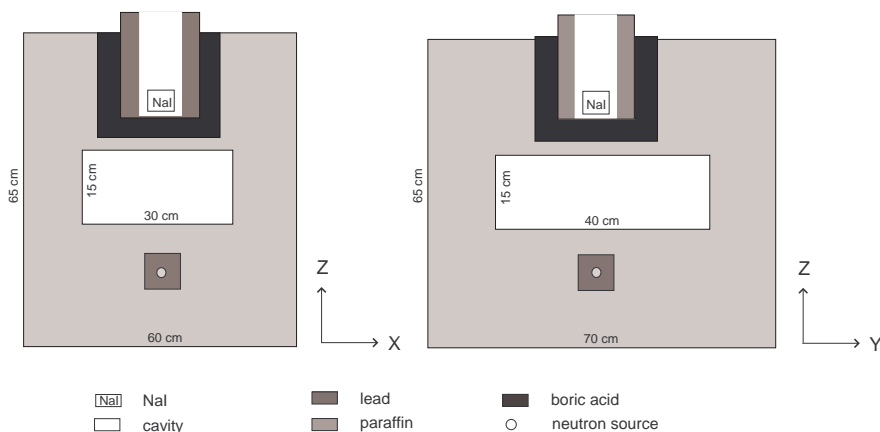
Figure 3.4 Two dimensional experimental geometry used in the experiment at CIAE, Beijing, China.
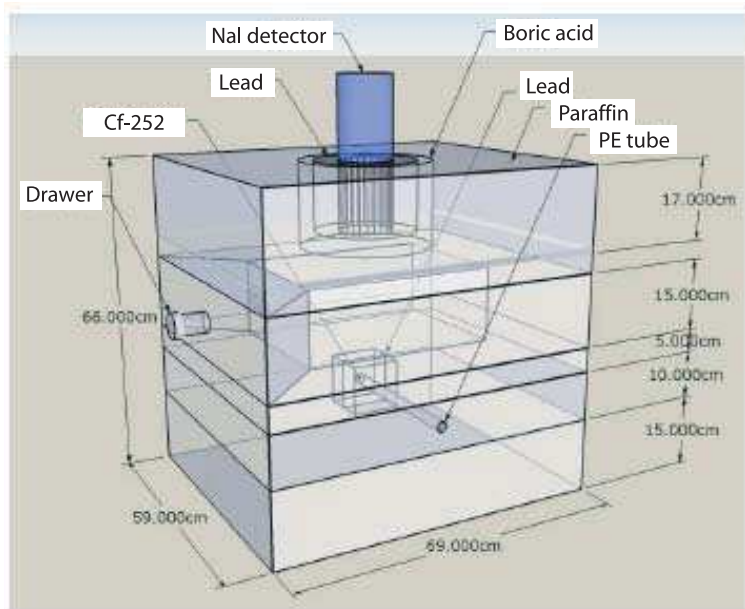
Figure 3.5 Three dimensional experimental geometry showing dimensions of the moderator and locations of the detector and neutron source (Courtesy from Yin Guanghua, Chinese army, Beijing, China).

The NaI(Tl) detector of 7.62 cm in height $\times$ 7.62 cm diameter is installed at the opposite side of the source. It was shielded in the front end and lateral sides with boric acid (3 cm thick) to absorb most neutrons which would have otherwise been absorbed by the NaI(Tl) crystal.It is further shielded with a layer of Pb (5

cm thick) on the side of the detector to stop gamma-ray from (n, γ) reactions coming from directions other than from the inspection cavity.

3.3   Simulation cases

Various cases of simulations were performed in this thesis. The following sections describe briefly about the description of each case.

3.3.1   Simulation of gamma ray emission resulted from activations of elements by thermal neutrons

This simulation was performed by using the spherical geometry. The elemental compositions of explosives (H, C, N, O) were put in region I, one at a time, for being activated by thermal neutrons of 0.025 eV energies. The number of gamma rays emitted from the activations are based on by F-4 tallies with energies covering from 0-12 MeV. The simulation results will be presented in chapter IV.

3.3.2   Simulation of gamma ray emission resulted from activations of elements by fast neutrons

This simulation was performed in the same way as in Section 3.3.1, except the source is changed to Cf-252 and Am-Be sources which emit fast neutrons. However, fast neutrons from the source will be slowing down and become thermal neutrons, after interacting with activated elements. Therefore, both elastic and inelastic nuclear reactions are expected to occur in this simulation. F-4 tallies represent the number of gamma rays emitted. The simulation results will be presented in chapter IV.

3.3.3 Simulation of gamma ray emission resulted from activations of materials by fast neutrons

This simulation was performed in the experimental geometry. Eight materials are used in this simulation. They are air, water, TNT, RDX, rubber , melamine, silk and sugar. The neutron sources used are Cf-252 and Am/Be. F-4 tallies are used in the simulation to represent the type and number of gamma rays produced in the simulation. The simulation result will be presented in chapter IV.

3.3.4 Simulation of pulse height spectra resulted from activations of materials by fast neutrons

This simulation was performed in the experimental geometry in the same way as in Section 3.3.3 (Sood et al., 2004). The same materials as those of Section 3.3.3 are used in this simulation. The neutron sources are Cf-252 and Am/Be. F-8 tallies (pulse height) are used in this simulation to represent the type and number of gamma rays produced in the simulation. The simulation results will be presented in chapter IV.

3.3.5 Simulation of thermal neutron flux distribution in the inspection cavity

This simulation was performed with three geometries, namely, the small, the large and the experimental geometries. Various moderators such as heavy water, light water, graphite, paraffin, polyethylene are used as the inspected materials. The neutron sources used are Cf-252 and Am/Be. F-4 tallies are used to represent the thermal neutron flux created.The simulation results from the small geometry, will be used as the condition for the selection of the appropriate type

and dimensions of the small EDS's moderator. The simulation results from the large geometry, will be used as the condition for the selection of the appropriate type and dimensions of the large EDS's moderator. The simulation results from the experimental geometry, will be used for comparisons with the experimental results.

3.3.6 Simulation of radiation doses created at the outer surfaces of the EDS

This simulation was performed in the large and the experimental geometries. Both of Cf-252 and Am/Be are used as neutron sources. The gamma ray and neutron doses created at the outer surfaces of the EDS are simulated. The total dose at the outer surfaces of the EDS can be obtained by adding these two doses. The total dose from the large geometry will be used to estimate the maximum dose created at its outer surfaces and compare with the ICRP maximum permissible dose (ICRP 75, 1997). The total doses from the experimental geometry will be used to compare with the experimental results.

3.3.7 Simulation of gamma ray attenuation

As mentioned in chapter I, gamma ray attenuation and backscatter can be additional indicators for identifying explosive. They will serve to reduce the EDS's false alarm rate. For this purpose, the gamma ray attenuation and backscatter simulations were performed in this thesis by using gamma rays from Cf-source. They are simulated by using the experimental geometry with two gamma ray detectors. The transmission detector locates at the top of the geometry while the backscattering detector locates inside the inspection cavity, next to the neutron source. Various materials are used in the simulation. From the simulation results,

the parameters of $ln(I/I_0)$ are deduced. These results will be presented in chapter IV.

3.3.8 Simulation of the 10.8 Mev gamma ray flux resulted from activations of TNT and RDX by fast neutrons

This simulation was performed by using the large geometry. The purpose of this simulation is to use its results for the estimation of the required source strength necessary for obtaining a desired detection sensitivity of the EDS. TNT and RDX are used in the simulation along with the Cf- and Am/Be-neutron sources. Fluxes of the 10.8 MeV gamma rays at the center of the inspection cavity resulted from activations of TNT and RDX by neutron sources are obtained from the simulation. These results will be presented in chapter IV.

3.4 Experimental Setup

To compare the simulation results with those from experiment, an experiment was performed at China Institute of Atomic Energy (CIAE), Beijing, China. The experimental setup is as shown in Figures 3.4 and 3.5 with the data acquisition system as shown in Figure 3.6. The data acquisition system inside the control room is connected to the experimental geometry outside the control room. The following sections describe the details of components of the experimental setup.

3.4.1 Neutron source

Cf-252 and Am/Be with source strengths of 2.125×10^7 and 2×10^5 n/s are used in the experiment. They are put in the source holder which locates at

the bottom portion of the experimental geometry as described in Section 3.2.4. The Cf-source produces neutrons with the most probable and average energies of 0.7 and 2.3 MeV, respectively. However, it also produce neutrons of higher energies with the highest energy of about 7 MeV (Ensslin, 1997). The Am/Be-source produces neutrons with an average energy of 4 MeV and the highest energy of 11 MeV (Kiefer and Maushart, 1972).

3.4.2 Moderating material

Due to the economic and practical resons, paraffin of 15 cm thick is selected as the EDS's moderator. The results from MCNP simulations confirmed that this thickness is the optimum thickness.

3.4.3 Radiation detectors

NaI (Tl) of 7.62 cm diameter and 7.62 cm in height is used for measuring gamma rays in the experiment. It is located at the top of the experimental geometry as shown in Figure 3.5. It is shielded by boric acid and lead as described in Section 3.2.4. The ^{3}He detector of 2.5 cm diameter and 9.7 cm long is used to measure the thermal neutron flux at the center of the inspection cavity. The radiation dosimeter is used to measure radiation at various positions outside the experimental EDS.

3.4.4 Data Acquisition System

Figure 3.6 shows a schematic diagram of the data acquisition system connected to the NaI(Tl) detector. It comprises of an amplifier, a multichannel analyzer (MCA) and computer. The amplifier is the AFT Research Amplifier - Model

2025 from Canberra Inc. Its gain can be adjusted to cover the whole energy spectrum of 2.23 MeV (of hydrogen) to 10.8 MeV (of nitrogen). The MCA is the compact and fast module from Amptex Inc. The computer is a personal computer with a Pentium IV processor. It is very easy to use with user friendly command.
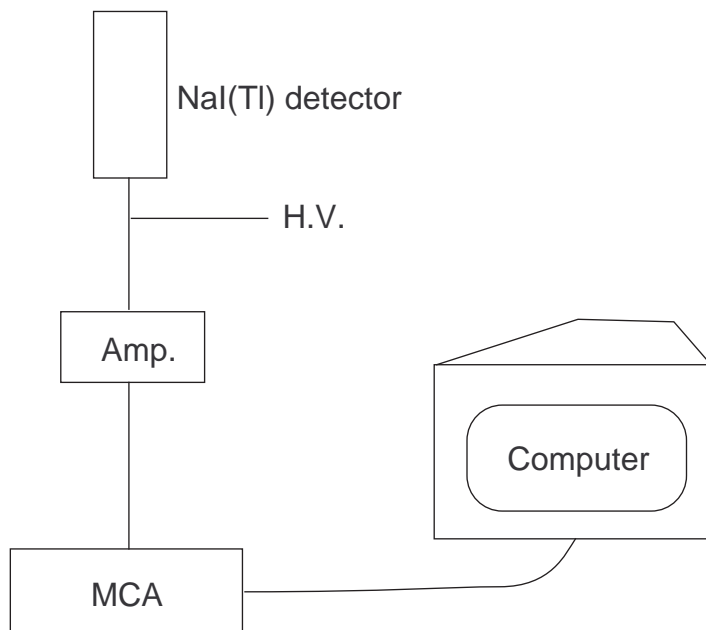
Figure 3.6 The circuit diagram for the data acquisition system connected to the NaI(Tl) detector.

CHAPTER IV

RESULTS AND DISCUSSIONS

In this chapter, the results from MCNP simulations and experiment are presented and discussed.

4.1 MCNP Simulation results

Various simulations were performed by using MCNP computer code. The results from these simulations are summarized in the following sections.

4.1.1 Gamma ray emission resulted from activations of elements by thermal neutrons

The gamma ray emission resulted from activations of H, C, O and N by thermal neutrons are presented in this chapter. These results are based on using the spherical geometry with elements located in region II. Figures 4.1–4.4 show the F-4 tallies of gamma ray emission resulted from the (n, γ) reactions when H, C, O and N are activated by thermal neutrons, respectively. Only the 2.2 MeV gamma ray line is emitted with the cross section of 0.332 b when H is activated by thermal neutrons. There are three lines emitted, namely the 1.26, 3.69 and 4.95 MeV with cross sections of 0.00124, 0.00122 and 0.00261 barns, respectively when C is activated by thermal neutron. The 1.26- and 3.69- MeV lines are the cascades of the 4.95 MeV line.

The 0.511- MeV line is the result of gamma ray annihilation process. There
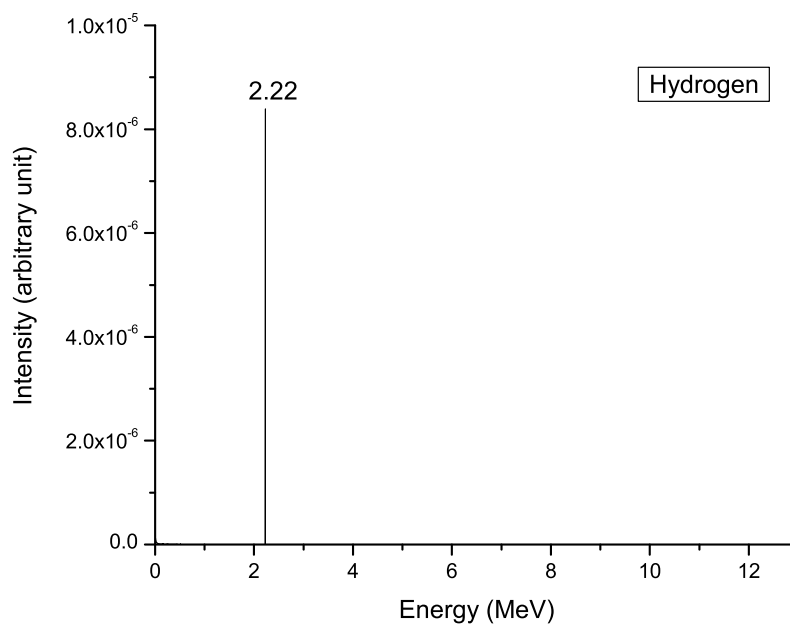
Figure 4.1 F4 tally of a gamma ray emitted when hydrogen is activated by thermal neutron.

are four significant lines of 0.87, 1.09, 2.19 and 3.27 MeV emitted when O is activated. Their cross sections are 1.77×10^{-4}, 1.58×10^{-4}, 1.64×10^{-4} and 3.53×10^{-5} b, respectively. When N is activated by thermal neutron, there are so many gamma ray lines emitted in the low energy region with only one line at the high energy region. These low energy lines will not be observed experimentally because they are buried under the Compton continuum. Though the 10.8 MeV-line at high energy region has a low cross section of 0.011 b, it is the important indicator for identification of explosive by TNA technique because it is well separated from other lines.

Figure 4.2 F4 tally of gamma rays emitted when carbon is activated by thermal neutron.

Figure 4.3 F4 tally of gamma rays emitted when oxygen is activated by thermal neutron.

Figure 4.4 F4 tally of gamma rays emitted when nitrogen is activated by thermal neutron.

4.1.2 Gamma ray emission resulted from activations of elements by Cf-neutrons

The emissions of gamma rays resulted from activations of H, C, O and N by neutrons from Cf-252 is simulated in this thesis with the results shown in Figures 4.5–4.8, respectively. Since the source produces fast neutrons that eventually become thermalized while interacting with moderator nuclei, the same kind of gamma ray emissions, as in Section 4.1.1, are expected. Additionally, gamma rays due to the inelastic nuclear (n, n′γ) reaction are expected to occur in most of these elements except in H. The 4.43 MeV line with a cross section of 0.2-0.4 b is emitted in C as the result of (n, n′γ) reaction.

In the case of O, the 6.13 MeV line is emitted with a cross section of 0.1

Figure 4.5 F4 tally of a gamma ray emitted when hydrogen is activated by Cf-252 source.

Figure 4.6 F4 tally of gamma rays emitted when carbon is activated by Cf-252 source.

Figure 4.7 F4 tally of gamma rays emitted when oxygen is activated by Cf-252 source.
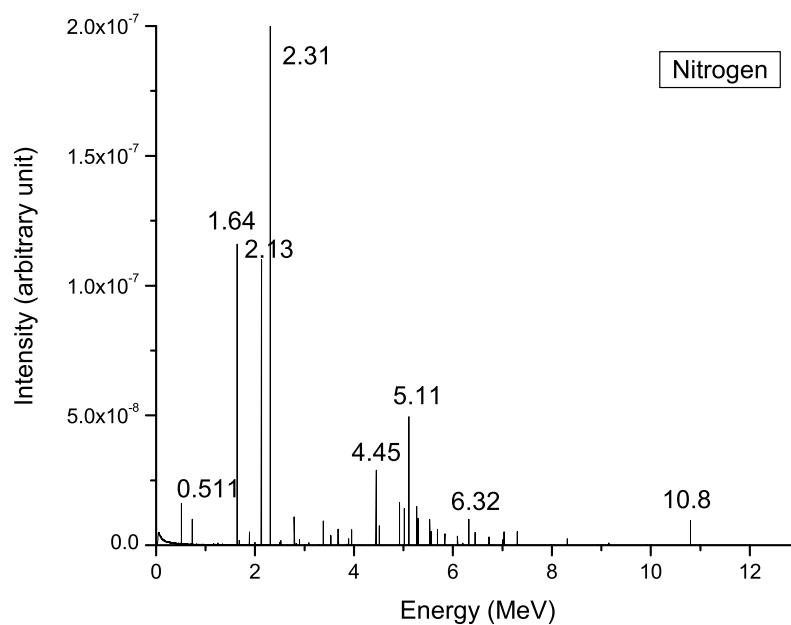
Figure 4.8 F4 tally of gamma rays emitted when nitrogen is activated by Cf-252 source.

- 0.4 b. For N, three gamma ray lines are emitted. They are 1.64, 2.31 and 5.11 MeV with cross sections of 0.02-0.1 b. The emissions of these gamma ray lines agree with theoretical results of Table 4.1 (Vourvopoulos et al., 1993).

4.1.3 Gamma ray emission resulted from activations of elements by Am/Be-neutrons

The emissions of gamma rays resulted from activations of H, C, O and N by Am-Be source are also simulated in this thesis with the results shown in Figures 4.9–4.12. As appeared in these figures, the gamma rays emitted by using Am-Be source are similar to those emitted by using Cf source. This is because Am-Be source produces neutrons with an average energy of about 4 MeV which is energetically possible to produce both the elastic and inelastic nuclear reactions. Additionally, the simulations of gamma ray emissions resulted from activations of C, O and N by Am/Be-source with energy cut off are performed in this thesis. In these simulations, when neutrons from source have energies below 4 MeV, the simulations are cut off. Therefore, the thermal or nuclear capture reaction should not occur in this simulation. Figures 4.13–4.15 show the results from these simulations. For the case of C, only the 4.43- MeV line due to the fast reaction is emitted. In the case of O, only the 6.13 MeV line is emitted. For the case of N, the 10.8 MeV line disappeared while the 1.64, 2.31 and 5.11 MeV lines persisted. The gamma ray lines of 4.43 MeV from C (n, n$'\gamma$) reaction, 6.13 MeV from O (n, n$'\gamma$) reaction and 0.72, 1.63, 2.12 and 2.31 MeV from N also occur when using neutron 7.6 MeV from D-D accelerator (Sawa, 1993).
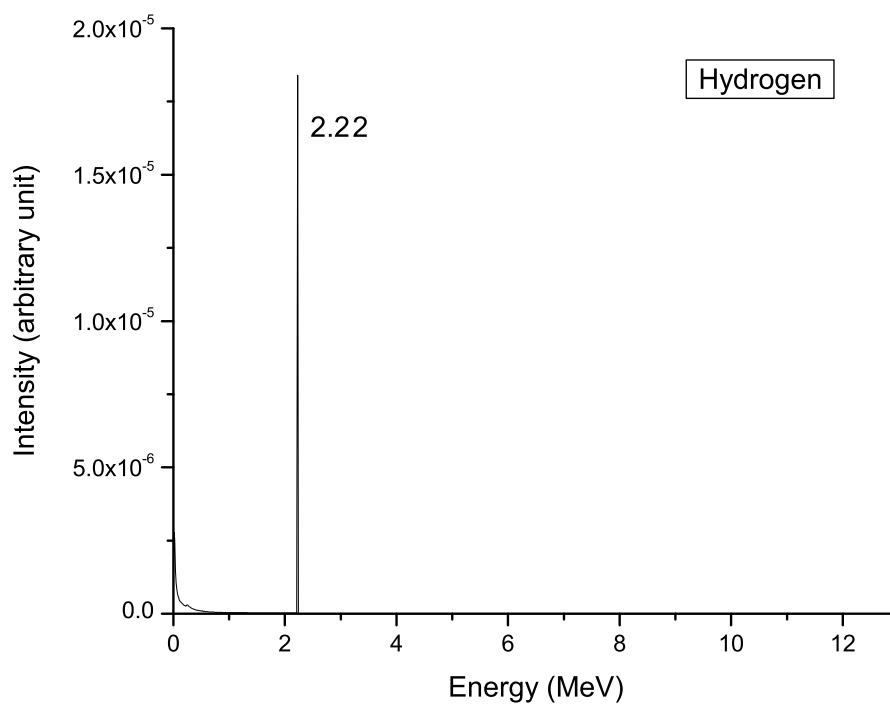
Figure 4.9 F4 tally of a gamma ray emitted when hydrogen is activated by Am/Be source.
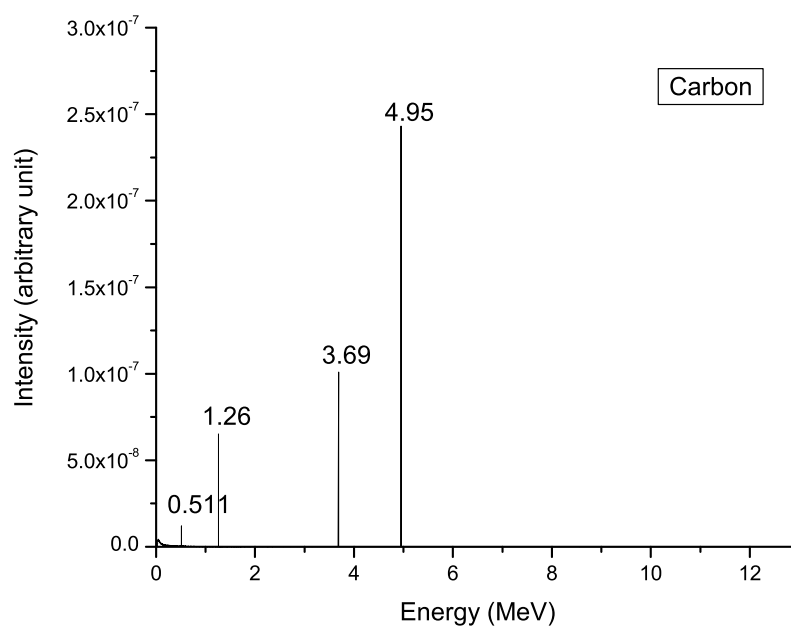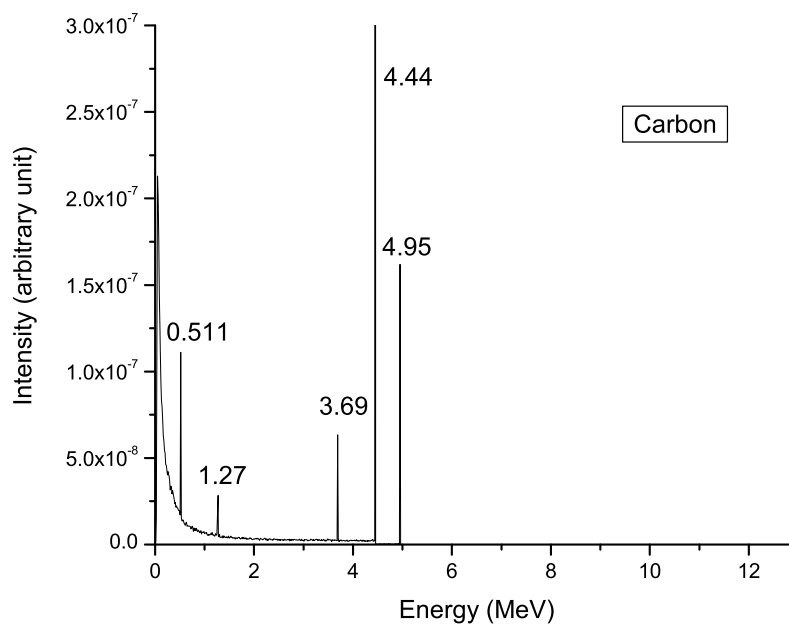

Figure 4.10 F4 tally of gamma rays emitted when carbon is activated by Am/Be source.
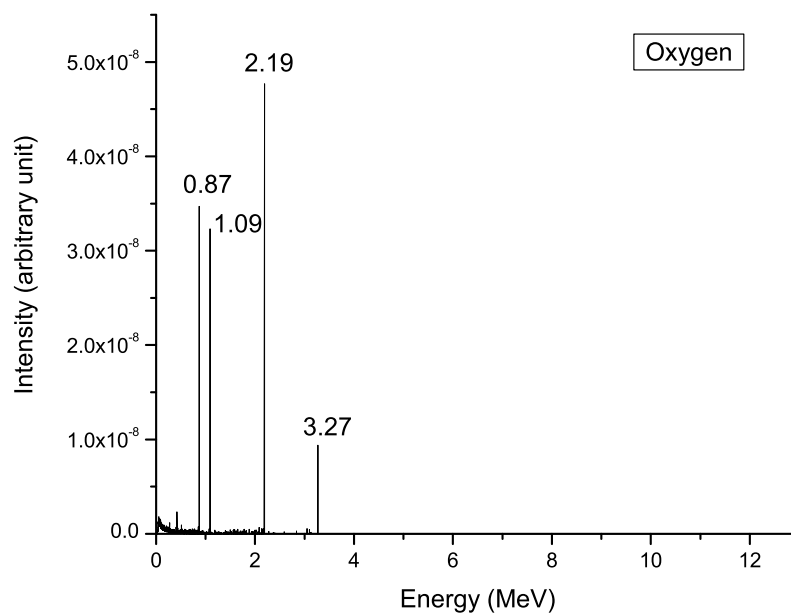
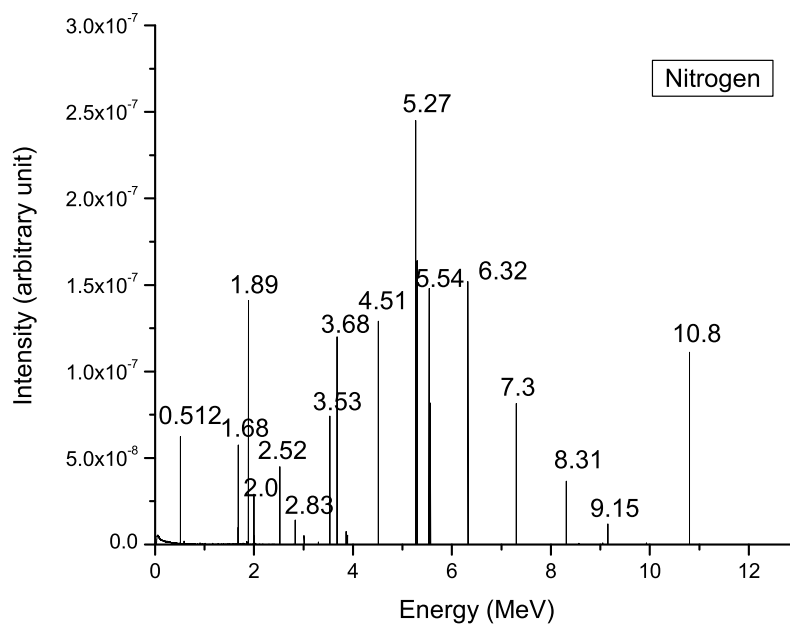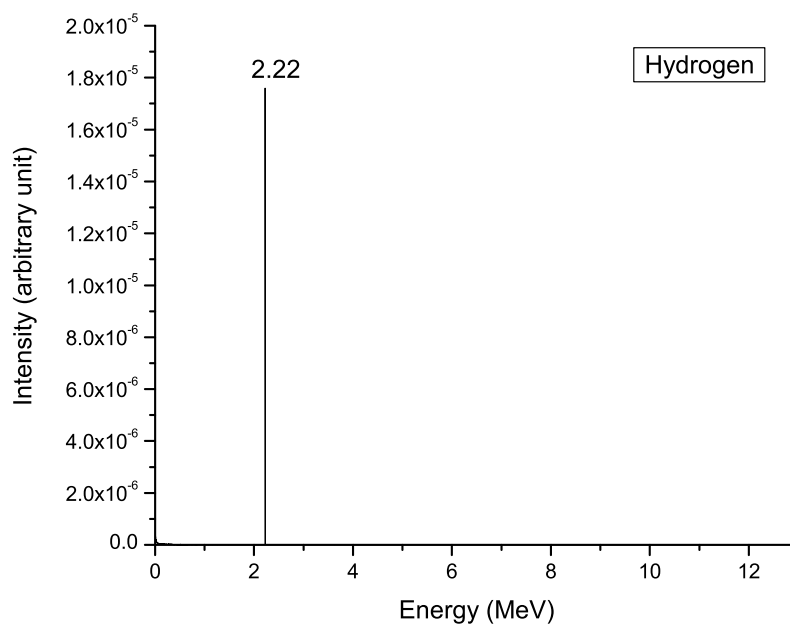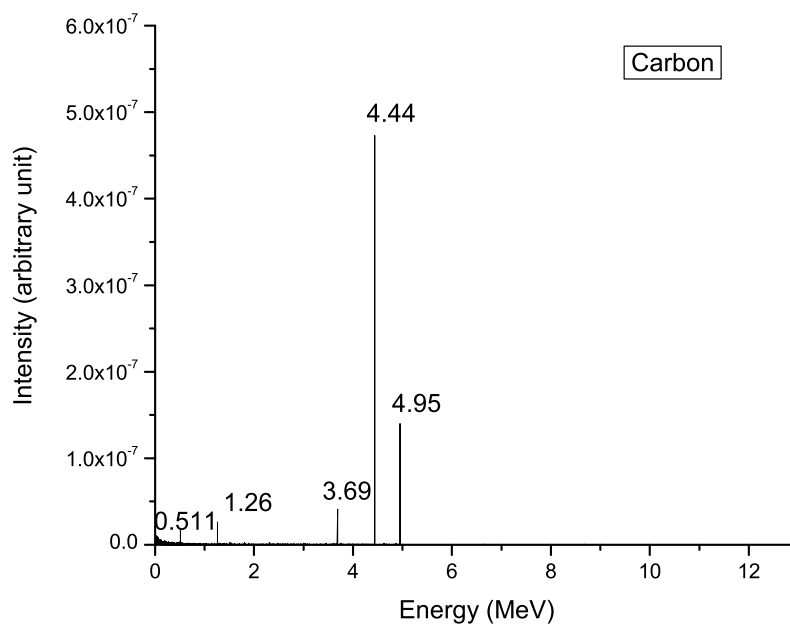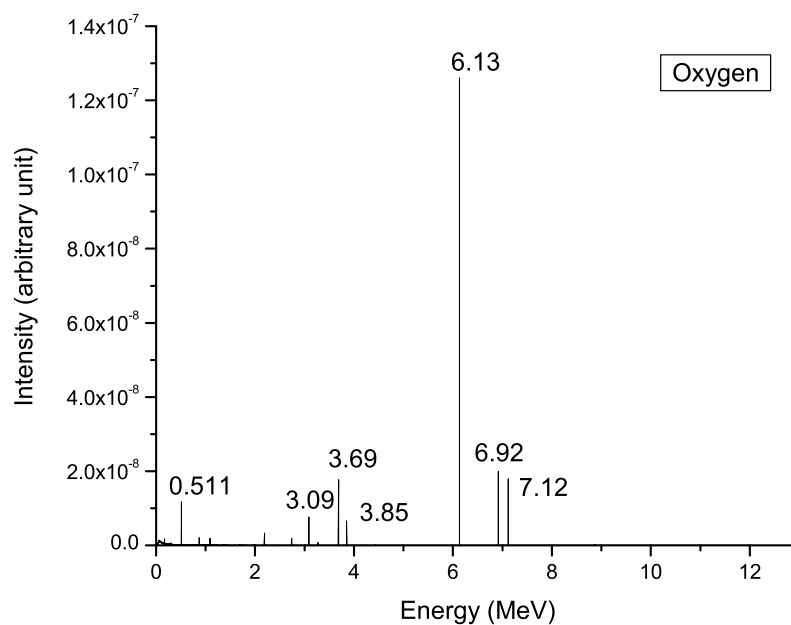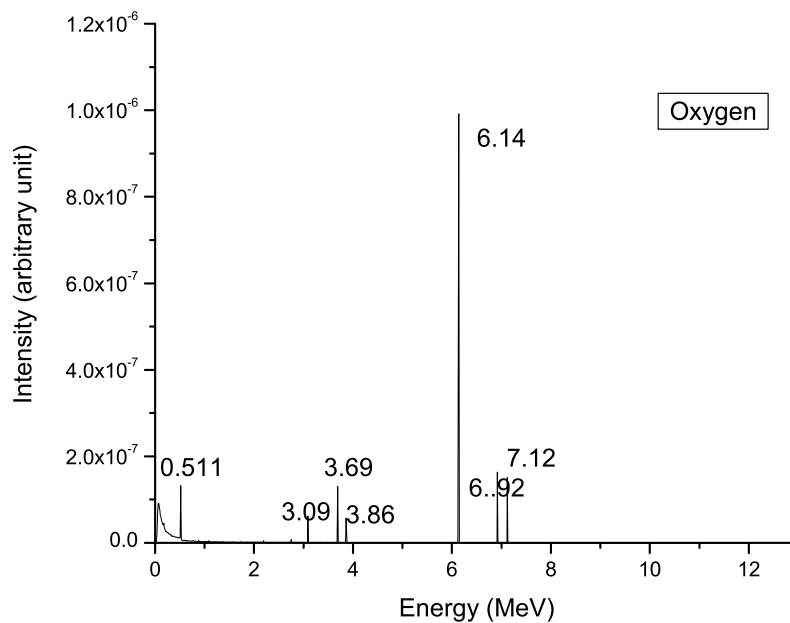**Figure 4.11** F4 tally of gamma rays emitted when oxygen is activated by Am/Be source.
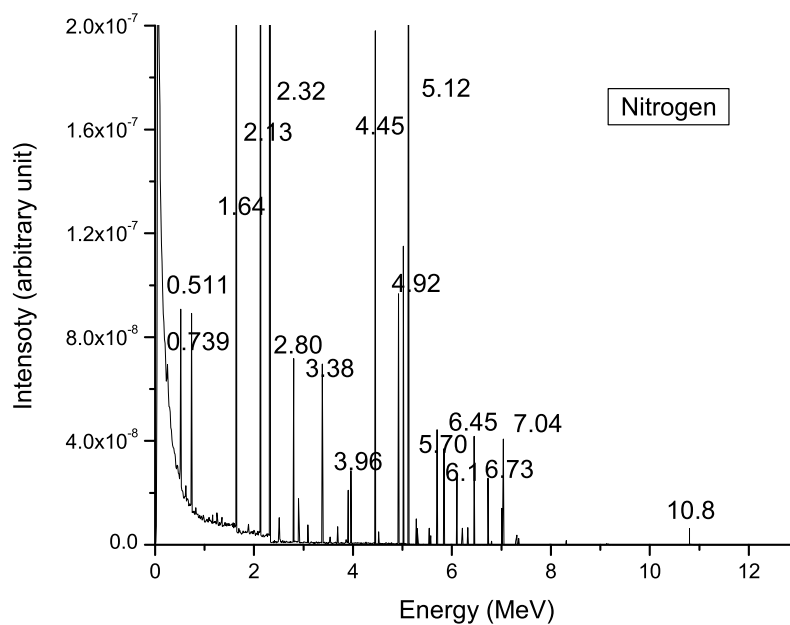
Figure 4.12 F4 tally of gamma rays emitted when nitrogen is activated by Am/Be source.
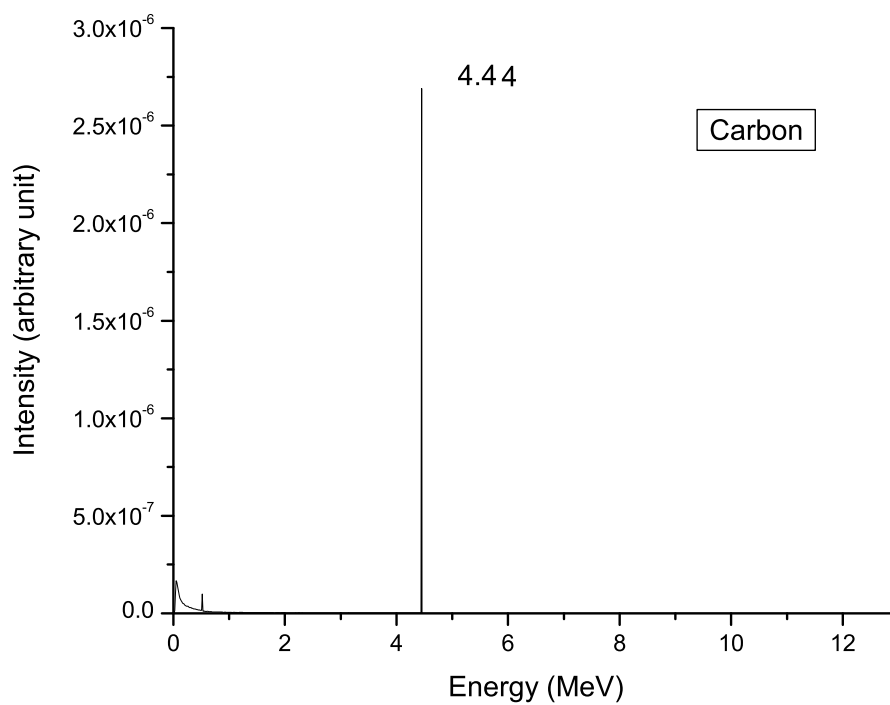
Figure 4.13 F4 tally of gamma rays emitted when carbon is activated by Am/Be source with energy cutoff.
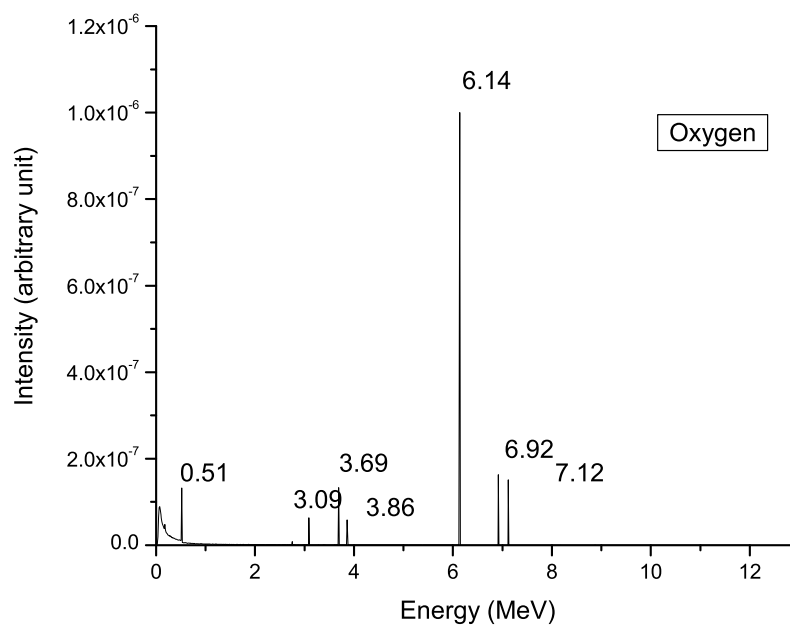
Figure 4.14 F4 tally of gamma rays emitted when oxygen is activated by Am/Be source with energy cutoff.
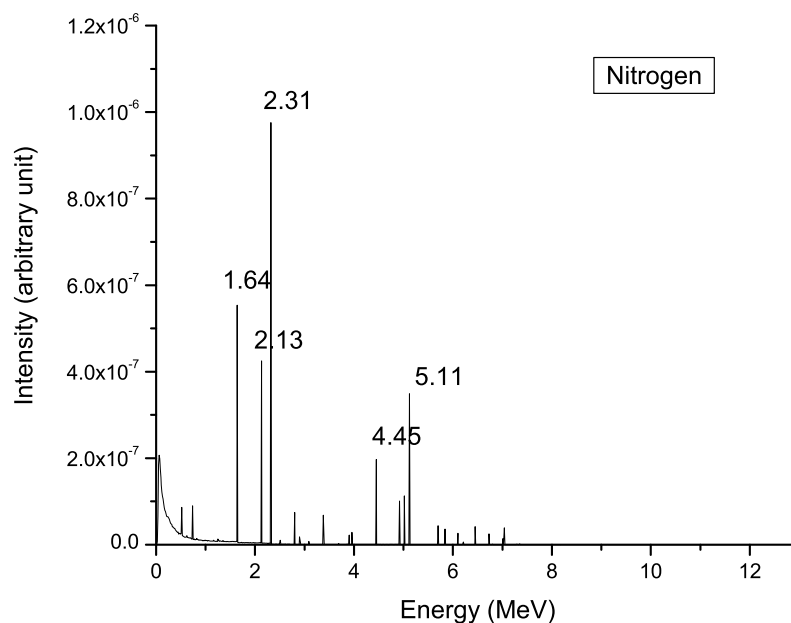
Figure 4.15 F4 tally of gamma rays emitted when nitrogen is activated by Am/Be source with energy cutoff.

Table 4.1 Neutron (fast and thermal) induced nuclear reactions on H, C, N and O (Vourvopoulos et al., 1993).

Element	Reaction	E_n^{min} (MeV)	Cross Section (barn)	E_γ (MeV)
H	n, γ	-	0.3326	2.23
C	n, n$'\gamma$	4.8	200*	4.44
N	n, n$'\gamma$	4.7	70*	2.31
N	n, γ	-	75	10.83
O	n, n$'\gamma$	6.4	96*	6.13
O	n, p	10.3	38*	6.13*

* Measured at $E_n = 14$ MeV

4.1.4   Gamma ray emission resulted from activations of materials by Cf-neutrons

The simulation results of gamma ray emission resulted from activations of six materials by Cf-neutrons are shown in Figures 4.16–4.21. These materials are shown in Table 4.2 along with their elemental compositions. When activated TNT by Cf-neutrons, most of the gamma ray lines due to both the thermal and fast reactions in its' elemental compositions (H, C, O and N) are observed.

All the important lines (the 2.2, 4.43, 6.13 and 10.8 MeV lines from H, C, O and N, respectively) which are important for the explosive identification are observed. However, the 6.13 MeV line from O has a very low intensity. Most of these gamma ray lines are expected to be observed in the experiment. The rest are expected to be covered by Compton continuum of the experimental spectrum. Figure 4.21 shows the RDX spectrum which basically contains similar gamma rays lines as of TNT except the 6.13 MeV weak line from O is missing. This is because both materials are explosives with the same elemental compositions (H, C, O, N) but with different number of atoms. Spectra of the remaining materials do not contain all these four prominent gamma ray lines concurrently as shown in Figures 4.16–4.21. This is because they either contain different elemental compositions or different number of atoms of the elemental compositions.

Figure 4.16 F4 tally of gamma ray emission resulted from activations of Silk by Cf-252 source.
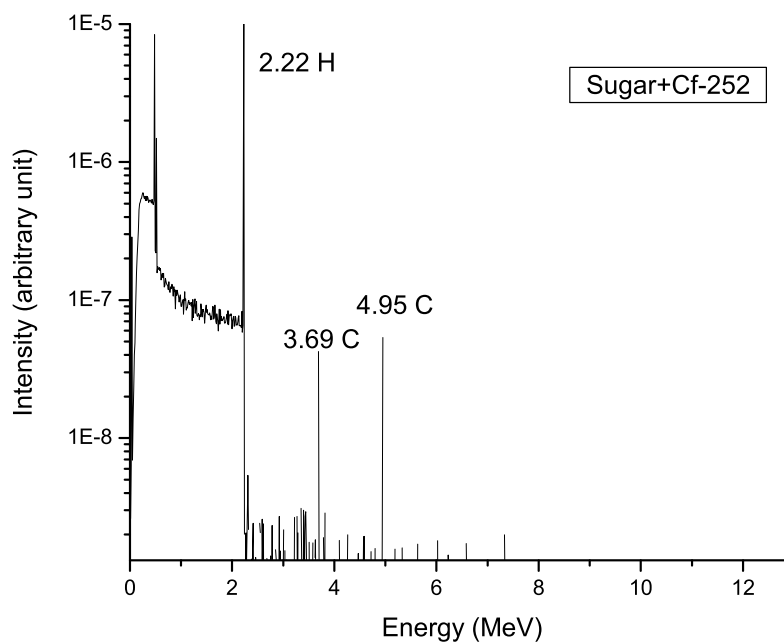
Figure 4.17 F4 tally of gamma ray emission resulted from activations of Sugar by Cf-252 source.
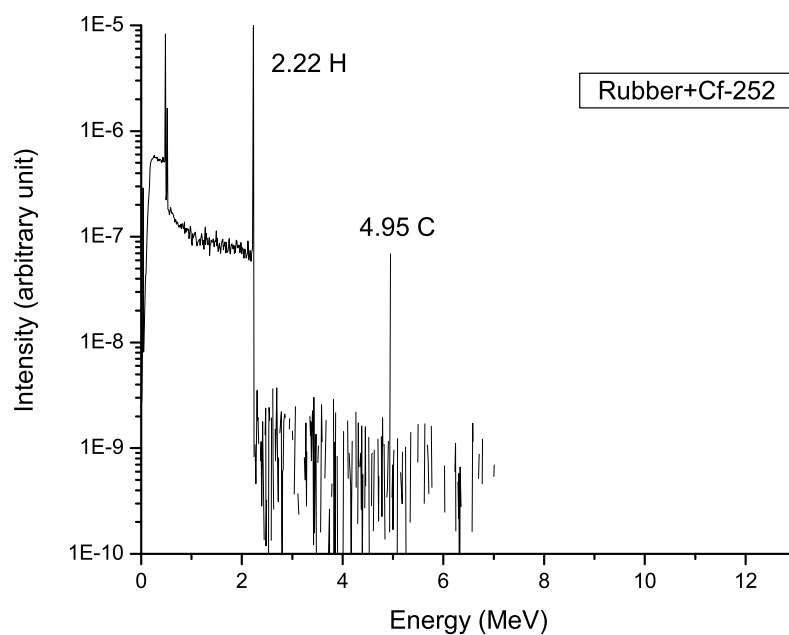
Figure 4.18 F4 tally of gamma ray emission resulted from activations of Rubber by Cf-252 source.
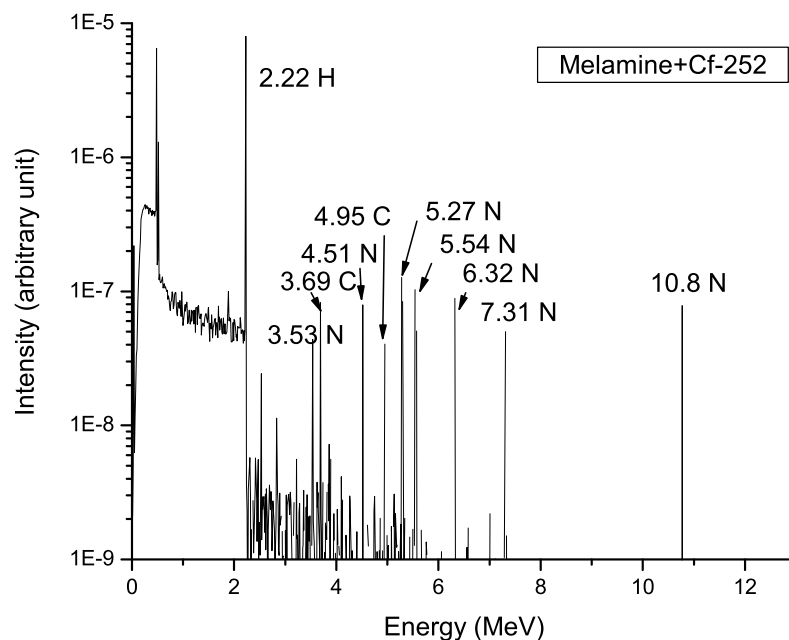
Figure 4.19 F4 tally of gamma ray emission resulted from activations of Melamine by Cf-252 source.
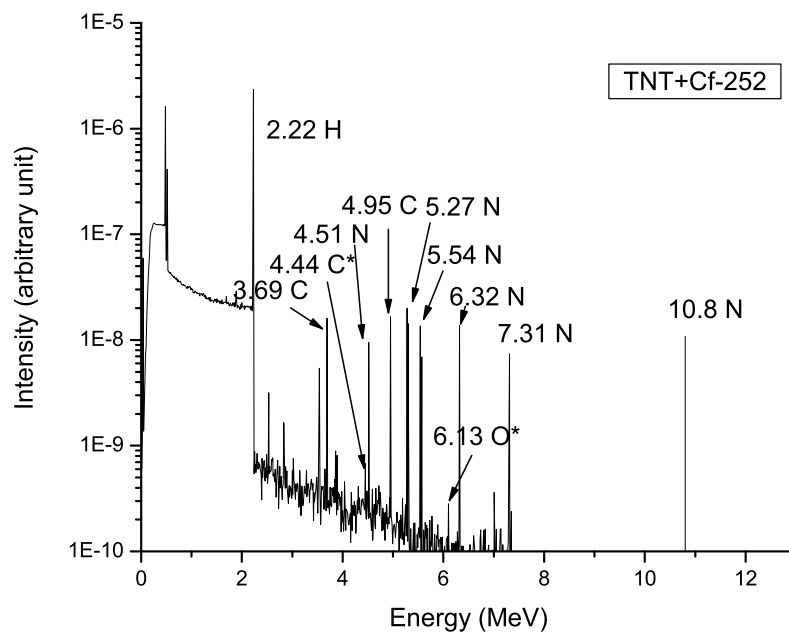
Figure 4.20 F4 tally of gamma ray emission resulted from activations of TNT by Cf-252 source.
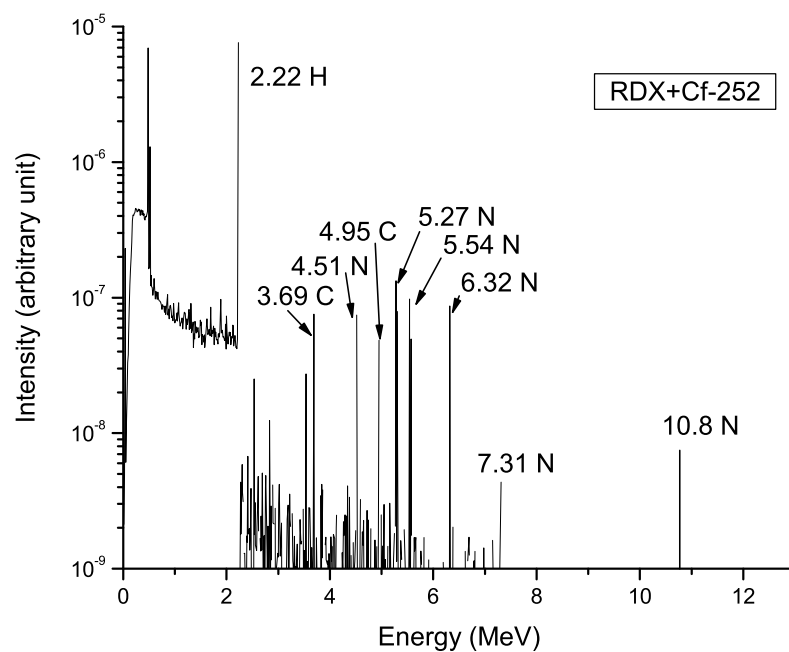
Figure 4.21 F4 tally of gamma ray emission resulted from activations of RDX by Cf-252 source.

Table 4.2 Elemental compositions and density of explosive and common materials.

Substance of interest	Elementary composition	Physical density (g/cm^3)
Cocaine	$C_{17}H_{21}NO_4$	1.40
Polyethylene	CH_2	0.94
Rubber	C_5H_8	0.94
Silk	$C_3H_{11}O_6N_3$	0.30
Sugar	$C_{11}H_{22}O_{11}$	0.9
Melamine	$C_3H_6N_6$	1.57
TNT	$C_7H_5O_6N_3$	1.65
RDX	$C_3H_6O_6N_6$	1.82

4.1.5 Gamma ray emission resulted from activations of materials by Am/Be-neutrons

The same simulations as in Section 4.1.4 but with Am/Be as the neutron source were performed with the resulted spectra shown in Figures 4.22–4.27. Similar characteristic are observed in these spectra when compare to those of Section 4.1.4. All four prominent lines (2.2, 4.43, 6.13 and 10.8 MeV) are observed in the spectra of TNT and RDX as shown in Figures 4.26 and 4.27. The 6.13 MeV liens are clearly observed in both spectra with higher intensities when compare to those of Figures 4.20 and 4.21. This is because Am/Be produces neutrons with energies higher than those of Cf. Therefore the probability of fast reaction is higher than that of Cf, resulting in the higher intensities of the 6.13 MeV lines.
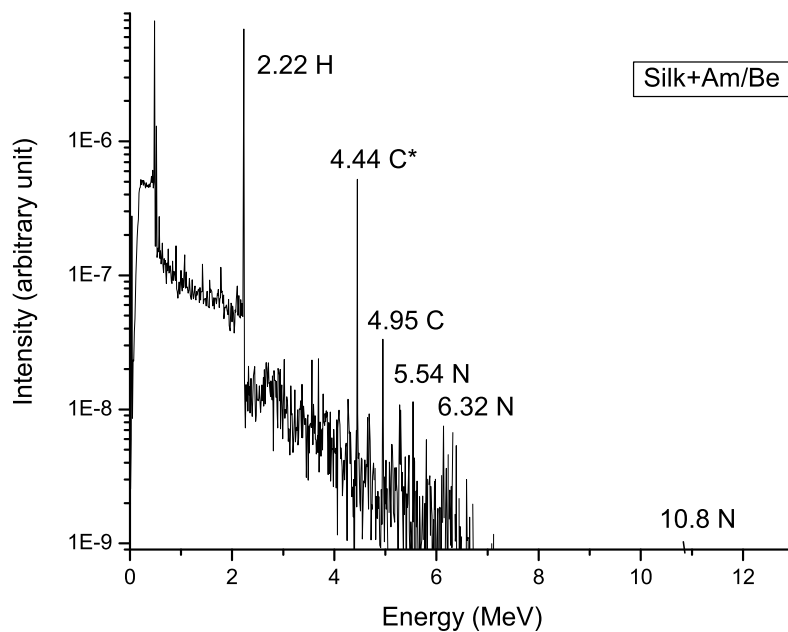
Figure 4.22 F4 tally of gamma ray emission resulted from activations of Silk by Am/Be source.
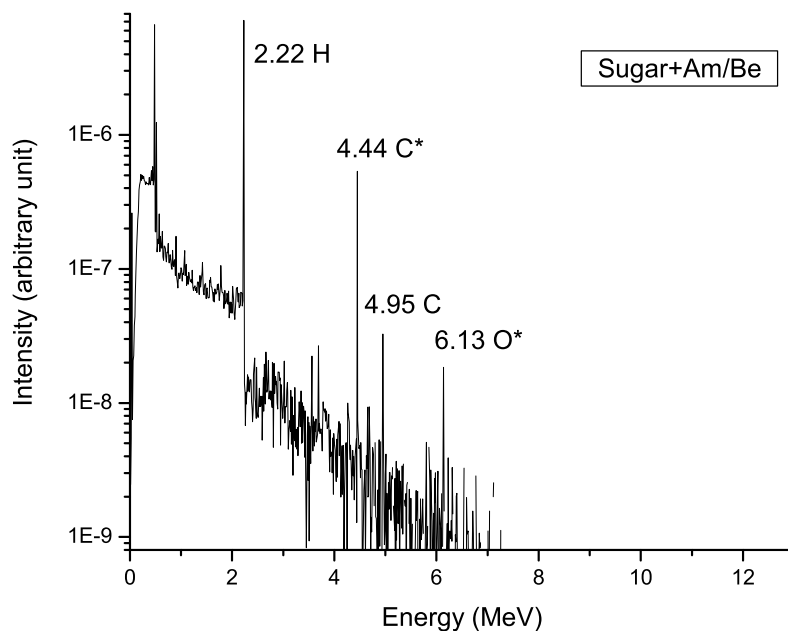
Figure 4.23 F4 tally gamma ray emission resulted from Monte Carlo Simulation of Sugar by using Am/Be neutron source.
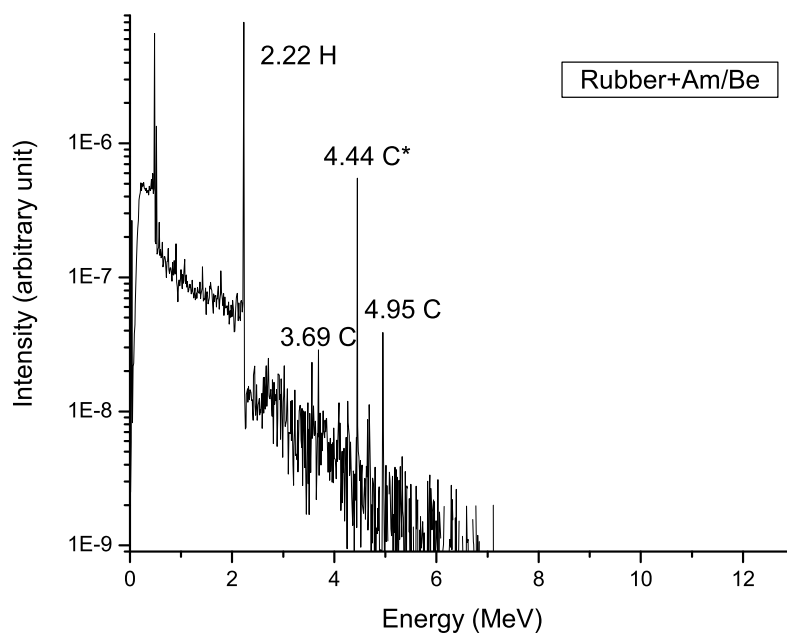
Figure 4.24 F4 tally gamma ray emission resulted from activation of Rubber by Am/Be source.
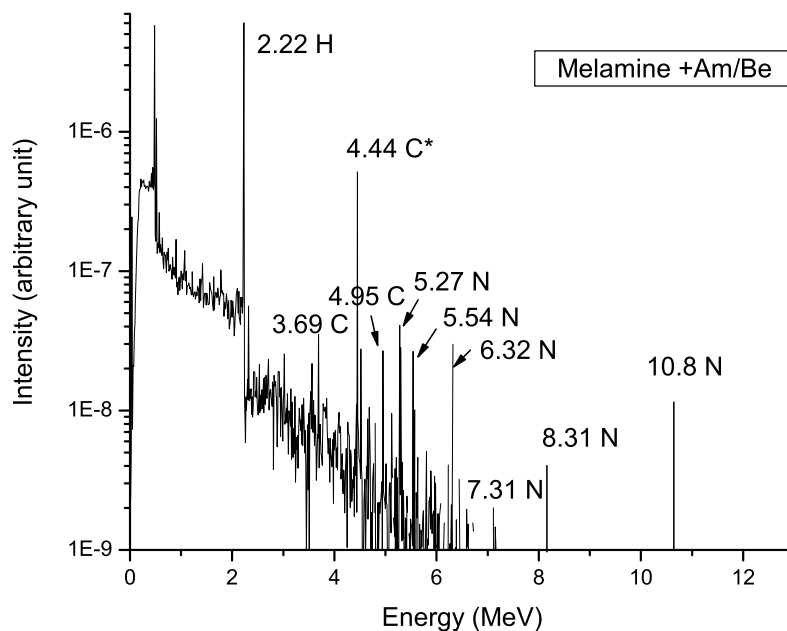
Figure 4.25 F4 tally gamma ray emission resulted from activation of Melamine by Am/Be source.

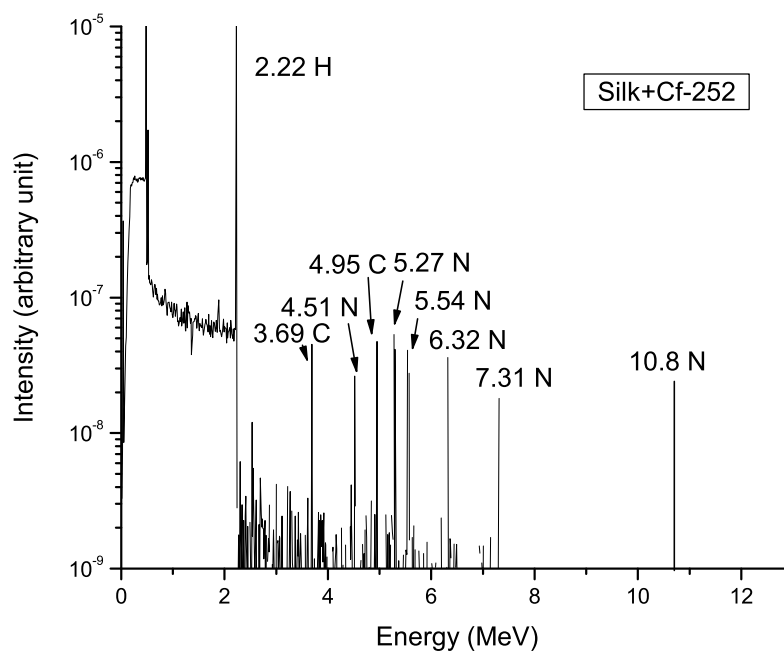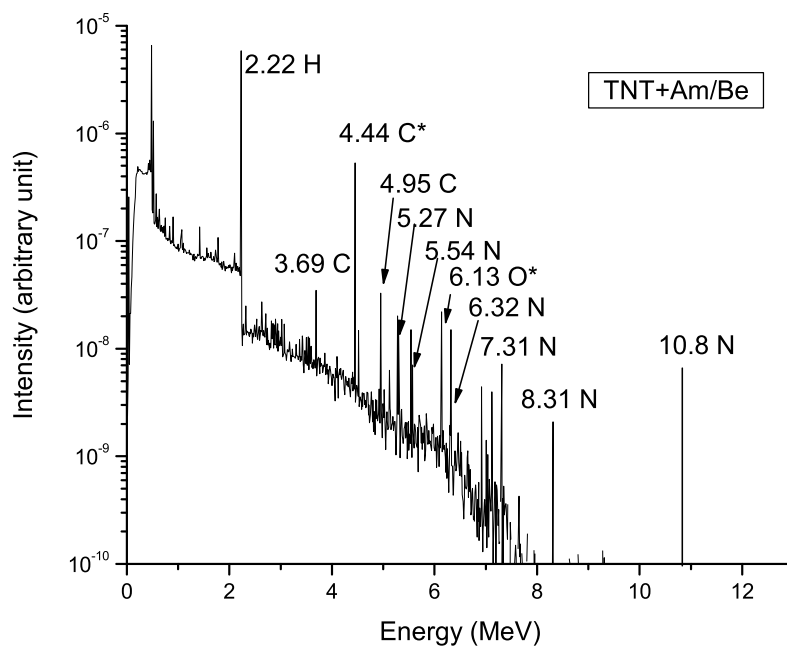**Figure 4.26** F4 tally gamma ray emission resulted from activation of TNT by Am/Be source.
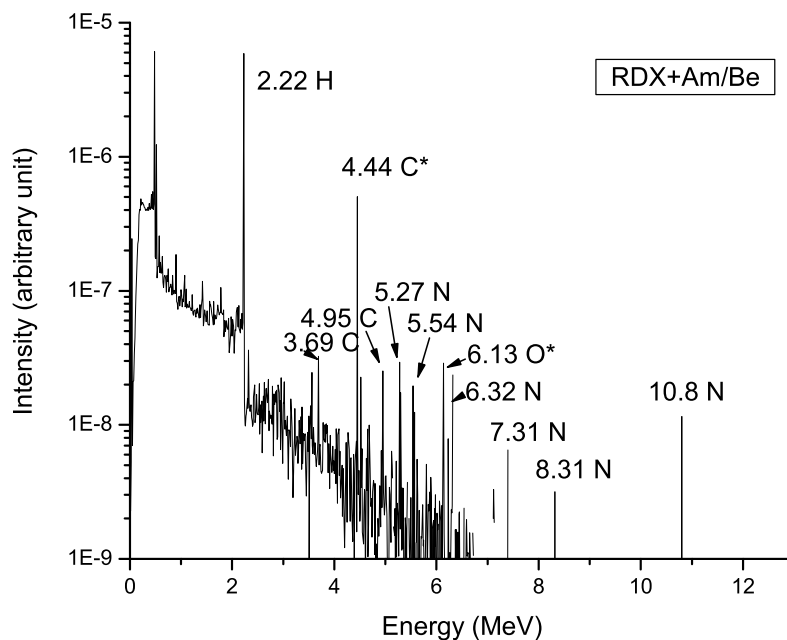
Figure 4.27 F4 tally gamma ray emission resulted from activation of RDX by Am/Be source.

The same characteristics are also observed in the spectra of the remaining materials as those of Section 4.1.4. The gamma ray lines appear on these spectra correlate with the material elemental compositions.

4.1.6   Pulse Height Spectra resulted from activations of materials by Cf-neutrons

The generations of pulse height spectra resulted from activations of various explosives and common materials were simulated in this thesis. The simulations are based on the experimental geometry and F-8 tallies with materials located in its inspection cavity. Figures 4.16–4.23 show the spectra of air, water, silk, sugar, rubber, melamine, TNT and RDX, respectively. For the first five materials, which either do not contain N or contain small number of N atoms, the spectra do not contain the 10.8 MeV gamma ray line. For the last three materials (melamine, TNT and RDX) which have high concentration of N, their spectra contain the 10.8 MeV gamma ray lines as expected.

Except for the case of melamine, these results clearly show that the 10.8 MeV line can be a good indicator for identifying the existence of explosive in the inspected materials. In case of melamine, we need an additional indicator to identify the existence of explosive with low false alarm rate.
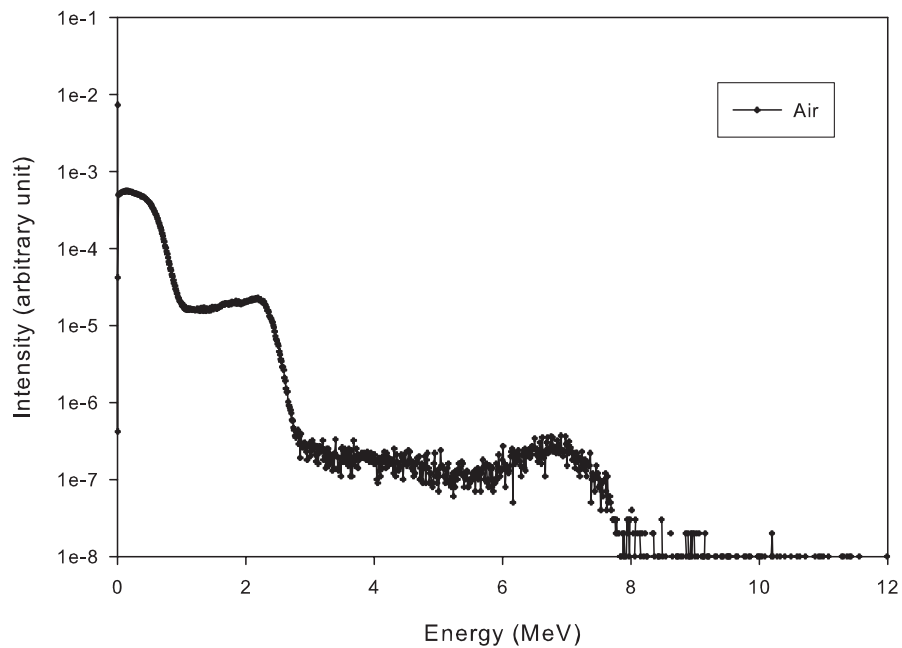
Figure 4.28 The pulse height spectrum resulted from activation of Air by Cf-252 source.
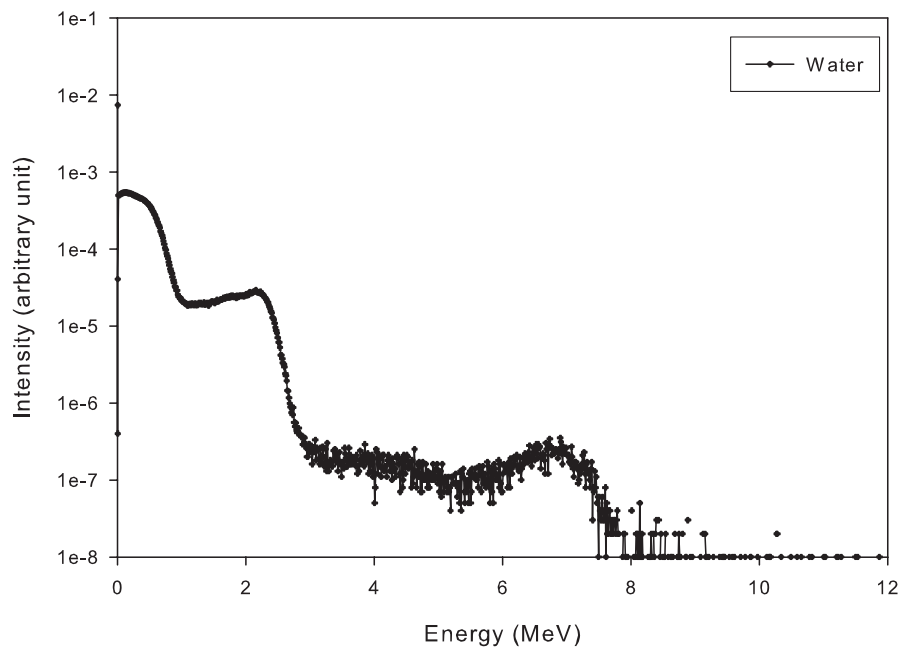
Figure 4.29 The pulse height spectrum from activation of Water by Cf-252 source.
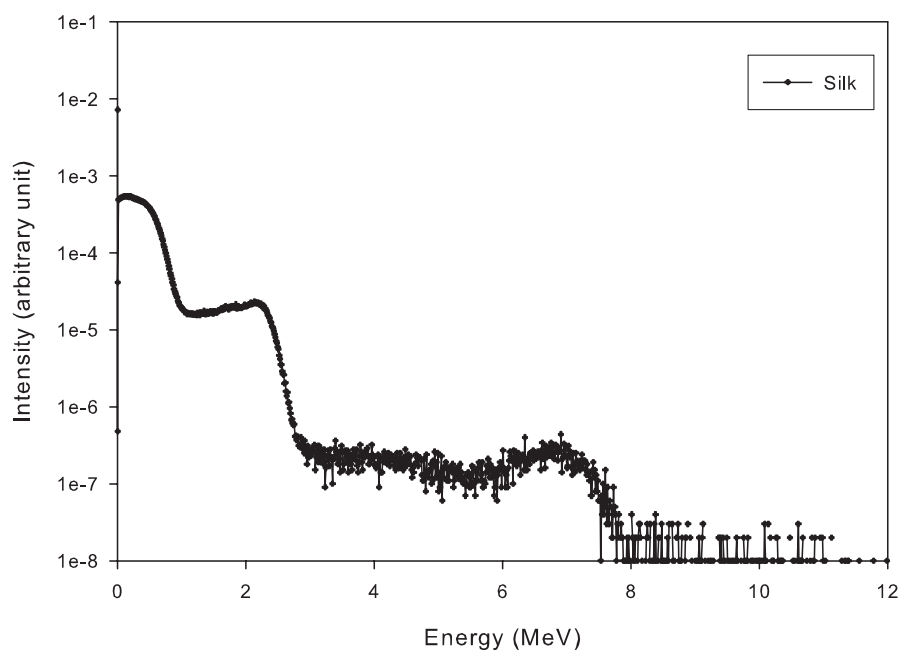
Figure 4.30 The pulse height spectrum from activation of Silk by Cf-252 source.
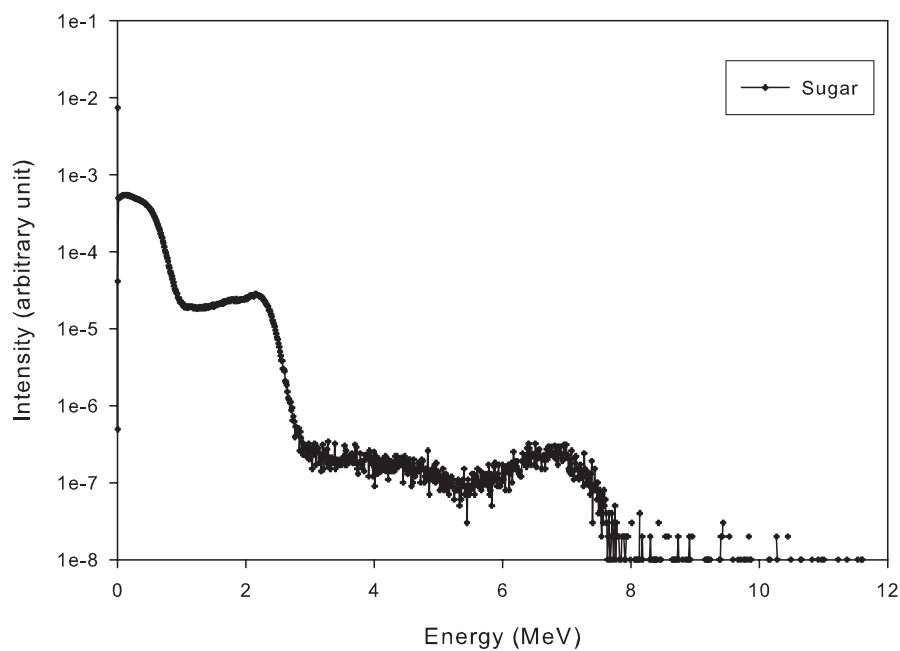
Figure 4.31 The pulse height spectrum from activation of Sugar by Cf-252 source.
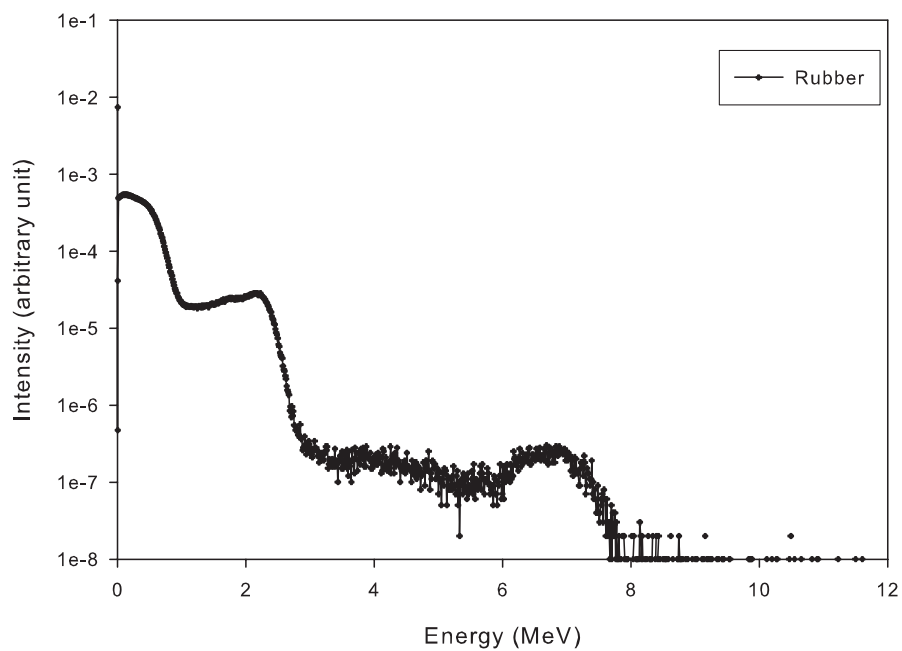
Figure 4.32 The pulse height spectrum from activation of Rubber by Cf-252 source.
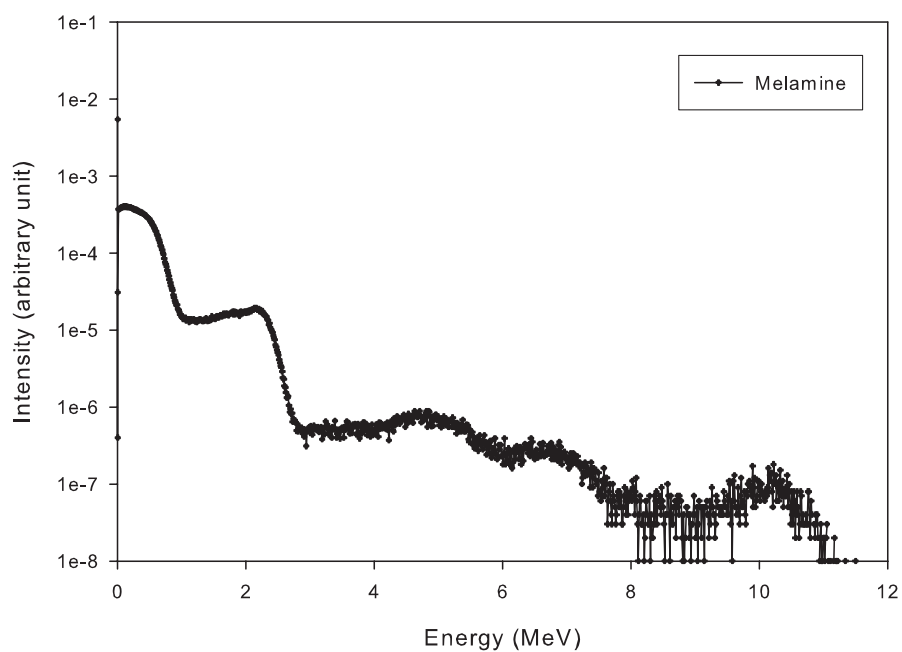
Figure 4.33 The pulse height spectrum from activation of Melamine by Cf-252 source.
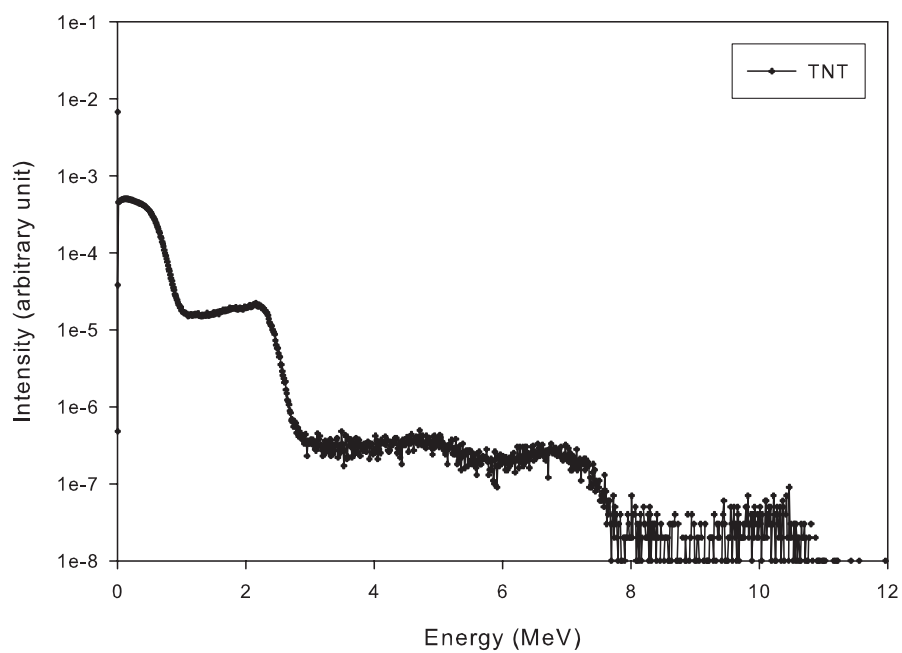
Figure 4.34 The pulse height spectrum from activation of TNT by Cf-252 source.
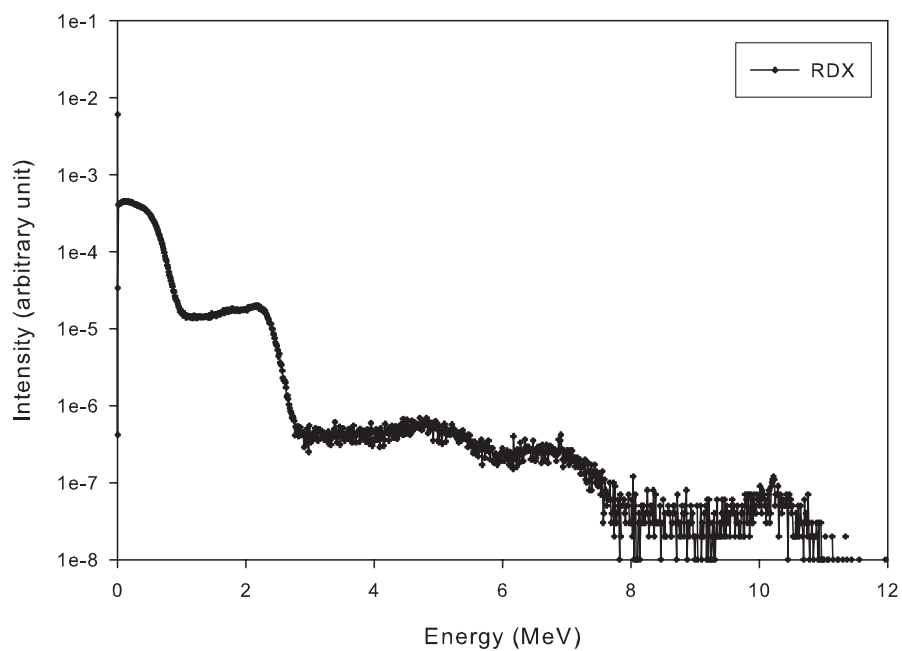
Figure 4.35 The pulse height spectrum from activation of RDX by Cf-252 source.

4.1.7 Thermal neutron flux at the center of the small geometry

To investigate the optimum thickness of the moderator, the thermal neutron flux created at the center of the small geometry by using Cf-source is simulated in this thesis This flux is based on the F-4 tally with the unit of n/cm^2-s. Figures 4.36–4.40 show the simulation results of fluxes (in unit of n/cm^2-s per source neutron) as a function of moderator thicknesses when heavy water, graphite, paraffin, polyethylene and light water are used as the moderators, respectively.

In the first two cases, fluxes increase monotonically with moderator thickness but have not yet reached saturation when the moderator thickness reaches 30 cm. Fluxes of the rest reach about the same highest values or the optimum values when the moderator thicknesses reach about 15 cm. These results agree with the values of moderating power of materials as shown in Table 2.4 Due to the economic and practical reasons, paraffin is selected as the moderator of the experimental geometry. Additionally, the simulation of flux distribution in the inspection cavity (on x-y plane at z=0) was performed. The result shows that flux is highest at the center and drops monotonically toward the edges as shown in Figure 4.41.
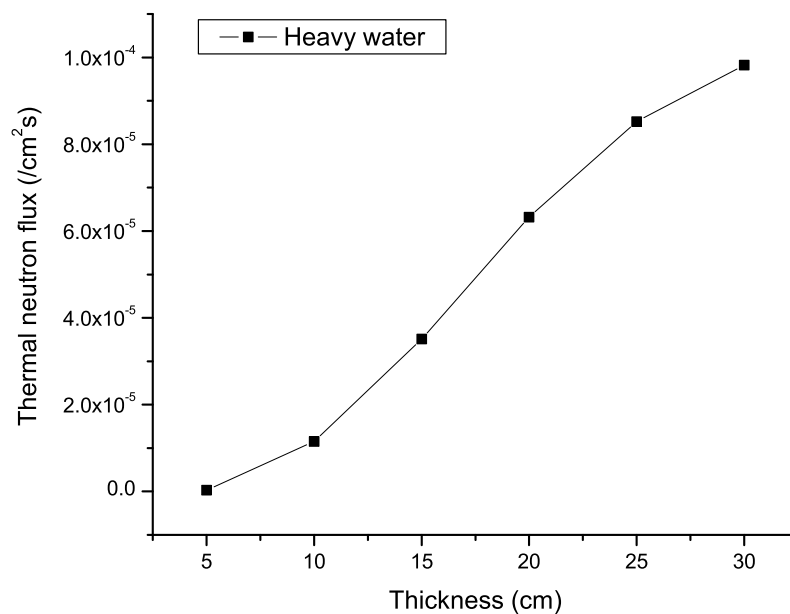
Figure 4.36 Thermal neutron flux at the center of the small geometry as a function of heavy water thickness.
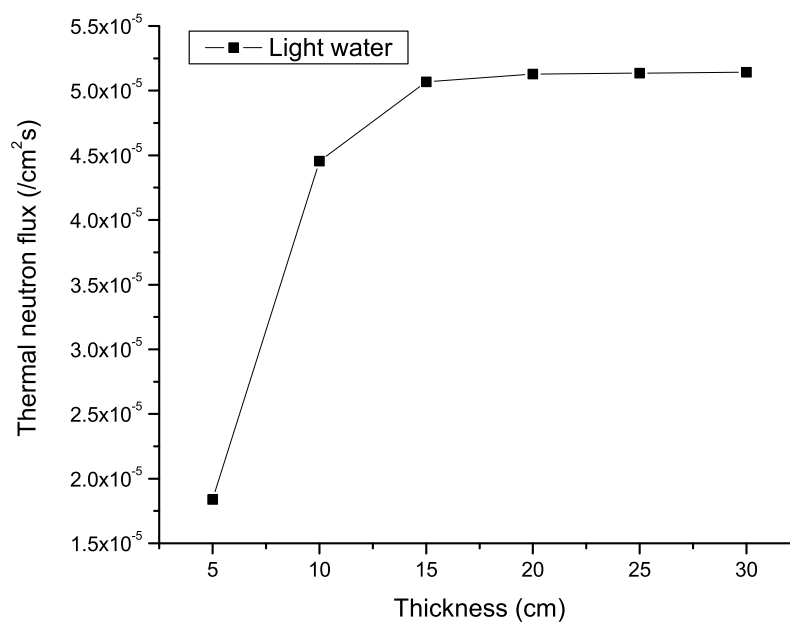
Figure 4.37 Thermal neutron flux at the center of the small geometry as a function of light water thickness.
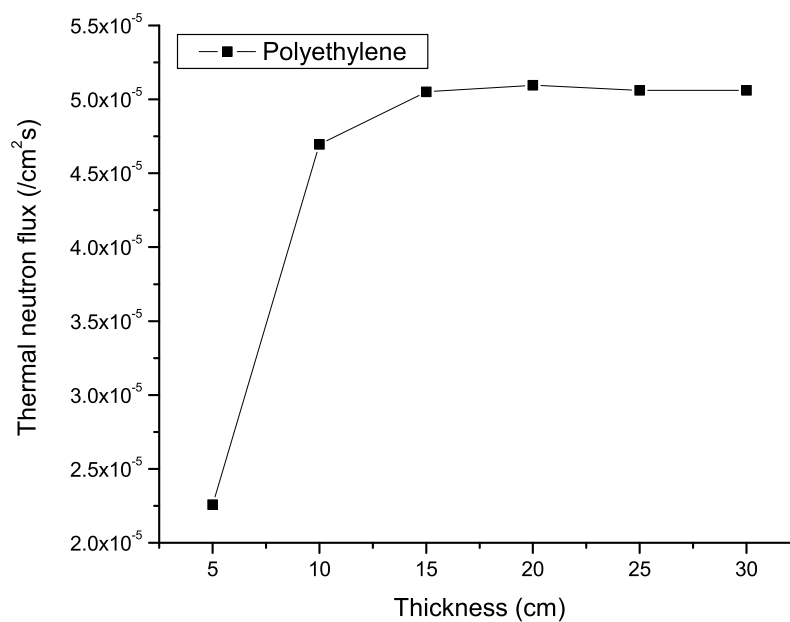
Figure 4.38 Thermal neutron flux at the center of the small geometry as a function of polyethylene thickness.
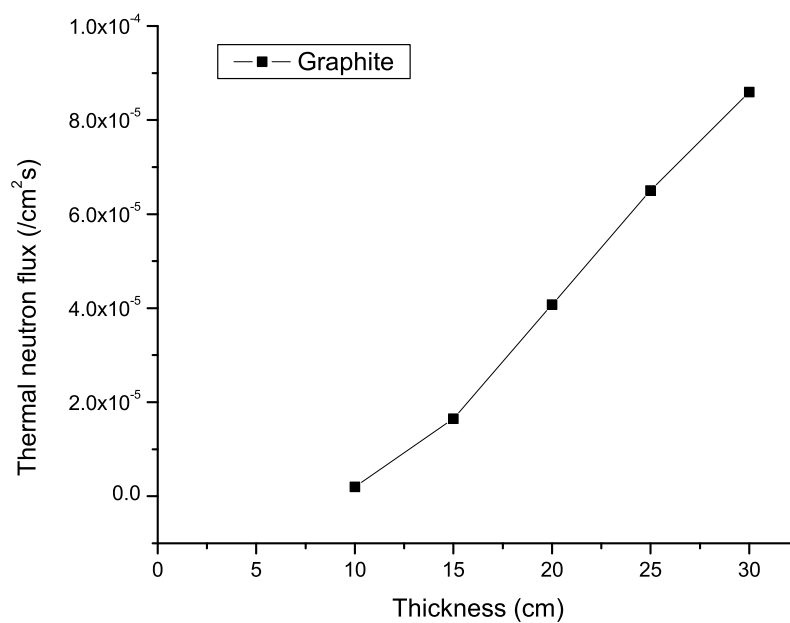
Figure 4.39 Thermal neutron flux at the center of the small geometry as a function of graphite thickness.
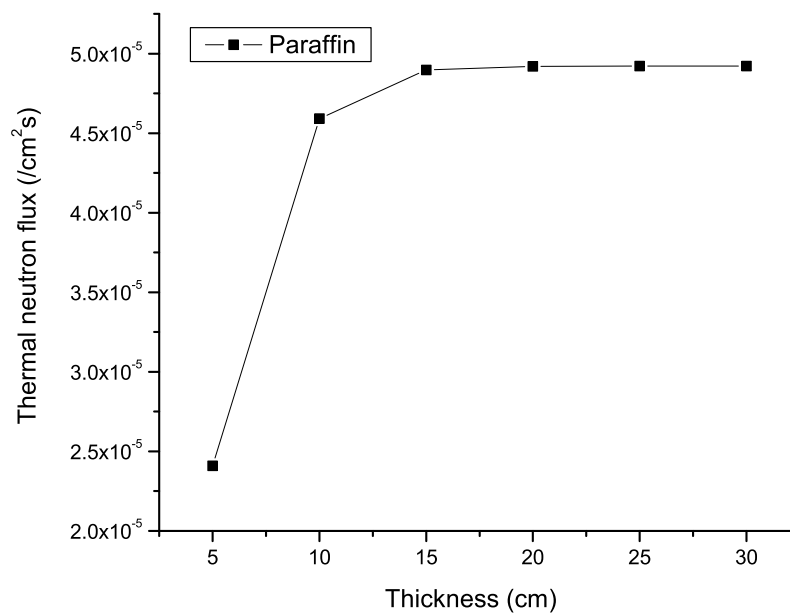
Figure 4.40 Thermal neutron flux at the center of the small geometry as a function of paraffin thi
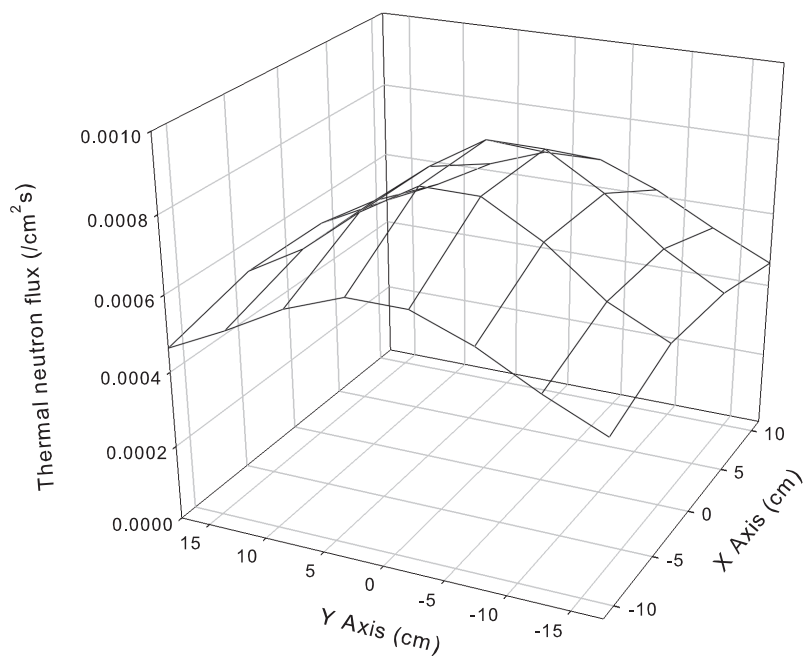
Figure 4.41 Thermal neutron flux distribution in the inspection cavity(on x-y plane at z=0) of the experimental geometry.

4.1.8 Thermal neutron flux at the center of the large geometry

With the reason given in Section 3.2.3, the large geometry is designed and used for simulation. The thermal neutron flux distribution characteristic as a function of moderator thickness is simulated. Three types of moderators, namly, heavy water, light water and polyethylene and three types of neutron sources, namely, Cf, Am/Be and D-D are used in the simulations.
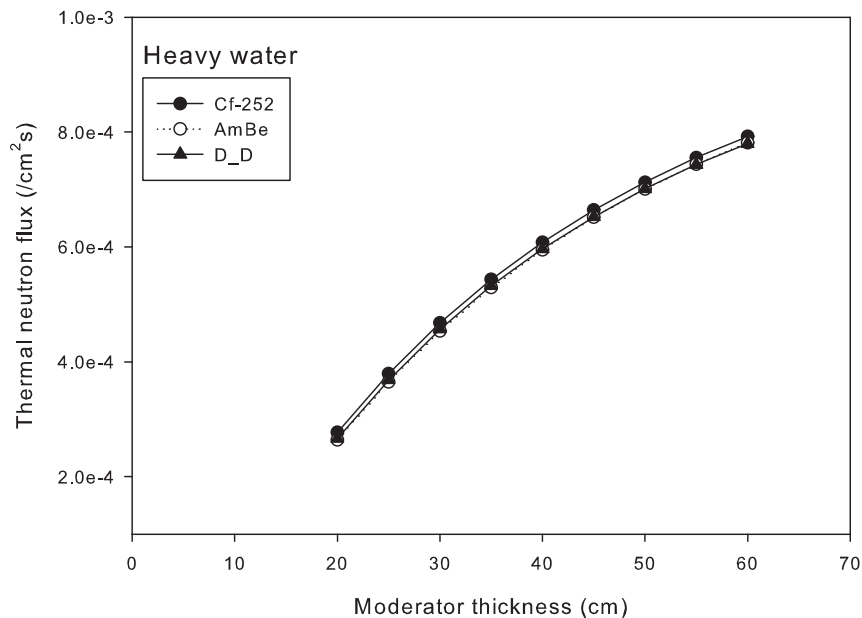
Figure 4.42 Thermal neutron flux at the center of the large geometry as a function of heavy water thickness .

Figures 4.42–4.44 show the results of fluxes at the center of the large geometry as a function of moderator thicknesses when heavy water, light water and polyethylene are used as moderators, respectively. For heavy water, the fluxes from all sources are almost the same and increase monotonically with moderator thicknesses. These fluxes have not reached saturations even with the moderator
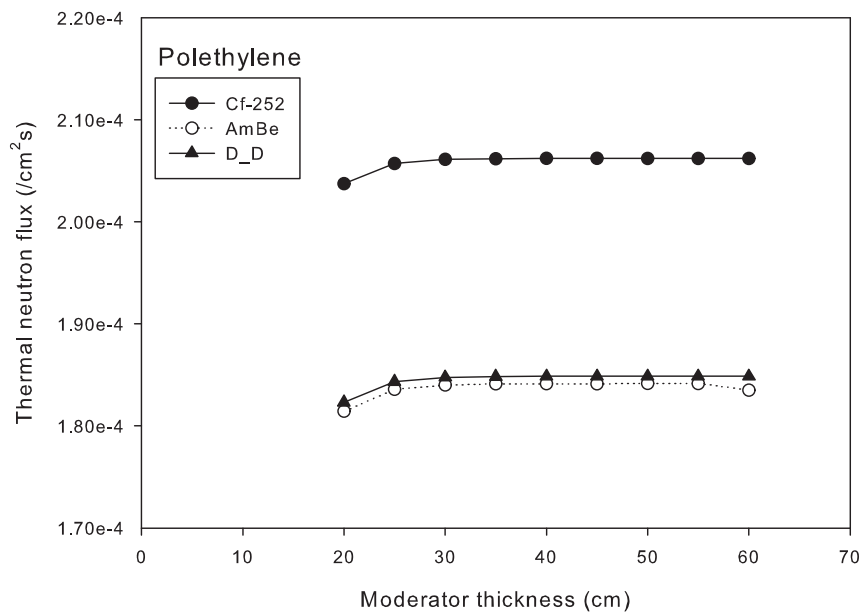
Figure 4.43 Thermal neutron flux at the center of the large geometry as a function of polyethylene thickness .
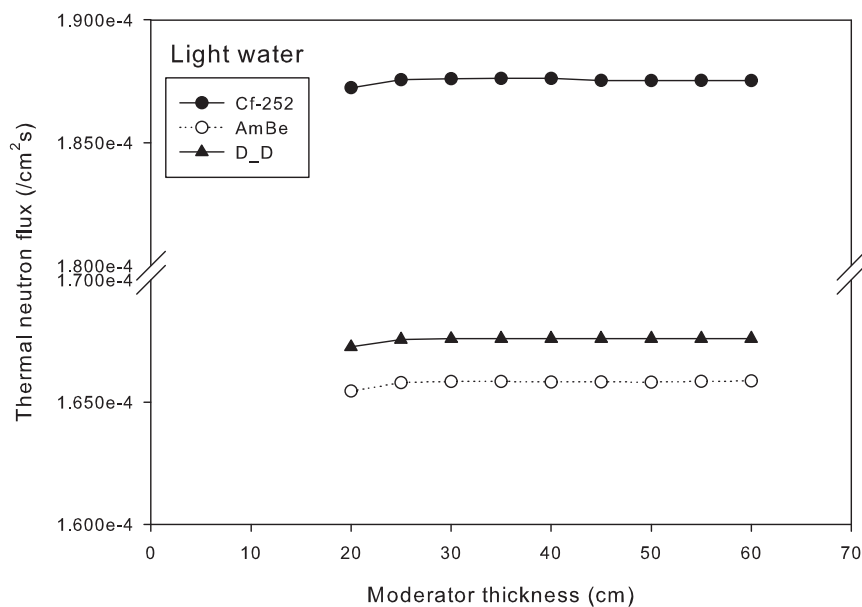
Figure 4.44 Thermal neutron flux at the center of the large geometry as a function of light water thickness.

thickness of 60 cm. For polyethylene, fluxes due to Cf are the highest with about 15 percents higher than those values from Am/Be and D-D. The flux values due to Cf reach the optimum value at about 30 cm of moderator thickness. The similar characteristics are also observed in the case of using light water as the moderator. However, its flux values are about 10 percents lower than those from polyethylene.

4.1.9 Doses at the outer surfaces of the large geometry

Another interesting simulation that was performed in this thesis is the dose levels at the outer surfaces of the large geometry.

Figure 4.45 shows the result from the simulation of total dose (in unit of pico Seivert) as a function of moderator thickness at the outer surfaces of the EDS in x, y, z axes when using polyethylene as the moderator. All the x-, y- and z -axes doses are about the same with the x -axis dose being the highest while the y- axis dose is the lowest. Since the total dose is the combination of gamma ray and neutron doses, the simulation of radiation dose is also performed to investigate about their attributions. Figure 4.46 shows simulation results of primary, secondary and neutron doses as a function of moderator thickness at the outer surfaces of the EDS in x axis when using polyethylene as the moderator. This figure shows that gamma ray doses are higher than neutron dose. To compare the dose level among different types of moderators, the simulations of doses due to heavy and light water were also performed. Figure 4.47 shows the comparison of total doses at the outer surfaces of the large geometry in x axis between heavy water, light water and polyethylene. It is interesting that heavy water gives the lowest dose while polyethylene and light water give about the same values. This result shows that heavy water which gives the highest moderating power also gives the highest shielding power. In addition, the simulations of doses due to using
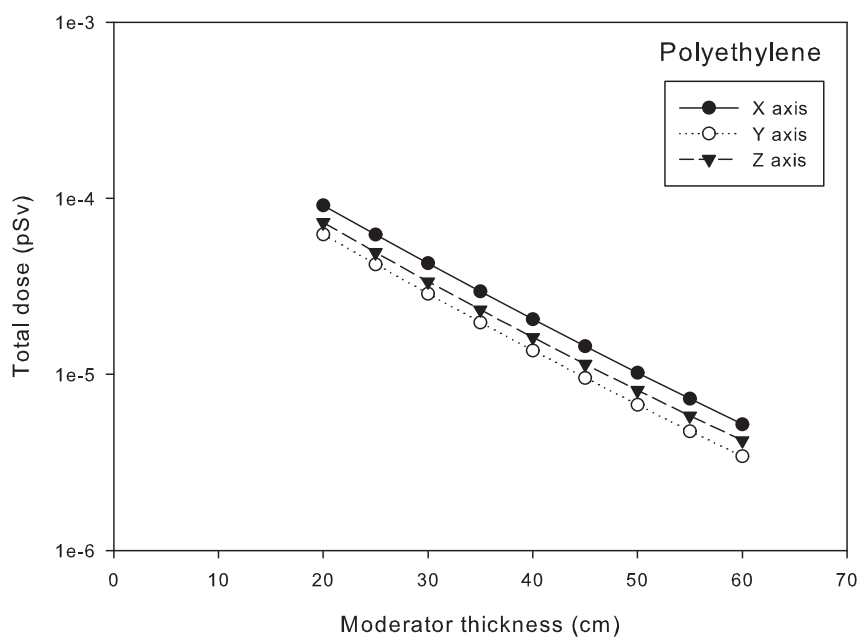
Figure 4.45 Total doses at the outer surfaces of the large geometry in x,y,z axes when using polyethylene as the moderator and Cf as the neutron source.
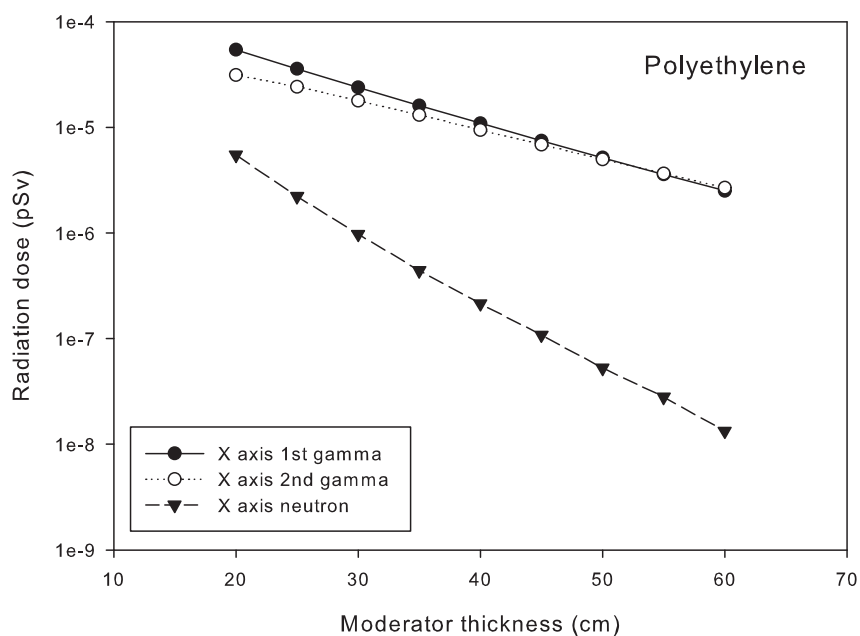
Figure 4.46 Radiation doses at the outer surfaces of the large geometry in x axis when using polyethylene as the moderator and Cf as the neutron source.
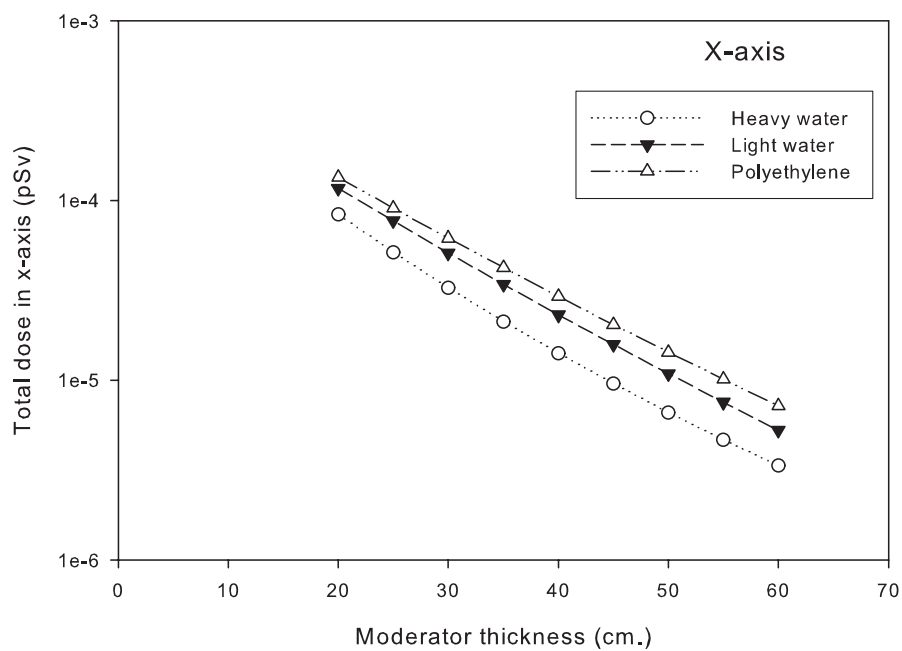
Figure 4.47 Comparison of total doses at the outer surfaces of the large geometry in x axis when heavy water, light water and polyethylene are used as the moderators.
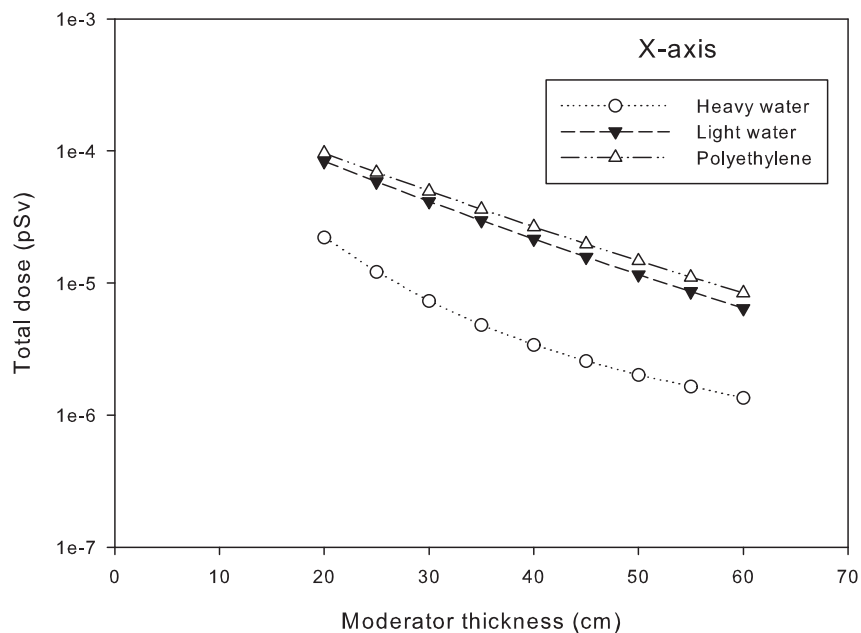
Figure 4.48 Total doses at the outer surfaces of the large geometry in various moderators when using Am/Be as the neutron source.
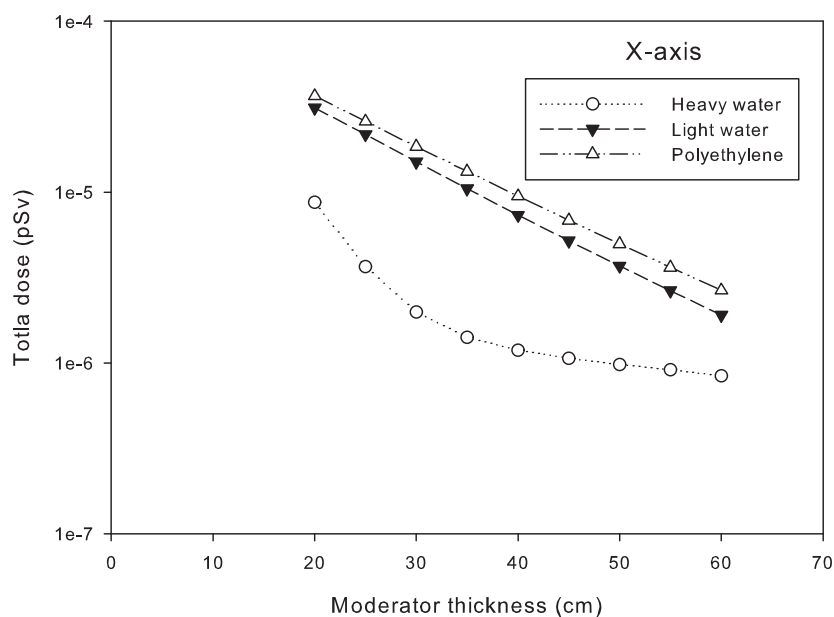
Figure 4.49 Total doses at the outer surfaces of the large geometry in various moderators when using D-D as the neutron source.

Am/Be and D-D as neutron sources were also performed. The same characteristics of total doses are also occurred when using these sources as shown in Figures 4.48 and 4.49, respectively. However, their total dose levels are different with that of Cf the highest and that of D-D the lowest. At 20 cm thickness of polyethylene, Cf gives dose about 10 and 20 times higher than that of Am/Be and of D-D, respectively.

4.1.10 Gamma ray attenuation and backscatter analysis

Since the Cf- source also produces gamma rays, it can be used as a gamma ray source for gamma ray attenuation and backscatter simulations. These simulations will provide additional indicators for explosive identification. With this reason, the gamma ray attenuation and backscatter are simulated in this the-

sis. In this simulations, primary gamma rays from Cf -252 with an average energy of 2.3 MeV are used to incident an various samples located at the center of the large geometry. Twelve samples as listed in Table 4.3, each with dimensions of $15 \times 30 \times 10$ cm^3, were used in the simulations. Two gamma ray detectors are used in the simulation, one for transmission and the other for backscattering. The transmission detector located at the top of the inspection cavity while the backscattering one sat next to the gamma ray source, looking at the center of the inspection cavity. These two detectors were used to count the numbers of transmitted and backscattered gamma rays. Assuming the source gamma ray intensity is I_0 and the transmitted gamma ray intensity is I, the logarithmic of the (I_0/I) ratio or $\ln(I_0/I)$ will be proportional to the sample density as given by equation (2.12). The estimation of this ratio is performed in this thesis for all samples appeared in Table 4.3 with the results shown in the last column. These results in this table show that the values of $\ln(I_0/I)$ are proportional to the sample densities.

When the transmitted gamma ray intensities are plotted against the backscattered intensities, the result will appear as shown in Figure 4.50. This figure shows the mapping of transmitted and backscattered intensities due to various samples, which can be grouped into three groups: Group I composes of C-4 and RDX (all are explosives); Group II composes of TNT, sugar and melamine (combination of an explosive and common materials); Group III composes of the rest of the samples (common materials and drug). This mapping shows that most samples are separated from explosives and drug, except sugar and melamine (as shown in group II). Therefore, the additional indicator is required to distinguish them from explosive. The combination of $\ln(I_0/I)$ and this mapping can serve that purpose.

Table 4.3 Results from the gamma ray attenuation of some interesting materials.

Material	Density(kg/m^3)	I	Io/I	$\ln(Io/I)$
Aluminium	2700	1.02E-05	3.12	1.14
C-4	1830	1.45E-05	2.20	0.79
RDX	1816	1.46E-05	2.19	0.78
TNT	1650	1.57E-05	2.03	0.71
Sugar	1590	1.56E-05	2.04	0.71
Melamine	1570	1.60E-05	1.99	0.69
Cocaine	1300	1.78E-05	1.80	0.59
Nylon	1140	1.89E-05	1.68	0.52
Rubber	950	2.07E-05	1.54	0.43
Wood	850	2.28E-05	1.40	0.34
Wool	600	2.43E-05	1.31	0.27
Silk	200	2.79E-05	1.15	0.14
Air	1.3	3.19E-05	1.00	0
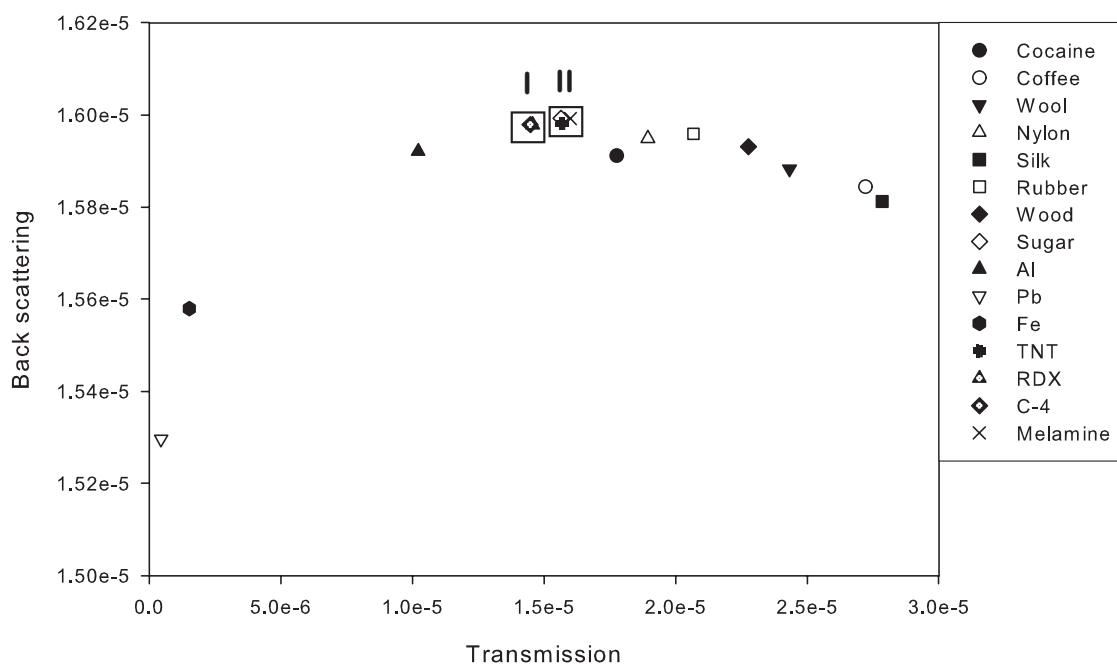
Figure 4.50 Mapping of the transmitted and backscattered gamma ray intensities resulted from the incident of source gamma rays on samples.

4.1.11 Source strength estimation

The source strength estimations required for various detection sensitivities for detecting TNT and RDX are performed in this thesis. These estimations are based on the detections of the 10.8 MeV gamma rays resulted from the activations of TNT and RDX with neutrons from Cf-252. To facilitate these estimations, fluxes of the 10.8 MeV gamma rays resulted from the activations must be known. The simulations results shown in Figure 4.51. Reading from the bottom graph of Figure 4.51, if the desired sensitivity for the detection of TNT is 300 g, the 10.8 MeV gamma ray flux detected by gamma ray detector will read 4.22×10^{-9} per source particle. By using this value of flux, the required source strength, S, can then be estimated from the formula $S = cps/\phi_\gamma$, where cps and ϕ_γ are the number of count per second and flux of the 10.8 MeV gamma rays, respectively.
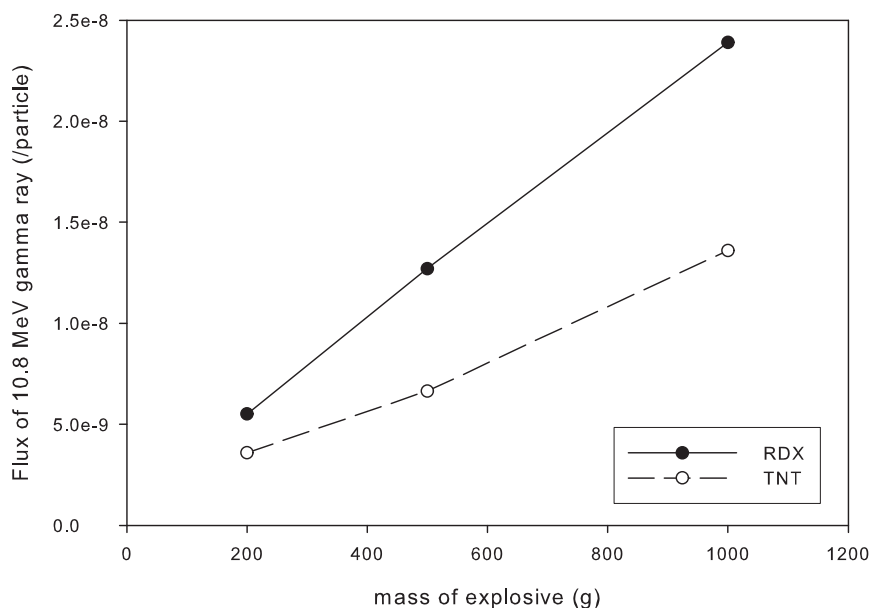
Figure 4.51 Fluxes of the 10.8 MeV gamma rays resulted from activations of TNT and RDX with neutrons from Cf-252.

In this application, the signal to noise ratio of 2 can be assumed and the required minimum flux of the10.8 MeV gamma rays can be about 100. Taking this value of minimum flux and choosing a reasonable counting time of 40 seconds, cps = 100/40 = 2.5. The above formula will then give the required source strength, S = $2.5/(4.22 \times 10^{-9})$ = 5.9×10^8 n/s. This result implies that, the source strength of Cf-252 of 5.9×10^8 n/s is required to detect TNT of 300 g. With the same source strength and cps values, the 10.8 MeV gamma ray flux detected by the gamma ray detector for the case of RDX inspection can, in turn, be estimated by using the above formula to be 4.22×10^{-9} per source particle. Extrapolating the top graph of Figure 4.51 by using this flux value, the estimated sensitivity for the detection of RDX reads about 150 g. The RDX detection sensitivity is twice better than that of TNT. Therefore, if the desired sensitivities for detections of

TNT and RDX of 300 and 150 g, respectively, the required source strength will be 5.9×10^8 n/s. Further more, the same kind of simulation was done by using D-D as the neutron source. It was found that the similar result is obtained. There fore, Cf and D-D source give similar detection sensitivity.

4.1.12   Dose rate estimation

If the source strength of the EDS is the same as in the last section, 5.9×10^8 n/s the maximum doses at the outer surfaces of the EDS can be estimate as follows. From the known source strength, S, the maximum total dose rate received by the control operator in one year can be estimated from the formula H=D $\times$ S $\times$ t, where D is the absorbed dose and t is the time period that the control operator works with the EDS in 1 year (52 w/y $\times$ 5 d/w $\times$ 8 h/d $\times$ 3600 s/h = 7.49×10^6 s). For the case of using 45 cm thick polyethylene as the moderator with neutron and gamma ray shielding materials of 5 and 0.5 cm thick, respectively, D = 7.04×10^{-6} pSv. Therefore, the maximum total dose rate received by the control operator is 7.04×10^{-18}Sv $\times$ 5.9×10^8n/s $\times$ 7.49x10^6s = 0.03 Sv/y. This value is well under the whole body ICRP's MPD of 0.05 Sv/y (ICRP 75, 1997).

4.2   Experimental results

To compare some results form MCNP simulations with experimental results, an experiment was performed at CIAE, Beijing, China. The details of experimental setup are discussed in Section 3.4. The results from this experiment are discussed in the following sections.

4.2.1 Thermal neutron flux at the center of the experimental geometry

The thermal neutron flux at the center of the experimental geometry was measured in the experiment by using a ^{3}He detector. The detector's tube has a volume of 76.18 cm^3 (2.5 cm diameter and 9.7 cm long) with the pressure of 4.5 atm. It contains the number of ^{3}He atoms (N^{He}) of 5.38×10^{21}. The thermal neutron flux, ϕ_{th}, can be estimated from the following equation:

$$\phi_{th} = \frac{cps}{N^{He} \times \sigma} \qquad (4.1)$$

where cps is the number of counts per second, N^{He} is the number of ^{3}He atoms in the detector's tube and σ is the neutron absorption cross section . Three measurements of cps were done in the experiment with results of 19703, 19347, 19551. Therefore, the average value of $cps = 19533$. Since $\sigma = 5327 \times 10^{-24}$ cm^2, equation (4.1) gives the thermal neutron flux of 68.10±0.63 n/cm^2.s. Since from the MCNP simulation, the thermal neutron flux (in the unit of track length) is 2.02×10^{-4} cm/source neutron and the source strength is 2.125×10^7 n/s, the thermal neutron flux is $2.02 \times 10^{-4} \times 2.125 \times 10^7 = 4.29 \times 10^3$cm n/s. Dividing this result by the detector volume of 76.18 cm^3, the thermal neutron flux from MCNP simulation is 90±9 n/cm^2.s. The experimental result is about 22 percents different from the simulation result.

4.2.2 Pulse height spectra resulted from activation of TNT by Cf-source

TNT of 1000, 520 and 200 g were put in the center of the experimental geometry for activations by Cf- neutrons for 900 s. The pulse height spectra

resulted from these activations are shown in Figure 4.52. The spectra resulted from activations of air (no sample in the cavity) with the same counting time are also measured in the experiment and included in this figure.
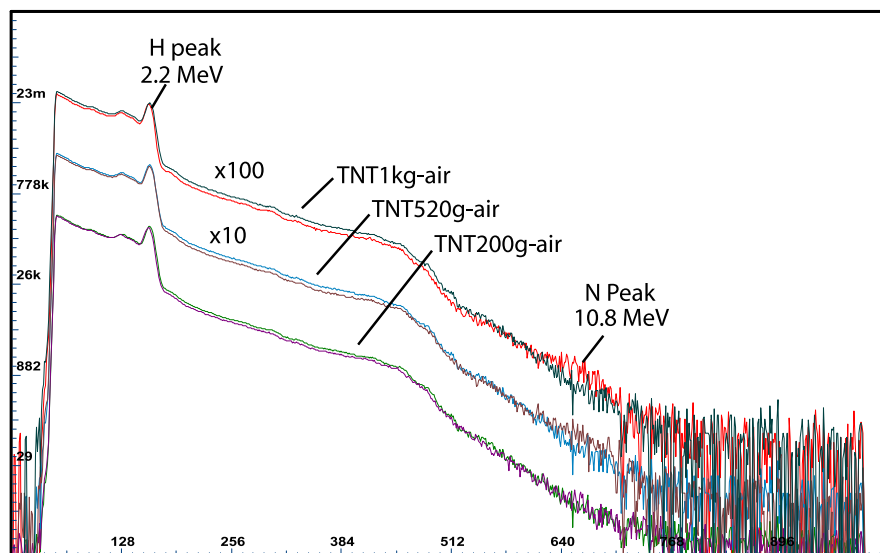
Figure 4.52 Pulse height spectra resulted from activations of the 1000, 520 and 200 g of TNT by Cf-neutron for 900 s.

To make the spectra well separated from each others for better visualization, the data from the measurements of 1000, 520 g and their respective air activation results are multiplied by 100 and 10, respectively. In each spectrum, the 2.22 MeV peak from H is clearly shown while the 10.8 MeV region from N is low in intensity. This region comprises of the photo peak, the single and double escapes of the 10.8 MeV gamma ray. The low intensity feature of N-region is similar to the TNA energy spectrum of C-4 simulant of 300 g as shown in Figure 4.53 (Gozani, 1996).

Since very high portion of the H-peaks comes from H-contents of paraffin moderator, only the N-regions are used for comparison with MCNP simulation results. In the deduction for the intensity of the 10.8 MeV gamma rays, its photo peak and the single and double escape peaks are included. The energy region for
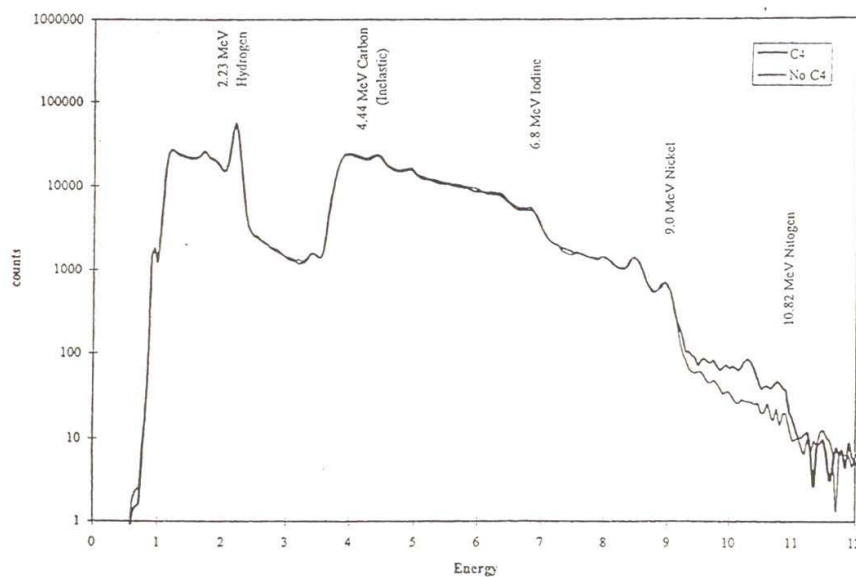
Figure 4.53 lPulse height spectra resulted from activations of the 300 g of C-4 by AmBe-neutron (Gozani, 1996).

this deduction covers from 9.45 to 11.43 MeV as shown in Figure 4.54. Intensities from the deductions are 481, 307 and 76 for 1000, 520 and 200 g, respectively. Dividing these numbers by their corresponding masses and counting time, the detection sensitivities are 0.53, 0.65 and 0.42 counts/s-kg for 1000, 520 and 200 g, respectively. Figure 4.55 shows a graph of the detection sensitivity values, from experiment, as a function of TNT's mass. The line drawn is the mean value of 0.53 counts/s-kg. The corresponding theoretical value can be estimated from the MCNP simulation based on F4 tally. The result from this simulation is shown in Figure 4.51 of section 4.1.11. It is the flux of the 10.8 MeV gamma rays resulted from activation of 1000 g TNT by Cf-source in the large geometry. From that figure flux of the 10.8 MeV gamma rays is 2.4×10^{-8}/source neutron. To facilitate comparison of this result to that from experiment, we need to scale this flux value into the value of the experimental geometry by using the relationship between configurations of the two geometries. The gamma ray flux of the experimental
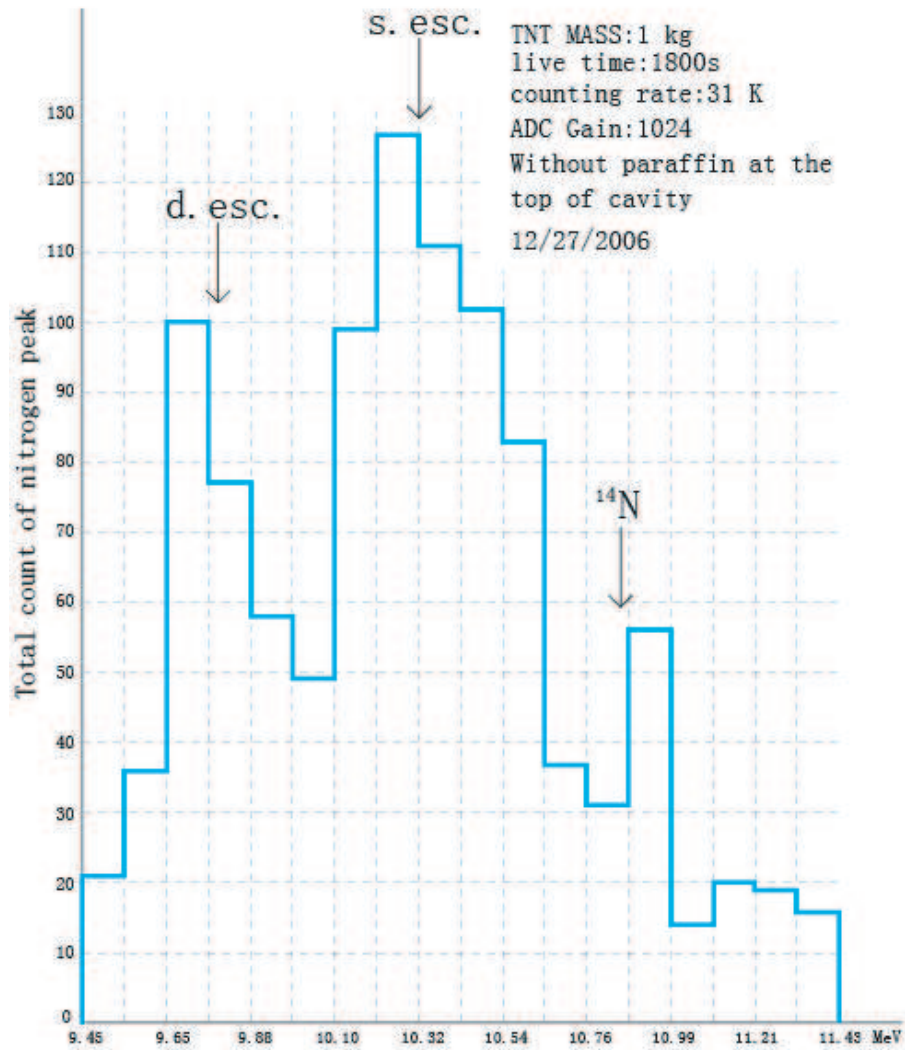
Figure 4.54 Energy region for the deduction of the 10.8 MeV gamma rays resulted from activation of 1000 g of TNT.
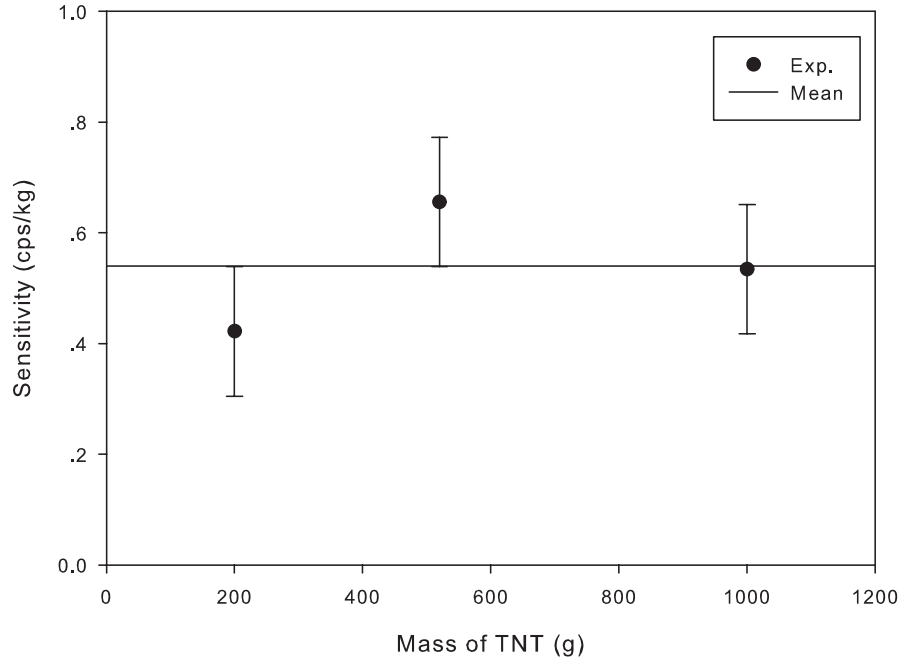
Figure 4.55 The detection sensitivity for the TNT inspection as a function of TNT's mass.

geometry, N_1, can be given in term of the gamma ray flux of the large geometry, N_2, as

$$\mathrm{N}_1 = N_2 \frac{\phi_{1th}}{\phi_{2th}} \times \left(\frac{r_1}{r_2}\right)^2 \times \left(\frac{R_2}{R_1}\right)^2 \times \frac{V_1}{V_2} \qquad (4.2)$$

where ϕ_{1th} and ϕ_{2th} are the thermal neutron fluxes created in the experimental and the large geometries, respectively. r_1 and r_2 are the radius of the detectors used in the experimental and the large geometries, respectively. R_1 and R_2 are the distances from the centers of the respective geometries to the centers of their respective detectors , $V - 1$ and V_2 are volumes of the detectors used in the experimental and large geometries respectively. The data for these parameters are: $N_2 = 1.35 \times 10^{-8}$, $\phi_{1th} = 2.02 \times 10^{-4}$, $\phi_{2th} = 2.05 \times 10^{-4}$, $r_1 = r_2 = 3.81$ cm, $R_1 = 16.31$ cm, $R_2 = 23.81$ cm, $V_1 = V_2 = 34.73$ cm^3. Substituting these values in equation (4.2), $N_1 = 2.83 \times 10^{-8}$/source neutron. Multiplying this result by

source strength value of 2.125×10^7 n/s and dividing by TNT's mass of 1 kg, we obtained the detection sensitivity of the experimental geometry 0.60 counts/s-kg. This result is about 13% different from the experimental value.

4.2.3 Effect of the detector collimation

To investigate the effect of the detector collimation, the NaI detector was collimated by lifting it up vertically about 6 cm from the original position. This lifting reduced the solid angle of the detector which in turn reduced the chance of detecting unwanted gamma rays resulted from activation of H-contents of paraffin moderator. There fore, the 2.2 MeV gamma ray intensity should be reduced when compare to the uncollimated value. Figure 4.56 shows the comparison between the collimated and uncollimated spectra for measurements of 1000 g of TNT. Comparing the intensities of the 2.2 MeV lines between these two spectra, the reduction of intensity is about 40 percents. This result shows that, if the detector collimation is good enough the photo peak area of the 2.2 MeV line can be used as an additional indicator for explosive identification.

4.2.4 Pulse height spectrum from activation of TNT by Am/Be-source

To investigate the characteristic of gamma ray spectrum resulted from activation of TNT by Am/Be-source (Vitorelli et al., 2005), the measurement of this spectrum was performed in this experiment. Figure 4.57 shows the result from this measurement with 1000 g of TNT put in the inspection cavity and the counting time of 900 s. In this measurement, the inspection cavity was surrounded by the lead bricks of 5 cm thick. These bricks act as a shielding to reduce the chance of unwanted gamma rays originated from H-contents of paraffin moderator to be detected by the gamma ray detector. There are two objectives for this measurement:
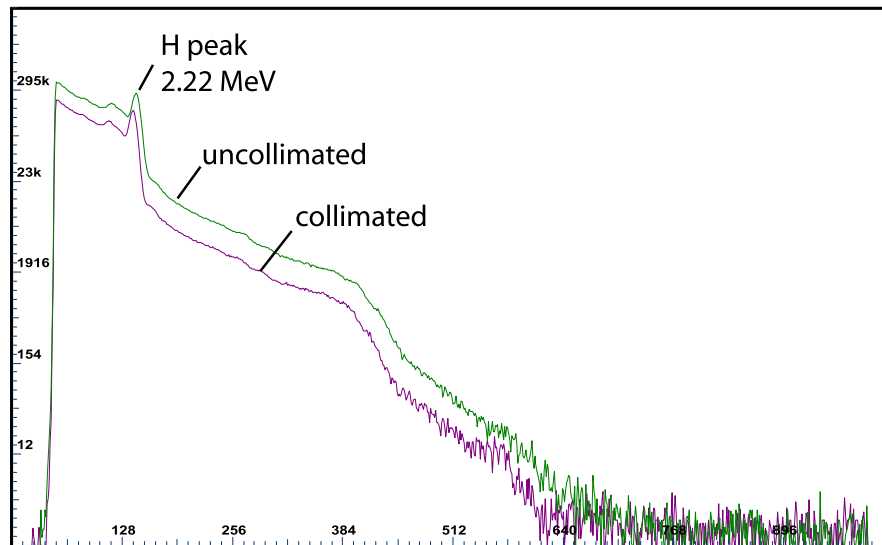
Figure 4.56 Comparison of gamma ray spectra detected by the collimated and uncollimated detectors.

1) to investigate whether the inelastic nuclear reaction is possible or not and 2) to estimate the effect of the shielding of inspection cavity.
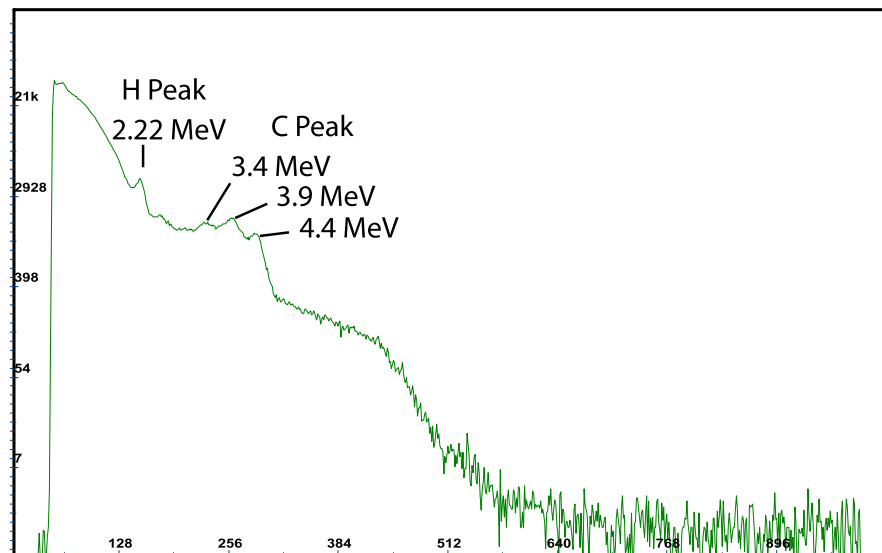
Figure 4.57 Gamma ray spectrum resulted from activation of TNT of 1000 g for 900s by Am/Be -source.
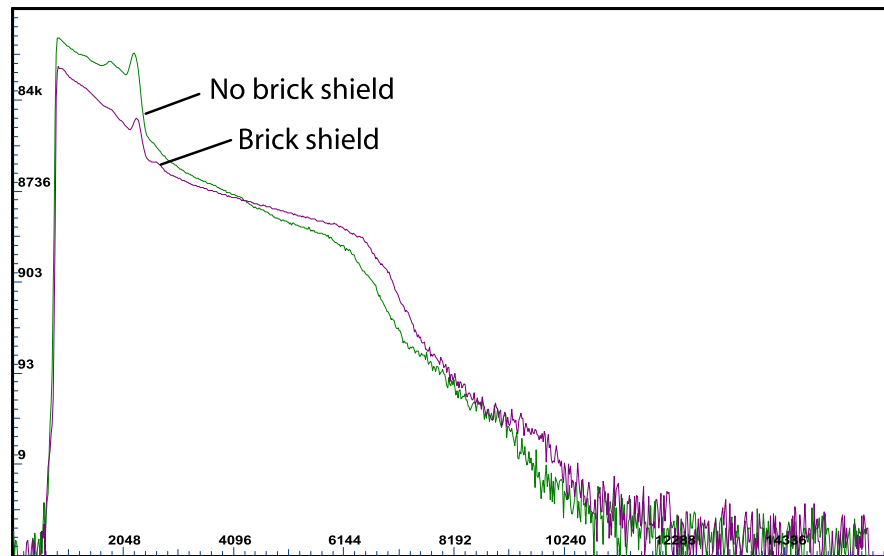
Figure 4.58 Gamma ray spectrum of TNT with brick shield and no brick shield.

It is clear from the spectrum that the inelastic nuclear reactions are possible because the 4.4 MeV line and its' single escape (3.9 MeV) and double escape (3.4 MeV) from C appear on the spectrum. The spectrum also shows that the intensity of the 2.2 MeV line reduced by about 100 percents when compare to that of the unshielded value (as shown in Figure 4.58). Deducing intensities of the gamma rays appear on this spectrum, we obtain intensities of 14,816, 8,860 and 222 for the 2.2, 4.4 and 10.8 MeV gamma rays respectively. Therefore the experimental intensity ratios of H/C, H/N and C/N from TNT's spectrum are 1.7, 67 and 40, respectively. The comparison between the experimental ratio of H/C with its' theoretical values can be obtained by using the formula,

$$H/C = \sigma_H A_H \epsilon_H / \sigma_C A_C \epsilon_C \tag{4.3}$$

where $\sigma_H = 0.33$b, $A_H = 5$, $\epsilon_H = 1$, $\sigma_C = 0.1$, $A_C = 7$, $\epsilon_C = 0.86$. Substituting these values in equation (4.3), we obtain the theoretical vale of H/C = 2.7. Following the same procedures for estimations of H/N and C/N with $\sigma_N = 0.011$b, $A_N = 3$, and $\epsilon_N = 0.8$, we obtain their theoretical ratios of 62.5 and 22.8, respec-

tively. These values are about 37, 7 and 43% different from experimental values, respectively. The differences between the experimental and theoretical ratio of H/C and C/N are quite high. However, these are only rough estimates which have not included background subtractions in the processes of intensity deductions.

Some of the gamma ray emissions resulted from activations of H- and C-contents of moderator are still detected by the gamma ray detector. These effects attribute to the differences between experimental and theoretical ratios.

4.2.5 Pulse height spectrum from activation of KCl and NaCl by Cf-source

Since another objective of this thesis is to investigate the feasibility of using TNA technique for drug detection (Tumer et al., 1994) , the activations of KCl and NaCl by Cf-neutrons was performed in this experiment. The idea is to investigate whether the TNA technique can detect Cl, an important elemental composition of drug, or not. Figure 4.59 shows the gamma ray spectrum resulted from activation of KCl and NaCl by Cf-source. As shown in the spectrum, all the Cl-gamma ray lines both from high energy and low energy regions present in the spectrum. The high energy region lines comprise of the 5.71 MeV ($\sigma = 1.86$ b), the 6.11 MeV ($\sigma = 7.37$ b) and the 6.62 MeV ($\sigma = 2.75$ b). The low energy region lines comprise of the 0.78 MeV ($\sigma = 4.9$ b),the 1.16 MeV ($\sigma = 8.92$ b) and the 1.95 MeV ($\sigma = 6.49$ b). These gamma ray lines agree with the results from Choi et al. technique (Choi et al., 1999). They show that TNA technique can provide a good mean for drug detection.
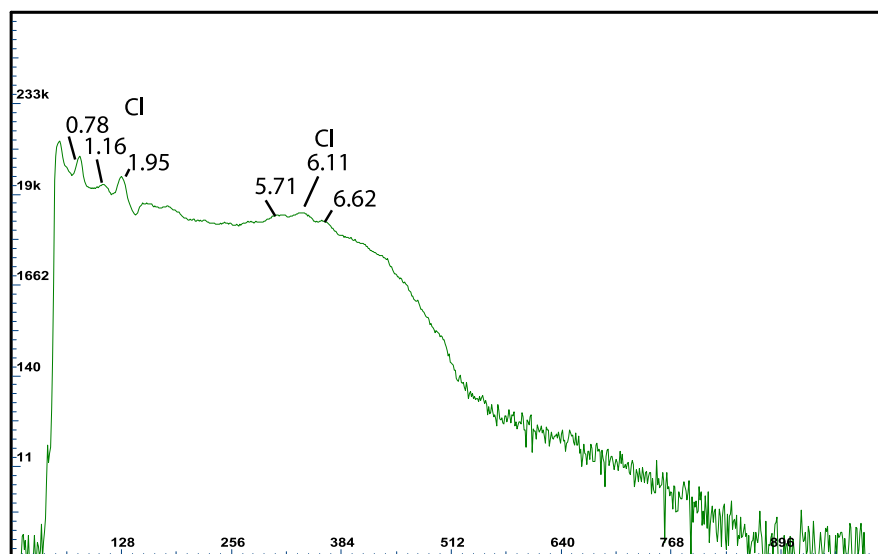
Figure 4.59 Gamma ray spectrum resulted from activations of KCl and NaCl by Cf-source.

4.2.6   Radiation dose measurement

In the experiment at CIAE, the measurements of gamma ray and neutron doses were performed. The doses at 1 m away from the surfaces of the experimental geometry in x- and y- directions were measured. The results are shown in Table 4.4 with their respective MCNP simulation values. Through neutron and gamma ray dose values from MCNP simulations and experiment are quite large, the differences between total doses are acceptable. The x- and y-directions total doses differences are 10 and 28%, respectively. By using the x-direction total dose of 9.43 μSv/hr, the maximum total dose at 1 m away from the surface can be estimated. In 1 year (1.49×10^6 s), the maximum dose is $(9.43 \times 10^{-6}$Sv/h$) \times (1.49 \times 10^6$ s$)/3600$ s/h $= 0.004$ Sv/y. This value is 75% over the ICRP public limit of 0.001 Sv/y.

Table 4.4 Neutron and gamma doses at 1 m away from the surfaces of the experimental geometry in x- and y-directions

Radiation dose	MCNP results (μSv/hr)		Experiment (μSv/hr)	
1m from	X-direction	Y-direction	X-direction	Y-direction
Neutron dose	8.19	5.00	5.00±0.08	2.34±0.15
Gamma dose	2.32	1.27	4.43±0.28	2.50±0.16
Total dose	10.51	6.27	9.43±0.36	4.84±0.31

CHAPTER V

CONCLUSIONS

In this chapter, MCNP simulations, experimental results and comparisons between them are concluded. The conclusions will be based on the following topics.

5.1 Gamma rays resulted from neutron activations of elements

As discussed in Sections 4.1.1-4.1.3, all gamma ray lines which are important for explosive identification present in the spectra resulted from activation of H, C, O and N by Cf- and Am/Be- sources. These lines are the results of thermal and fast reactions which include the 2.23, 4.43, 6.13 and 10.81 MeV from H, C, O and N, respectively. Other gamma ray lines with low intensities are also present. However, since they have low intensities, they will be buried under the Compton continuum of the experimental gamma ray spectra. When the energy cut off technique is used with the Am/Be-source, all the lines due to the thermal reactions in explosive elemental compositions (H, C, O, N) disappeared while those due to the fast reactions remained. These results show that our simulations are consistent.

5.2 Gamma rays resulted from neutron activations of materials

In Sections 4.1.4 and 4.1.5, the gamma ray lines resulted from thermal and fast activations of explosives and common materials by Cf- and Am/Be-sources

were discussed. It was found that all the gamma ray lines present in the spectra correspond to elemental compositions of the materials activated. The 2.23, 4.43, 6.13, 10.81 MeV lines which are necessary for explosive identification present concurrently in the TNT and RDX spectra. In other spectra, only some of them present. Further more, the 6.13 MeV line due to activation of O by Am/Be -source is stronger than that from Cf-source. This result tends to suggest that Am/Be-source is better than Cf-source for explosive identification.

5.3 Pulse height spectra resulted from neutron activations of materials

As discussed in Section 4.1.6, all gamma ray lines due to activations of explosive and common materials by Cf, are not visible in their pulse height spectra except the 10.8 MeV region in TNT, RDX and Melamine spectra. This result suggest that only 10.8 MeV gamma rays may be useful for explosive identification.

5.4 Thermal neutron flux at the center of the small geometry

As discussed in Section 4.1.7, the thermal neutron flux at the center of the small geometry was simulated by using heavy water, graphite, light water, paraffin as the moderators. The simulation results show that heavy water and graphite give higher moderating powers than the rest. However, due to practical and economic reasons, paraffin of 15 cm is select to be the moderator of the experimental geometry.

5.5 Gamma ray attenuation and backscatter

As shown in Table 4.2 of Section 4.1.10, gamma ray attenuation can be used as an additional indicator for better explosive identification. Table 4.2 shows that materials of different densities exhibit different values of $\ln(I/I_0)$. Therefore the value of $\ln(I/I_0)$ can be used to differentiate between explosive and common materials. Furthermore, the mapping of gamma ray transmission and backscatter intensities can give an additional indicator for explosive identification. This characteristic can be seen in Figure 4.50 of Section 4.1.10.

5.6 Source strength estimation

As discussed in Section 4.1.11, the source strength required for the inspections of TNT and RDX can be estimated by using the thermal neutron flux created at the center of the large geometry. It was found that for inspection of 300 g of TNT, Cf-source must have source strength of 5.9×10^8 n/s. This source strength value can be used to detect 150 g of RDX. This results show that Cf-source with a certain source strength can detect RDX with higher sensitivity than that of TNT.

5.7 Comparisons of MCNP simulation results with experiment

The following Sections conclude about comparisons of the MCNP simulation results with experiment.

5.7.1 Thermal neutron flux at the center of the experimental geometry

Comparisons of thermal neutron fluxes at the center of the experimental geometry between MCNP simulation and experimental results are discussed in Section 4.2.1. The MCNP simulation and the experimental values are 90.0 ± 9.0 and 68.10 ± 0.63 n/cm^2-s, respectively. These two values are about 22% different which is quite large.

5.7.2 Radiation doses at points around the experimental geometry

Comparison of radiation doses between MCNP simulation and experimental results are discussed in Section 4.2.2 with the results shown in Table 4.3. For neutron doses at 1 m away from the geometry's surfaces in X- and Y-directions, the differences in total dose are about 10 and 28%, respectively. The differences are not so large.

5.7.3 Detection sensitivity

The detection sensitivities for inspections of TNT of 1000, 520 and 200 g are discussed in Section 4.2.3. The experimental results are 0.53, 0.65 and 0.42 counts/s-kg for the inspections of 1000, 520 and 200 g TNT, respectively. The mean value of these values is 0.531 counts/s-kg. The corresponding MCNP simulation value is 0.60 counts/s-kg. The two values agree with each other very well with the difference about 13%.

5.7.4 Pulse height spectrum from activation of TNT by Am/Be-source

To investigate the effect of shielding of the inspection cavity, the pulse height spectrum resulted from activation of TNT by Am/Be-source was measured with the results shown in Figure 4.44 of Section 4.2.4. It is clear from the spectrum that the 2.2 MeV line reduced by about 100 percents when compare to that of the unshielded value. Further more, the 4.43 MeV gamma rays from C presents in the spectrum. The intensity deductions of the 2.2, 4.43 and 10.8 MeV gamma ray lines are performed and their ratios estimated. It was found that the experimental ratios of H/C, H/N and C/N are 1.7, 67, 40, respectively. The corresponding theoretical values are 2.7, 62.5 and 22.8, respectively. These two ratios are about 37, 7 and 43% different, respectively.

5.7.5 Pulse height spectrum resulted from activation of KCl and NaCl by Cf-source

To investigate whether the TNA technique can be used to detect drug or not, the spectrum resulted from activations of KCl and NaCl by Cf-neutrons was measured experimentally. The resulted is shown in Figure 4.45 of Section 4.2.5. It was found that all gamma ray lines from Cl are observed in the spectrum. This result suggests that the TNA technique may be capable of detecting drugs.

5.7.6 Suggestions for further study

Results from this study suggested that improvement are required to make FTNGA (combinations of FNA, TNA and GAA) the practical explosive detection method. Experimental results show that activation of TNT by Cf-source can not

produce gamma ray lines due to fast reactions from C and O. Furthermore, intensity of the 10.8 MeV line is rather weak because the source strength (2.125×10^7 n/s) is too low. In fact the simulation result based on the large geometry suggested that the required source strength should be around 5.9×10^8 n/s. However, when Am/Be-source was used to activate TNT, the 4.43 MeV gamma ray line from C presents in its pulse height spectrum. More over, when the inspection cavity is shielded properly, the 2.2 MeV line from H becomes useful and the estimations of H/C, H/N and C/N ratios are possible.

The above observations suggested that Am/Be-source with larger source strength, larger gamma ray detector with higher detection efficiency (such as BGO), better shielding of the inspection cavity and better collimation of gamma ray detector should be used for further study.

REFERENCES

REFERENCES

วรศิษย์ อุชัย, (2002). เทคโนโลยีในการตรวจวัตถุระเบิดและยาเสพติด, **วารสารเทคโนโลยี
สุรนารี**, 9, หน้า 219–229.

Al-Jarallah, M.I., et al. (2003). Neutron moderation in a bulk sample and its effects on PGNAA setup geometry, **Radiation Measurements**, 36, pp. 471-474.

Brown, D.R. and Gozani, T. (1995).Cargo inspection system based on pulsed fast neutron analysis, **Nuclear Instruments and Methods in Physics Research B**, 99, pp. 753-756.

Choi, et al. (1999). Database of Prompt Gamma Rays from Slow Neutron Capture for Elemental Analysis, **Nuclear Data Section**, IAEA, Vienna, Austria.

Cywicka-Jakiel, T., Loskiewicz, J. and Tracz, G. (2001). The Monte Carlo Simulation of the Fast Neutron and Gamma-ray Transmission Setup for Humidity Measurement of Coke, **Department of Environmental and Radiation Transport Physics, The Henryk Niewodniczanski Institute of Nuclear Physics, Polish Academy of Sciences, Krakow, Poland**, 1887, pp. 1-18.

Gavrish, Y.N.,Sidorov, A.V. and Fialkovskii, A.M. (2003). Nondestructive Elemental Analysis in Searching for Explosive and Fissioning Materials During Customs Inspection of Cargo, **Atomic Energy**, v. 95, pp. 480-485

Gozani, T., et al. (1989). Explosive detection system based on thermal neutron activation, **IEEE**, 52, pp. 17-20.

Gozani, T., Elsalim, M. and Phillips, E. (2003). Gamma ray spectroscopy features for detection of small explosives, **Nuclear Instruments and Methods in Physics Research A**, 505, pp. 482-485.

He, D.F. (2002). Metal detector based on high-Tc RF SQUID, **Physica C**, pp. 1404-1407.

Hussein, E.M.A. and Lord, P.M. (1990). An empirical fast-neutron technique for detection of explosive-like materials, **Nuclear Instruments and Methods in Physics Research A 299**, pp. 453-457.

Hussein, E.M.A. (2003). **Handbook on Radiation Probing Gauging, Imaging and Analysis**, Kluwer Academic Publishers, Netherlands.

ICRP 75, (1997). General Principles for the Radiation Protection of Worker, 75 Vol. 27/1, 1997.

Kiefer, H. and Maushart, R. (1972). Radiation Protection Measurement, **Pergamon press**.

Lamarsh, J.R. and Baratta, A.J. (2001). **Introduction to Nuclear Engineering**, Upper Saddle River, New Jersey: Prentice Hall, pp. 52-88.

Lin, M.S., Hsieh, B.R. and Su, A.C. (2004). **Fluorescent conjugated polymer films as TNT chemosensors**, Synthetic Metals 144, pp. 297-301.

Muhrer, G., et al. (2007). Comparison of the measured and the calculated total thermal neutron cross-section of Pb, **Nuclear Instruments and Methods in Physics Research A**, 572, pp. 866-873.

Nordlund, A., et al. (2001). Measurements of water content in geological samples using transmission of fast neutrons, **Nuclear Instruments and Methods in Physics Research A**, 462, pp. 457-462.

Nunes, W.V., da Silva, A.X., Crispim, V.R. and Schirru, R. (2002). Explosives detection using prompt-gamma neutron activation and neural networks, **Applied Radiation and Isotopes**, 56, pp. 937-943.

Oliveira, C., Salgado, J., Botelho, M.L. and Ferreira, L.M. (2000). Dose determination by Monte Carlo-a useful tool in gamma radiation process, **Radiation Physics and Chemistry**, 57, pp. 667-670.

Ostafin M. and Nogaj, B. (2007). **N14-NQR based device for detection of explosives in landmines**, Measurement, 40, pp. 43-54.

OTA report. (1991). **Technology Against Terrorism: The Federal Effort**.

Overley, J.C. (1985). Determination of H, C, N, O content of bulk materials from neutron-attenuation measurements **International Journal of Applied Radiation and Isotope**, 36, pp. 185-191.

Overley, J.C., et al. (1995). Explosives detection through fast-neutron time-of-flight attenuation measurements, **Nuclear Instruments and Methods in Physics Research B**, 99, pp. 728-732.

Overley, J.C., et al. (2006). Explosives detection via fast neutron transmission spectroscopy, **Nuclear Instruments and Methods in Physics Research B**, 251, pp. 470-478.

Park, et al. (2004). Gamma ray transmission imaging detectors using a double gap resistive plate chamber, **Nuclear Instruments and Methods in Physics Research A**, 533, pp. 144-148

Pinnaduwage, L.A.,Thundat, T., Gehl, A. and Wilson, S.D. (2004). Desorption characteristics of uncoated silicon microcantilever surfaces for explosive and common nonexplosive vapors, **Ultramicroscopy**, 100, pp. 211-216.

Porter, L.J. (1999). The use of Thermal neutron analysis in unexploded ordnance and mine detection, **SPIE Conference on Penetrating Radiation Systems and Applications**.

Reilly, D., Ensslin, N., Smith, J.H., and Kreiner, S. (1991). Passive Nondestructive Assay of Nuclear Materials, **Los Alamos National Laboratory**, Los Alamos, New Mexico.

Rynes, J., et al. (1999). Gamma-ray and neutron radiography as part of a pulsed fast neutron analysis inspection system, **Nuclear Instruments and Methods in Physics Research A**, 422, pp. 895-899.

Sanin, V.M., et al. (1994). Aplication of accelerated particles for explosives identification, **NSC KIPT, Kharkov, Ukraine**.

Sang Hai-feng a, Wang Fu-li a, Liu Lin-mao b, Sang Hai-jun. (2005). Detection of element content in coal by pulsed neutron method based on an optimized back-propagation neural network, **Nuclear Instruments and Methods in Physics Research B 239**, pp. 202–208.

Sawa, Z.P. (1993). PFN GASCA technique for detection of explosives and drugs, **Nuclear Instruments and Methods in Physics Research B**, 79, pp. 593-596.

Schaeffer, N.M. (1973). Reactor shielding for nuclear engineers, **U.S. Atomic Energy Commission Office of Information Services**, pp 83-93.

Shea, P. and Gozani, T. (1990). A TNA explosives-detection system in airline baggage, **Nuclear Instruments and Methods in Physics Research A**, 299, pp. 444-448.

Shtejer-Diaz, K., et al. (2003). Determination of neutron flux distribution in an Am-Be irradiator using the MCNP, **Nuclear Instruments and Methods in Physics Research A**, 353, pp. 646-649.

Shue, S.L., Faw, R.E. and Shultis, J.K. (1994). Fast neutron thermalization and capture gamma-ray generation in soils, **Department of Nuclear Engineering, Kansas State University, Manhattan, KS**.

Singleterry, R.C. and Thibeault, S.A. (2000). Materials for Low-Energy Neutron Radiation Shielding, **Langley Research Center, Hampton, Virginia**.

Smith, R.C., Hurwitz, M.J. and Tran, K.C. (1995). System to detect contraband in cargo containers using fast and slow neutron irrodiation and collimated gamma detectors, **Nuclear Instruments and Methods in Physics Research B**, 99, pp. 733-735.

Speller, R. (2001). Radiation-based security, **Radiation Physics and Chemistry**, 61, pp. 293-300.

Steward, S., and Forsht, D. (2005). Use of nuclear techniques to determine the fill of found unexploded ordnance, **Applied Radiation and Isotopes**, 63, pp. 795-797.

Sohrabpour, M., Shahriari, M., Zarifian, V. and Moghadam, K.K. (1999). Borehole prompt gamma neutron activation and comparison with Monte Carlo

simulation using MCNP code, **Applied Radiation and Isotopes**, 50, pp. 805-810.

Sood, A., et al. (2004). Verification of the pulse height tally in MCNP5, **Nuclear Instruments and Methods in Physics Research B**, 213, pp. 167-171.

Strellis, D. and Gozani, T. (2005). Classifying threats with a 14-MeV Neutron interrogation system, **Applied Radiation and Isotopes**, 63, pp. 799-803.

Tanimura, Y., Saegusa, J., Yoshizawa, M. and Yoshida, M. (2005). Design of a single moderator-type neutron spectrometer with enhanced energy resolution in the energy range from a few to 100 keV, **Nuclear Instruments and Methods in Physics Research A**, article in press.

Tartari, A., Bonifazzi, C., Felsteiner, J. and Casnati, E. (1996). Detailed multiple-scattering profile evaluations in collimated photon scattering techniques, **Nuclear Instruments and Methods in Physics Research B**, 117, pp. 325-332.

Tumer, T.O., Pierce, R.M. and Dotson, K.C. (1994). A Portable Narcotics Detector with Identification Capability, **SPIE**, 2276, pp. 255-265.

Tzika, F. and Stamatelatos I.E. (2004). Thermal neutron self-shielding correction factors for large sample instrumental neutron activation analysis using the MCNP code, **Nuclear Instruments and Methods in Physics Research A**, 213, pp. 177-181.

Uckan, T., et al. (2003). [241]AmBe Sealed Neutron Source Assessment Studies for the Fissile Mass Flow Monitor, **Oak Ridge National Laboratory**.

Vega-Carrillo, H.R., et al. (2002). Neutron and gamma-rays spectra of ^{239}PuBe and ^{241}AmBe, **Applied Radiation and Isotopes**, 57, pp. 167-170.

Victor, J. Orphan, Ernie Muenchau, Jerry Gormley and Rex Richardson. (2005). Advanced gamma ray technology for scanning cargo containers, **Applied Radiation and Isotopes**, 63, pp. 723-732.

Vitorelli, J.C., et al. (2005). Monte Carlo simulation of response function for a NaI(Tl) detector for gamma rays from ^{241}Am/Be source, **Applied Radiation and Isotopes**, 62, pp. 619-622.

Vourvopoulos, G. and Schultz, F.J. (1993). A pulsed fast-thermal neutron system for the detection of hidden explosives, **Nuclear Instruments and Methods in Physics Research B**, 79, pp. 585-588.

Vourvopoulos, G. (1994). Accelerator based techniques for contraband detection, **Nuclear Instruments and Methods in Physics Research B**, 89, pp. 388-393.

Vourvopoulos, G. and Womble, P.C. (2001). Pulsed fast/thermal neutron analysis:a technique for explosives detection, **Talanta**, 54, pp. 459-468.

Womble, P.C., Schultz, F.J. and Vourvopoulos, G. (1995). Non-destructive characterization using pulsed fast-thermal neutronns, **Nuclear Instruments and Methods in Physics Research B**, 99, pp. 757-760.

Womble, P.C., Vourvopoulos, G., Novikov, I. and Paschal, J. (2001). PELAN 2001: Current Status of the PELAN Explosives Detection System, **Proceedings SPIE conference on Hard X-Ray and Gamma-Ray Detector Physics, San Diego**.

X-5 Monte Carlo Team. (2003). MCNP-A General Monte Carlo N-Particle Transport Code., Version5, **Technical Report, Los Alamos National Laboratory**, Los Alamos, New Mexico.

Yang, X., Du, X.X., Shi, J. and Swanson, B. (2001). Molecular recognition and self-assembled polymer films for vapor phase detection of explosives, **Talanta**, 54, pp. 439-445.

Yazdi, M.H.H., Mowlavi, A.A., Thompson, M.N. and Hakimabad, H.M. (2004). Proper shielding for NaI(Tl) detectors in combined neutron-gamma fields using MCNP, **Nuclear Instruments and Methods in Physics Research A**, 522, pp. 447-454.

Yinon, j. (2002). Field detection and monitoring of explosives, **Analytical chemistry**, 21, pp. 292-300.

APPENDICES

APPENDIX A

INPUT FILE

A.1   F4 tally simulation of Spherical geometry

This input file is Am/Be source in the center of cavity.

```
Spherical cavity

1  1  -1000 -1 imp:n,p=1 $Carbon

2  2  -0.0013  1 -2 imp:n,p=1 $ air

3  3  -3.670   2 -3 imp:n,p=1 $ $ detector

4  0   3 imp:n,p=0


c Cylinder shell

1  so  2.5

2  so  7.5

3  so  8.5


mode  n  p

phys:p   4j    1

c  MATERIAL SPECIFICATION

m1 6012 1 $ C-single element

m2 8016 -0.000301 7014 -0.000976 $air

m3 11023 0.4995 53127 0.4995 $ NaI  detector

c    SOURCE SPECIFICATION
```

```
sdef  cell 1 pos= 0 0 0  rad=d1   erg=d2  par=1

si1   0   2.5

sp1   0   1

si2   h   0.11  0.33  0.54  0.75  0.97  1.18  1.40  1.61

          1.82  2.04  2.25  2.47  2.68  2.90  3.11  3.32

          3.54  3.75  3.97  4.18  4.39  4.61  4.82  5.04

          5.25  5.47  5.68  5.89  6.11  6.32  6.54  6.75

          6.96  7.18  7.39  7.61  7.82  8.03  8.25  8.46

          8.68  8.89  9.11  9.32  9.53  9.75  9.96  10.18

          10.39 10.60 10.82 11.03 11.09

sp2   d   0.000  0.014363  0.033397   0.031272  0.028119  0.025002

             0.021361   0.019831   0.017470   0.019248   0.022252

             0.021457   0.022482   0.022766   0.029506   0.035585

             0.036852   0.034583   0.030658   0.029987   0.026906

             0.028626   0.031784   0.030736   0.033340   0.030412

             0.027380   0.023319   0.020584   0.018152   0.017673

             0.020393   0.018299   0.016298   0.016773   0.016806

             0.018833   0.018374   0.016880   0.014352   0.009677

             0.006520   0.004255   0.003666   0.003805   0.005058

             0.006253   0.005519   0.004675   0.003695   0.002781

             0.001513   0.000363

c TALLY SPECIFICATION

f8:p  3

ft8  geb  0.4  0  0

f18:p 3

ft18 geb  0.0 0.05086  0.30486
```

```
f28:p 3

ft28  geb  0.007  0.014  0

f38:p 3

ft38  geb  0.0  0.05086  0.30486

f48:p 3 e0  0  1.0e-5  1.0e-3 1024i  12

F4:p 3 e4  0  1.0e-5  1.0e-3  1024i  12

nps  20000000
```

A.2 Thermal neutron flux in different moderating materials

This input file compose of heavy water, graphite, paraffin, polyethylene and light water.

```
Small cavity

c 1  2  -0.0013  1 -2 3 -4 5 -6 #6  imp:n,p=1 $Air

c 2  2  -0.0013  50 -51  52 -53 54 -55 #1 #6 imp:n,p=1 $Bag (Air)

3 2  -0.0013  120 -130 180 -190 240 -250 #6 #7 #8 #9 #10 #11

      #12 #13 #14 #15 #16 #17 imp:n,p=1 $Air Cavity

c 4  3  -1  110 -140 170 -200 230 -260 #3 #6 #7 #8 #9 #10 #11

c          #12 #13 #14 #15 #16 #17 #18 imp:n,p=1 $Water

5  3  -2.25 100 -150 160 -210 220 -270 #3 #6 #7 #8 #9 #10 #11

      #12 #13 #14 #15 #16 #17 #18 imp:n,p=1 $[Graphite]

6  0  -580  imp:n,p=1 $Sphere detector

7  like 6 but trcl=(0 0 6)

8  like 6 but trcl=(0 0 12)

9  like 6 but trcl=(0 0 18)
```

```
10 like 6 but trcl=(0 0 24)

11 like 6 but trcl=(3 0 12)

12 like 6 but trcl=(6 0 12)

13 like 6 but trcl=(9 0 12)

14 like 6 but trcl=(0 4 12)

15 like 6 but trcl=(0 8 12)

16 like 6 but trcl=(0 12 12)

17 like 6 but trcl=(0 16 12)

18 2   -0.0013 -550 560 -570 imp:n,p=1 $Source

20 0   -800 #3 #5 #6 #7 #8 #9 #10 #11 #12 #13 #14 #15 #16
          #17 #18 imp:n,p=1

21 0    800  imp:n,p=0


c C-4

1 pz -10

2 pz  10

3 py -7.5

4 py  7.5

5 px -1.5

6 px  1.5

c Bag

50 pz -13

51 pz  13

52 py -17

53 py  17

54 px -5
```

```
55 px   5

c Shielding

100 pz -30

110 pz -22

120 pz -15

130 pz  15

140 pz  22

150 pz  30

160 py -35

170 py -27

180 py -20

190 py  20

200 py  27

210 py  35

220 px -25

230 px -17

240 px -10

250 px  10

260 px  17

270 px  25

c Detector

c 500  cx   1.5

c Source Housing

550 pz  -15

560 pz  -25

570 cz   1.3
```

```
c Sphere

580  sz -12 1

800  so 100


mode  n  p
c  MATERIAL  SPECIFICATION
c m1    8016 6 6012 4 70146 1001 6 $C-4
c m1    6012 3 7014 6 1001 6 $ Melamine
c m1 8016 6 6012 3 7014 3 1001 11 $ Silk
c m1    6012 5 1001 8 $ Rubber
c m1 8016 4 6012 17 1001 21 7014 1  17000 21 $Cocaine+Cl
m2    8016 -0.000301 7014 -0.000976 $air
c m2 082207 -1   $Lead
c m3    6012 -0.7342 1001 -0.1475$ paraffin -0.95
c m3    1001  0.667954  6012  0.332046 $polyethylene -0.91
m3    6012  1 $graphite
c m4   8016 1  1001 2 $Water
c m4   1002 0.667  8016 0.333 $Heavy water -1.2
c m5     11023 0.4995 53127 0.4995 $ NaI  detector
c m5 82000.50c -11.35 $Pb
c    SOURCE SPECIFICATION
 sdef cel=18 pos= 0 0 -20   erg=d1 par=1
 si1  1  10i 14
 sp1   -3   1.025  2.926 c
TALLY SPECIFICATION
f4:n  6
```

```
f14:n 7

f24:n 8

f34:n 9

f44:n 10

f54:n 11

f64:n 12

f74:n 13

f84:n 14

f94:n 15

f104:n 16

f114:n 17

e0 1e-8 2e-8  t

nps 10000000
```

A.3   F8 tally simulation of experimental geometry

This input file compose of 500g TNT in the center of cavity.

```
480  1  -1.65  -600  imp:n,p =1 $TNT ball 500g R= 4.12 cm.

485  15 -0.0013 1 -5  11 -19 21 -27 600 imp:n,p =1

c Air cavity

489  4  -3.670  80 -85 -90 imp:n,p=1

c Z axis NaI detector

490  15 -0.0013 75 -88 -95 #(80 -85 -90) IMP:N=1 imp:p=1

c Air in NaI

495  32 -11.34  75 -88 -100 #490 #489 IMP:N=1 imp:p=1

c Pb Shield NaI
```

```
500  21 -1.4    70 -36 -105 #495 #490 #489 IMP:N=1 imp:p=1
```

c Boric Acid

```
510  32 -11.34  60 -61 62 -63 -64 65 IMP:N=1 imp:p=1
```

c Pb Shield Source

```
600  11 -0.952 31 -32 33 -34 35 -36 #(1 -5 11 -19 21 -27)
            #(60 -61 62 -63 -64 65) #500 #495 #490 #489 #480
                                    IMP:N=1 imp:p=1
700  0 -2000 #(31 -32 33 -34 35 -36) #500 #495 #490 #489 #480
                                    IMP:N=1 imp:p=1
800  0 2000 imp:n=0 imp:p=0
```

```
1     PX -15
2     PX -7.5
3     PX 0
4     PX 7.5
5     PX 15
11    PY -20
12    PY -15
13    PY -10
14    PY -5
15    PY 0
16    PY 5
17    Py 10
18    Py 15
19    Py 20
21    PZ -7.5
```

```
22    PZ -5

23    PZ -2.5

24    PZ 0

25    pz 2.5

26    pz 5

27    pz 7.5 c

31    px   -30.00000     $-6

32    px    30.00000

33    py   -34.00000

34    py    34.00000

35    pz   -37.500000

36    pz    27.500000     $NewSim
c

c Source Shield

60  px -5

61  px 5

62  py -5

63  py  5

64  pz -13

65  pz -23
c NaI Shielding layer

70 pz 9.5

75 pz 12.5

80 pz 13.5

85 pz 21.1

88 pz 32.6
```

```
90 cz 3.8

95 cz 5.5

100 cz 10.5

105 cz 13.5

c Explosive

600  so  4.22 c

2000 so 1000


MODE  n p

PHYS:P  4j  1

m1     8016 6 6012 7 7014 3 1001 5 $TNT 1.65

m4     11023 0.4995 53127 0.4995 $ NaI  detector 81000 0.001

c      sample material

m11    1001 2 6012 2 $CH2 -0.952

m12    1001 2 8016 1 $H2O -1

m13    1002 2 8016 1 $D2O -1.2

m14    1001 -2.97 6012 -17.79 $Polyethelyne -0.91

m15    8016 -0.000301 7014 -0.000976 $air -0.0013

m16    6012  1 $graphite  -2.25

c moderation material

m21    1001  3  5010 1 6012 3  $Boric acid

m22    3006 2 16000 1 8016 4 $Li2SO4 -2.06

c N_shielding material

m31    3006 2 6012 1 8016 3 $Li2CO3 -0.88

m32    82207 1 $Pb -11.35

c P_shielding material
```

```
c TALLY SPECIFICATION

f8:p  489

ft8  geb  0.4  0  0

f18:p 489

ft18 geb  4.22E-4  1.15E-3  0

cf28:p 489

c ft28  geb  0.007  0.014  0

c f38:p 489 c ft38  geb 0.061  0.004  0

f48:p 489 e0  0  1.0e-5  1.0e-3  1024i  12

f4:p 489

e4  0  1.0e-5  1.0e-3  1024i  12

nps        100000000

print

 SDEF  ERG=D1 POS=0 0 -18

SP1   -3 1.025 2.926
```

A.4   Simulation of neutron flux and dose in large cavity

This input file compose of neutron shielding and gamma shielding.

```
C

111   0 1 -2 11 -12 21 -22 IMP:N=1 imp:p=1

112   0 1 -2 11 -12 22 -23 IMP:N=1 imp:p=1

113   0 1 -2 11 -12 23 -24 IMP:N=1 imp:p=1

114   0 1 -2 11 -12 24 -25 IMP:N=1 imp:p=1

115   0 1 -2 11 -12 25 -26 IMP:N=1 imp:p=1

116   0 1 -2 11 -12 26 -27 IMP:N=1 imp:p=1

c 8
```

```
121    0 1 -2 12 -13 21 -22 IMP:N=1 imp:p=1

122    0 1 -2 12 -13 22 -23 IMP:N=1 imp:p=1

123    0 1 -2 12 -13 23 -24 IMP:N=1 imp:p=1

124    0 1 -2 12 -13 24 -25 IMP:N=1 imp:p=1

125    0 1 -2 12 -13 25 -26 IMP:N=1 imp:p=1

126    0 1 -2 12 -13 26 -27 IMP:N=1 imp:p=1
c 15
131    0 1 -2 13 -14 21 -22 IMP:N=1 imp:p=1

132    0 1 -2 13 -14 22 -23 IMP:N=1 imp:p=1

133    0 1 -2 13 -14 23 -24 IMP:N=1 imp:p=1

134    0 1 -2 13 -14 24 -25 IMP:N=1 imp:p=1

135    0 1 -2 13 -14 25 -26 IMP:N=1 imp:p=1

136    0 1 -2 13 -14 26 -27 IMP:N=1 imp:p=1
c 22
141    0 1 -2 14 -15 21 -22 IMP:N=1 imp:p=1

142    0 1 -2 14 -15 22 -23 IMP:N=1 imp:p=1

143    0 1 -2 14 -15 23 -24 IMP:N=1 imp:p=1

144    0 1 -2 14 -15 24 -25 IMP:N=1 imp:p=1

145    0 1 -2 14 -15 25 -26 IMP:N=1 imp:p=1

146    0 1 -2 14 -15 26 -27 IMP:N=1 imp:p=1
c 29
151    0 1 -2 15 -16 21 -22 IMP:N=1 imp:p=1

152    0 1 -2 15 -16 22 -23 IMP:N=1 imp:p=1

153    0 1 -2 15 -16 23 -24 IMP:N=1 imp:p=1

154    0 1 -2 15 -16 24 -25 IMP:N=1 imp:p=1

155    0 1 -2 15 -16 25 -26 IMP:N=1 imp:p=1
```

```
156    0 1 -2 15 -16 26 -27 IMP:N=1 imp:p=1

c

161    0 1 -2 16 -17 21 -22 IMP:N=1 imp:p=1

162    0 1 -2 16 -17 22 -23 IMP:N=1 imp:p=1

163    0 1 -2 16 -17 23 -24 IMP:N=1 imp:p=1

164    0 1 -2 16 -17 24 -25 IMP:N=1 imp:p=1

165    0 1 -2 16 -17 25 -26 IMP:N=1 imp:p=1

166    0 1 -2 16 -17 26 -27 IMP:N=1 imp:p=1

c

171    0 1 -2 17 -18 21 -22 IMP:N=1 imp:p=1

172    0 1 -2 17 -18 22 -23 IMP:N=1 imp:p=1

173    0 1 -2 17 -18 23 -24 IMP:N=1 imp:p=1

174    0 1 -2 17 -18 24 -25 IMP:N=1 imp:p=1

175    0 1 -2 17 -18 25 -26 IMP:N=1 imp:p=1

176    0 1 -2 17 -18 26 -27 IMP:N=1 imp:p=1

c

181    0 1 -2 18 -19 21 -22 IMP:N=1 imp:p=1

182    0 1 -2 18 -19 22 -23 IMP:N=1 imp:p=1

183    0 1 -2 18 -19 23 -24 IMP:N=1 imp:p=1

184    0 1 -2 18 -19 24 -25 IMP:N=1 imp:p=1

185    0 1 -2 18 -19 25 -26 IMP:N=1 imp:p=1

186    0 1 -2 18 -19 26 -27 IMP:N=1 imp:p=1

c

211    0 2 -3 11 -12 21 -22 IMP:N=1 imp:p=1

212    0 2 -3 11 -12 22 -23 IMP:N=1 imp:p=1

213    0 2 -3 11 -12 23 -24 IMP:N=1 imp:p=1
```

```
214    0 2 -3 11 -12 24 -25 IMP:N=1 imp:p=1

215    0 2 -3 11 -12 25 -26 IMP:N=1 imp:p=1

216    0 2 -3 11 -12 26 -27 IMP:N=1 imp:p=1

c

221    0 2 -3 12 -13 21 -22 IMP:N=1 imp:p=1

222    0 2 -3 12 -13 22 -23 IMP:N=1 imp:p=1

223    0 2 -3 12 -13 23 -24 IMP:N=1 imp:p=1

224    0 2 -3 12 -13 24 -25 IMP:N=1 imp:p=1

225    0 2 -3 12 -13 25 -26 IMP:N=1 imp:p=1

226    0 2 -3 12 -13 26 -27 IMP:N=1 imp:p=1

c

231    0 2 -3 13 -14 21 -22 IMP:N=1 imp:p=1

232    0 2 -3 13 -14 22 -23 IMP:N=1 imp:p=1

233    0 2 -3 13 -14 23 -24 IMP:N=1 imp:p=1

234    0 2 -3 13 -14 24 -25 IMP:N=1 imp:p=1

235    0 2 -3 13 -14 25 -26 IMP:N=1 imp:p=1

236    0 2 -3 13 -14 26 -27 IMP:N=1 imp:p=1

c

241    0 2 -3 14 -15 21 -22 IMP:N=1 imp:p=1

242    0 2 -3 14 -15 22 -23 IMP:N=1 imp:p=1

243    0 2 -3 14 -15 23 -24 IMP:N=1 imp:p=1

244    0 2 -3 14 -15 24 -25 IMP:N=1 imp:p=1

245    0 2 -3 14 -15 25 -26 IMP:N=1 imp:p=1

246    0 2 -3 14 -15 26 -27 IMP:N=1 imp:p=1

c

251    0 2 -3 15 -16 21 -22 IMP:N=1 imp:p=1
```

```
252   0 2 -3 15 -16 22 -23 IMP:N=1 imp:p=1

253   0 2 -3 15 -16 23 -24 IMP:N=1 imp:p=1

254   0 2 -3 15 -16 24 -25 IMP:N=1 imp:p=1

255   0 2 -3 15 -16 25 -26 IMP:N=1 imp:p=1

256   0 2 -3 15 -16 26 -27 IMP:N=1 imp:p=1

c

261   0 2 -3 16 -17 21 -22 IMP:N=1 imp:p=1

262   0 2 -3 16 -17 22 -23 IMP:N=1 imp:p=1

263   0 2 -3 16 -17 23 -24 IMP:N=1 imp:p=1

264   0 2 -3 16 -17 24 -25 IMP:N=1 imp:p=1

265   0 2 -3 16 -17 25 -26 IMP:N=1 imp:p=1

266   0 2 -3 16 -17 26 -27 IMP:N=1 imp:p=1

c

271   0 2 -3 17 -18 21 -22 IMP:N=1 imp:p=1

272   0 2 -3 17 -18 22 -23 IMP:N=1 imp:p=1

273   0 2 -3 17 -18 23 -24 IMP:N=1 imp:p=1

274   0 2 -3 17 -18 24 -25 IMP:N=1 imp:p=1

275   0 2 -3 17 -18 25 -26 IMP:N=1 imp:p=1

276   0 2 -3 17 -18 26 -27 IMP:N=1 imp:p=1

c

281   0 2 -3 18 -19 21 -22 IMP:N=1 imp:p=1

282   0 2 -3 18 -19 22 -23 IMP:N=1 imp:p=1

283   0 2 -3 18 -19 23 -24 IMP:N=1 imp:p=1

284   0 2 -3 18 -19 24 -25 IMP:N=1 imp:p=1

285   0 2 -3 18 -19 25 -26 IMP:N=1 imp:p=1

286   0 2 -3 18 -19 26 -27 IMP:N=1 imp:p=1
```

```
c

311   0 3 -4 11 -12 21 -22 IMP:N=1 imp:p=1

312   0 3 -4 11 -12 22 -23 IMP:N=1 imp:p=1

313   0 3 -4 11 -12 23 -24 IMP:N=1 imp:p=1

314   0 3 -4 11 -12 24 -25 IMP:N=1 imp:p=1

315   0 3 -4 11 -12 25 -26 IMP:N=1 imp:p=1

316   0 3 -4 11 -12 26 -27 IMP:N=1 imp:p=1

c

321   0 3 -4 12 -13 21 -22 IMP:N=1 imp:p=1

322   0 3 -4 12 -13 22 -23 IMP:N=1 imp:p=1

323   0 3 -4 12 -13 23 -24 IMP:N=1 imp:p=1

324   0 3 -4 12 -13 24 -25 IMP:N=1 imp:p=1

325   0 3 -4 12 -13 25 -26 IMP:N=1 imp:p=1

326   0 3 -4 12 -13 26 -27 IMP:N=1 imp:p=1

c

331   0 3 -4 13 -14 21 -22 IMP:N=1 imp:p=1

332   0 3 -4 13 -14 22 -23 IMP:N=1 imp:p=1

333   0 3 -4 13 -14 23 -24 IMP:N=1 imp:p=1

334   0 3 -4 13 -14 24 -25 IMP:N=1 imp:p=1

335   0 3 -4 13 -14 25 -26 IMP:N=1 imp:p=1

336   0 3 -4 13 -14 26 -27 IMP:N=1 imp:p=1

c

341   0 3 -4 14 -15 21 -22 IMP:N=1 imp:p=1

342   0 3 -4 14 -15 22 -23 IMP:N=1 imp:p=1

343   0 3 -4 14 -15 23 -24 IMP:N=1 imp:p=1

344   0 3 -4 14 -15 24 -25 IMP:N=1 imp:p=1
```

```
345    0 3 -4 14 -15 25 -26 IMP:N=1 imp:p=1

346    0 3 -4 14 -15 26 -27 IMP:N=1 imp:p=1

c

351    0 3 -4 15 -16 21 -22 IMP:N=1 imp:p=1

352    0 3 -4 15 -16 22 -23 IMP:N=1 imp:p=1

353    0 3 -4 15 -16 23 -24 IMP:N=1 imp:p=1

354    0 3 -4 15 -16 24 -25 IMP:N=1 imp:p=1

355    0 3 -4 15 -16 25 -26 IMP:N=1 imp:p=1

356    0 3 -4 15 -16 26 -27 IMP:N=1 imp:p=1

c

361    0 3 -4 16 -17 21 -22 IMP:N=1 imp:p=1

362    0 3 -4 16 -17 22 -23 IMP:N=1 imp:p=1

363    0 3 -4 16 -17 23 -24 IMP:N=1 imp:p=1

364    0 3 -4 16 -17 24 -25 IMP:N=1 imp:p=1

365    0 3 -4 16 -17 25 -26 IMP:N=1 imp:p=1

366    0 3 -4 16 -17 26 -27 IMP:N=1 imp:p=1

c

371    0 3 -4 17 -18 21 -22 IMP:N=1 imp:p=1

372    0 3 -4 17 -18 22 -23 IMP:N=1 imp:p=1

373    0 3 -4 17 -18 23 -24 IMP:N=1 imp:p=1

374    0 3 -4 17 -18 24 -25 IMP:N=1 imp:p=1

375    0 3 -4 17 -18 25 -26 IMP:N=1 imp:p=1

376    0 3 -4 17 -18 26 -27 IMP:N=1 imp:p=1

c

381    0 3 -4 18 -19 21 -22 IMP:N=1 imp:p=1

382    0 3 -4 18 -19 22 -23 IMP:N=1 imp:p=1
```

```
383    0 3 -4 18 -19 23 -24 IMP:N=1 imp:p=1

384    0 3 -4 18 -19 24 -25 IMP:N=1 imp:p=1

385    0 3 -4 18 -19 25 -26 IMP:N=1 imp:p=1

386    0 3 -4 18 -19 26 -27 IMP:N=1 imp:p=1

c

411    0 4 -5 11 -12 21 -22 IMP:N=1 imp:p=1

412    0 4 -5 11 -12 22 -23 IMP:N=1 imp:p=1

413    0 4 -5 11 -12 23 -24 IMP:N=1 imp:p=1

414    0 4 -5 11 -12 24 -25 IMP:N=1 imp:p=1

415    0 4 -5 11 -12 25 -26 IMP:N=1 imp:p=1

416    0 4 -5 11 -12 26 -27 IMP:N=1 imp:p=1

c

421    0 4 -5 12 -13 21 -22 IMP:N=1 imp:p=1

422    0 4 -5 12 -13 22 -23 IMP:N=1 imp:p=1

423    0 4 -5 12 -13 23 -24 IMP:N=1 imp:p=1

424    0 4 -5 12 -13 24 -25 IMP:N=1 imp:p=1

425    0 4 -5 12 -13 25 -26 IMP:N=1 imp:p=1

426    0 4 -5 12 -13 26 -27 IMP:N=1 imp:p=1

c

431    0 4 -5 13 -14 21 -22 IMP:N=1 imp:p=1

432    0 4 -5 13 -14 22 -23 IMP:N=1 imp:p=1

433    0 4 -5 13 -14 23 -24 IMP:N=1 imp:p=1

434    0 4 -5 13 -14 24 -25 IMP:N=1 imp:p=1

435    0 4 -5 13 -14 25 -26 IMP:N=1 imp:p=1

436    0 4 -5 13 -14 26 -27 IMP:N=1 imp:p=1

c
```

```
441   0 4 -5 14 -15 21 -22 IMP:N=1 imp:p=1

442   0 4 -5 14 -15 22 -23 IMP:N=1 imp:p=1

443   0 4 -5 14 -15 23 -24 IMP:N=1 imp:p=1

444   0 4 -5 14 -15 24 -25 IMP:N=1 imp:p=1

445   0 4 -5 14 -15 25 -26 IMP:N=1 imp:p=1

446   0 4 -5 14 -15 26 -27 IMP:N=1 imp:p=1

c

451   0 4 -5 15 -16 21 -22 IMP:N=1 imp:p=1

452   0 4 -5 15 -16 22 -23 IMP:N=1 imp:p=1

453   0 4 -5 15 -16 23 -24 IMP:N=1 imp:p=1

454   0 4 -5 15 -16 24 -25 IMP:N=1 imp:p=1

455   0 4 -5 15 -16 25 -26 IMP:N=1 imp:p=1

456   0 4 -5 15 -16 26 -27 IMP:N=1 imp:p=1

c

461   0 4 -5 16 -17 21 -22 IMP:N=1 imp:p=1

462   0 4 -5 16 -17 22 -23 IMP:N=1 imp:p=1

463   0 4 -5 16 -17 23 -24 IMP:N=1 imp:p=1

464   0 4 -5 16 -17 24 -25 IMP:N=1 imp:p=1

465   0 4 -5 16 -17 25 -26 IMP:N=1 imp:p=1

466   0 4 -5 16 -17 26 -27 IMP:N=1 imp:p=1

c

471   0 4 -5 17 -18 21 -22 IMP:N=1 imp:p=1

472   0 4 -5 17 -18 22 -23 IMP:N=1 imp:p=1

473   0 4 -5 17 -18 23 -24 IMP:N=1 imp:p=1

474   0 4 -5 17 -18 24 -25 IMP:N=1 imp:p=1

475   0 4 -5 17 -18 25 -26 IMP:N=1 imp:p=1
```

```
476    0 4 -5 17 -18 26 -27 IMP:N=1 imp:p=1

c

481    0 4 -5 18 -19 21 -22 IMP:N=1 imp:p=1

482    0 4 -5 18 -19 22 -23 IMP:N=1 imp:p=1

483    0 4 -5 18 -19 23 -24 IMP:N=1 imp:p=1

484    0 4 -5 18 -19 24 -25 IMP:N=1 imp:p=1

485    0 4 -5 18 -19 25 -26 IMP:N=1 imp:p=1

486    0 4 -5 18 -19 26 -27 IMP:N=1 imp:p=1

c

500    11 -0.952 60 -21 -61 IMP:N=1 imp:p=1

510    32 -11.34 62 -60 -61 IMP:N=1 imp:p=1

600    11 -0.952 31 -32 33 -34 35 -36 #(1 -5 11 -19 21 -27)
       #(62 -21 -61) IMP:N=1 imp:p=1

700    21 -0.88 41 -42 43 -44 45 -46 #(31 -32 33 -34 35 -36)
                              IMP:N=1 imp:p=1

800    32 -11.35 51 -52 53 -54 55 -56 #(41 -42 43 -44 45 -46)
                              IMP:N=1 imp:p=1

900    0 -2000 #(51 -52 53 -54 55 -56) IMP:N=1 imp:p=1

950    0 2000 imp:n=0 imp:p=0


1      PX -20

2      PX -10

3      PX 0

4      PX 10

5      PX 20

11     PY -40
```

```
12    PY -30

13    PY -20

14    PY -10

15    PY 0

16    PY 10

17    Py 20

18    Py 30

19    Py 40

21    PZ -30

22    PZ -20

23    PZ -10

24    PZ 0

25    pz 10

26    pz 20

27    pz 30

c

31    px   -40.00000

32    px    40.00000

33    py   -60.00000

34    py    60.00000

35    pz   -50.00000

36    pz    50.00000

c

41    px   -45.00000

42    px    45.00000

43    py   -65.00000
```

```
44     py     65.00000

45     pz    -55.00000

46     pz     55.00000

c

51     px    -45.50000

52     px     45.50000

53     py    -65.50000

54     py     65.50000

55     pz    -55.50000

56     pz     55.50000

c

60     pz -33

61     cz 10

62     pz -40

c

2000   so 1000


MODE   n p

m1     8016 6 6012 7 7014 3 1001 5 $TNT 1.65

c      sample material

m11    1001 2 6012 2 $CH2 -0.952

m12    1001 2 8016 1 $H2O -1

m13    1002 2 8016 1 $D2O -1.2

m14    1001 -2.97 6012 -17.79 $Polyethelyne -1.19

c      moderation material

m21 3006 2 6012 1 8016 3 $Li2CO3 -0.88
```

```
m22     3006 2 16000 1 8016 4 $Li2SO4 -2.06

c       N_shielding material

m31     26054 1 $Fe -7.86

m32     82207 1 $Pb -11.35

c       P_shielding material

f2:n  56

f12:n 52

f22:n 54

e2     1.e-8 4e-7 0.01 0.1 2 20

e12    1.e-8 4e-7 0.01 0.1 2 20

e22    1.e-8 4e-7 0.01 0.1 2 20

f32:p 56 f42:p 52

f52:p 54 f62:p 56

f72:p 52 f82:p 54

f114:n 111 112 113 114 115 116

       121 122 123 124 125 126

       131 132 133 134 135 136

       141 142 143 144 145 146

       151 152 153 154 155 156

       161 162 163 164 165 166

       171 172 173 174 175 176

       181 182 183 184 185 186

       211 212 213 214 215 216

       221 222 223 224 225 226

       231 232 233 234 235 236

       241 242 243 244 245 246
```

```
       251 252 253 254 255 256

       261 262 263 264 265 266

       271 272 273 274 275 276

       281 282 283 284 285 286

       311 312 313 314 315 316

       321 322 323 324 325 326

       331 332 333 334 335 336

       341 342 343 344 345 346

       351 352 353 354 355 356

       361 362 363 364 365 366

       371 372 373 374 375 376

       381 382 383 384 385 386

       411 412 413 414 415 416

       421 422 423 424 425 426

       431 432 433 434 435 436

       441 442 443 444 445 446

       451 452 453 454 455 456

       461 462 463 464 465 466

       471 472 473 474 475 476

       481 482 483 484 485 486

e114   1.e-8 4e-7 0.01 0.1 2 20

e62    0.01 1198i 12

e72    0.01 1198i 12

e82    0.01 1198i 12

de32   0.01 0.015 0.02 0.03 0.04 0.05 0.06 0.08 0.1 0.15 0.2 0.3

       0.4 0.5 0.6 0.8 1 1.5 2 3 4 5 6 8 10
```

```
df32   7.43 3.12 1.68 0.721 0.429 0.323 0.289 0.307 .0371 0.599
       0.856 1.38 1.89 2.38 2.84 3.69 4.47 6.14 7.55 9.96 12.1
       14.1 16.1 20.1 24.0
de42   0.01 0.015 0.02 0.03 0.04 0.05 0.06 0.08 0.1 0.15 0.2 0.3
       0.4 0.5 0.6 0.8 1 1.5 2 3 4 5 6 8 10
df42   7.43 3.12 1.68 0.721 0.429 0.323 0.289 0.307 .0371 0.599
       0.856 1.38 1.89 2.38 2.84 3.69 4.47 6.14 7.55 9.96 12.1
       14.1 16.1 20.1 24.0
de52   0.01 0.015 0.02 0.03 0.04 0.05 0.06 0.08 0.1 0.15 0.2 0.3
       0.4 0.5 0.6 0.8 1 1.5 2 3 4 5 6 8 10
df52   7.43 3.12 1.68 0.721 0.429 0.323 0.289 0.307 .0371 0.599
       0.856 1.38 1.89 2.38 2.84 3.69 4.47 6.14 7.55 9.96 12.1
       14.1 16.1 20.1 24.0
nps         10000000
print
SDEF  ERG=D1 POS=0 0 -35.1
SP1   -3 1.025 2.926


Note: In all case material can be change by using material card
 m1    8016 6 6012 7 7014 3 1001 5 $TNT 1.65
 m2    8016 6 6012 3 7014 6 1001 6 $RDX 1.816
 m3    6012 3 7014 6 1001 6 $ Melamine 1.57
 m4    6012 12 1001 22 8016 11 $ Sugar  1.59
 m5    6012 5 1001 8 $ Rubber  0.94
 m6    8016 6 6012 3 7014 3 1001 11 $ Silk 0.3
 m7    8016 4 6012 17 1001 21 7014 1  17000 21 $ Cocaine+Cl
```

APPENDIX B

MAXIMUM DOSE LIMITS

Whole Body (total effective dose equivalent)	5 rems (0.05 Sv) / year
or the sum of the deep dose equivalent	3 rems / quarter
and the committed dose equivalent to any	
individual organ or tissue (excluding	
the lens of the eye), being equal to	
50 rems (0.5 Sv).	
Skin of the Whole Body or Any Extremity	50 rems (0.5 Sv) / year
Lens of the Eye	15 rems (0.15 Sv) / year
Fetal Dose	0.5 rems / gestation
Guidance: Cumulative Exposure[2]	1 rem x age in years
	(10 mSv x age in years)
Maximum Dose Limit for the Public	0.1 rem (0.001 Sv) / year

CURRICULUM VITAE

FIRST NAME: Sommai   LAST NAME: Changkian

GENDER: Male   NATIONALITY: Thai   DATE OF BIRTH: 18 February 1963

EDUCATION BACKGROUND:

- 2001 - 2007 , Ph.D. student at Suranaree University of Technology.
- 1991 - 1996 , M.Sc. In Physics Prince of Songkla University, Thailand.
- 1982 - 1985 , B.Sc. In Physics Prince of Songkla University ,Thailand.

WORK EXPERIENCE:

- 1997 - present Prince of Songkla University, Physics Lecturer.
- 1987 - 1996   Songklanakarine hospital, Radiotherapy Physicist .

PUBLICATIONS:

- Changkian, S., (1999). Radiation Dose Response of Calcium Carbonate in Marine Shells.
- Changkian, S., (1998). A Study of Radioactive Elements of Various Rocks in Pattani province with the Gamma Spectrometer Method.
- Changkian, S., (1997). TL Dating of Ancient Pottery of Yarang Historical Site Amphur Yarang Pattani Province.

CONFERENCE:

- Participant, Optimization of the ^{252}Cf Based Explosive Detection System by Monte Carlo Simulation (2006). The First National Symposium on Physics Graduate Research, CHEP07.